UNIVERSITY OF OKLAHOMA

GRADUATE COLLEGE

SIGNAL PROCESSING TECHNIQUES FOR RADAR CROSS SECTION
MEASUREMENTS USING ORTHOGONAL FREQUENCY-DIVISION
MULTIPLEXING WAVEFORMS

A THESIS

SUBMITTED TO THE GRADUATE FACULTY

in partial fulfillment of the requirements for the

Degree of

MASTER OF SCIENCE

By

ROBERT CHAISE GLENN
Norman, Oklahoma
2023

SIGNAL PROCESSING TECHNIQUES FOR RADAR CROSS SECTION
MEASUREMENTS USING ORTHOGONAL FREQUENCY-DIVISION
MULTIPLEXING WAVEFORMS

A THESIS APPROVED FOR THE
SCHOOL OF ELECTRICAL AND COMPUTER ENGINEERING

BY THE COMMITTEE CONSISTING OF

Dr. Justin Metcalf, Chair

Dr. Jay McDaniel

Dr. Jessica Ruyle

Acknowledgments

The support and instruction provided by my primary advisor Dr. Justin Metcalf has been indispensable to my time as an undergraduate and graduate researcher. In particular, his classroom instruction and our private discussions have sparked a deep fondness of radar signal processing and its related fields. I would also like to thank Dr. Jay McDaniel and Dr. Jessica Ruyle for serving on my thesis committee, providing additional instruction, and reviewing my work.

I would also like to thank my fiancé, Kinsey Montgomery, who has supported me in every way imaginable throughout my college career. Additionally, my parents, Robert and Lori, have always been supportive and encouraging, no matter the circumstance.

Finally, I would like to thank my remaining family, as well as the friends I've made while on my academic journey. Each and every one of them has had a part in my success.

Table of Contents

List of Tables

List of Figures

Abstract

In recent work conducted at the University of Oklahoma's Advanced Radar Research Center, it has been shown that using orthogonal frequency-division multiplexing (OFDM) offers a significant time reduction in taking wideband radar cross section (RCS) measurements, compared with traditional techniques. This has led to an interest as to whether or not the reduced measurement time enables wideband RCS measurements of moving targets. In an attempt to answer this question, this thesis presents a simulation framework for RCS extraction of a moving target.

Because the target is moving, it is assumed that measurements are taken in an outdoor environment. As such, ground clutter is the primary competing interference. It is shown that in order to recover the target RCS, range-Doppler filtering must be performed. As a result, the filter shape, available Doppler resolution, and signal-to-noise ratio become the primary determiners of performance. Some closed-form expressions are derived to help determine acceptable system parameters and improve performance.

Interfering signals from other transmitters are also considered in this work. It is shown that if an interfering signal corrupts part of the spectrum, filtering is impossible because the target cannot be located in the range-Doppler space. To combat this, the spectrum is nulled at points where interference occurs. This enables filtering to be applied; however, nulls will exist in the RCS measurement. Finally, some spectral reconstruction techniques are discussed and tested with the purpose of estimating pieces of the spectrum that were lost.

Chapter 1

Introduction

Traditionally, taking radar cross section (RCS) measurements is a time-consuming process that requires the target to be stationary. Taking RCS measurements can be time-consuming due to not only the dependence on the transmitted wave's incidence angle, but also its frequency. Stepped frequency continuous wave (SFCW) radars are typically employed, which move through discrete frequency steps to measure RCS as a function of frequency [2] [3]. For a large amount of frequency steps, the measurement time can be quite long, since the frequencies are sent individually. On the other hand, orthogonal frequency-division multiplexing (OFDM) waveforms have the capability of sending many frequencies simultaneously in a single pulse. OFDM waveforms were designed this way for use in wireless communications, since data can be modulated onto the different frequencies, allowing for fast data transfer. Despite the fact that OFDM is traditionally a communications waveform, work has been done in developing processing techniques for the received OFDM signal so that radar measurements (range, velocity, etc.) can be obtained [4] [5].

Recent experiments at the University of Oklahoma's Advanced Radar Research Center have shown that OFDM can be used to obtain RCS measurements for frequencies contained in the OFDM waveform. This fact has led to a considerable decrease in the amount of time required to take RCS measurements. As a result, it is of inter-

est to see if this increased speed allows for wideband RCS measurements to be taken of moving targets. This thesis presents a simulation framework that was developed to assess the feasibility and signal processing requirements for RCS measurements of moving targets using OFDM. The goal is to provide insight and analysis for each step of the process in order to justify and enable future real-world experiments. In addition, a congested spectrum problem is presented in order to provide analysis on the effect of interfering signals from other transmitters, as well as how to mitigate this interference.

1.1 Outline

Chapter 2 presents the fundamental information required to understand the simulation model and subsequent analysis. The first topic is a brief derivation of the radar range equation, which is central to the RCS extraction process. The concept of RCS is then discussed, which provides some useful background into the quantity that we are interested in. Next, a quick sprint through random variable and random process theory is provided. This theory relates to both the foundation of the simulation model, as well as spectral estimation theory that is discussed at the end of this thesis. Finally, the OFDM signal model is presented, as well as the fundamentals of OFDM radar processing.

Chapter 3 discusses the MATLAB simulation. It starts by discussing how the base model was developed, including target information, noise, and ground clutter. It then discusses window selection for filtering and how the filters are applied. This naturally leads to RCS extraction, where several results are presented. Some equations are then derived to help determine simulation parameters, as well as improve performance. Lastly, some important practical considerations for performing real-world tests are discussed.

Chapter 4 considers what happens if an interfering signal has corrupted part of

the spectrum. The problem statement is provided first, followed by an analysis of the effect of including nulls in the spectrum. A few simulation tests are then presented, followed by a discussion of how concepts from spectral estimation theory may be used to reconstruct the spectrum.

Chapter 5 presents the conclusions and discusses possible avenues of future work.

Chapter 2

Background

Before discussing the simulation model and subsequent work, some background information must be provided to ensure sufficient understanding. This chapter is dedicated to providing detailed explanations of the requisite knowledge. This includes the radar range equation, radar cross section, fundamental random variable and random process theory, as well as foundations for the OFDM signal model and OFDM radar processing.

2.1 Radar Range Equation

Let us start by considering a radar transmitter that transmits a total peak power P_t (watts). If the antenna of this transmitter has an isotropic radiation pattern, then the power density Q_i (W/m^2) is given by the total power divided by the surface area of a sphere with radius R

$$Q_i = \frac{P_t}{4\pi R^2} \tag{2.1}$$

For an antenna that is nonisotropic (all realizable antennas), the power density will be concentrated in a specific direction; this is called a directional antenna. Such an antenna has a *directivity*, which is the ratio of its radiation intensity to that of an isotropic source, defined over all possible directions [6]. Now consider a directional antenna that has

some transmit gain G. The gain of a directional antenna is the directivity reduced by losses that arise from the antenna's radiation efficiency, as well as other losses in the transmitter system [6]. Denoting the transmit gain as G_t, the power density for a directional antenna is given by

$$Q_i = \frac{P_t G_t}{4\pi R^2} \tag{2.2}$$

Upon incidence with a target, part of the transmitted signal will be reflected back towards the radar. The power of this reflected signal is the product of the incident power density, Q_i, and a factor called the *radar cross section* (RCS) σ. RCS will be discussed in more detail in the next section. For now, it is only important to note that RCS has units of square meters (m^2). The total reflected power, P_{refl} (watts), can now be expressed as

$$P_{refl} = Q_i \sigma = \frac{P_t G_t \sigma}{4\pi R^2} \tag{2.3}$$

The reflected power density at the radar, Q_r, is found by dividing the total reflected power by the surface area of a sphere with radius R

$$Q_r = \frac{P_{refl}}{4\pi R^2} = \frac{P_t G_t \sigma}{(4\pi)^2 R^4} \tag{2.4}$$

The received power, P_r (watts), from a target at range R at the receive antenna is given by [7]

$$P_r = Q_r A_e = \frac{P_t G_t A_e \sigma}{(4\pi)^2 R^4} \tag{2.5}$$

where A_e is the effective area of the receiving antenna (m^2). [6] gives the effective antenna area as

$$A_e = \frac{\lambda^2 G}{4\pi} \tag{2.6}$$

where λ is the operating wavelength and G is the antenna gain. By inserting (2.6) into

(2.5) and changing G to G_r, we obtain a typical form of the radar range equation

$$P_r = \frac{P_t G_t G_r \lambda^2 \sigma}{(4\pi)^3 R^4} \qquad (2.7)$$

By including an extra loss term L into (2.7), we obtain a more complete version of the radar range equation that accounts for various losses that can occur. For a given radar configuration and scenario, the loss term can vary greatly, so L is calculated on a case-by-case basis. More information about possible sources of loss can be found in [7]. The complete version of the radar range equation is given by

$$P_r = \frac{P_t G_t G_r \lambda^2 \sigma}{(4\pi)^3 R^4 L} \qquad (2.8)$$

Although (2.8) is but one of many configurations that the radar range equation can take, it is quite easy to rearrange this form to directly solve for RCS

$$\sigma = \frac{P_r (4\pi)^3 R^4 L}{P_t G_t G_r \lambda^2} \qquad (2.9)$$

As long as all of the variables on the right side of (2.9) are accurately measured or estimated, it should be possible to calculate the target RCS.

2.2 Radar Cross Section

The topic of radar cross section will now be discussed in further detail. A general description will be given first to provide intuitive understanding, followed by a brief introduction to different scattering regimes. Finally, the RCS of a sphere will be discussed because of its importance to this work.

2.2.1 General Description

The IEEE dictionary of standard terms [8] defines radar cross section (RCS) as "4π times the ratio of the power per unit solid angle scattered in a specified direction of the power per unit area in a plane wave incident on the scatterer from a specified direction. More precisely, it is the limit of that ratio as the distance from the scatterer to the point where the scatterer power is measured approaches infinity." This definition is given mathematically by [1] as

$$\sigma = \lim_{R\to\infty} 4\pi R^2 \frac{|\boldsymbol{E}^{scat}|^2}{|\boldsymbol{E}^{inc}|^2} = \lim_{R\to\infty} 4\pi R^2 \frac{P_s}{P_i} \tag{2.10}$$

where $\boldsymbol{E}^{scat}$ is the scattered electric field, $\boldsymbol{E}^{inc}$ is the incident electric field, P_s is the scattered power density (W/m^2), P_i is the incident power density, and R is the distance between the target and point of measurement. Because of the limit that appears in (2.10), it is assumed that the measurement point is a sufficient distance away from the target so that near-field effects can be ignored.

As with the radar range equation, a brief derivation is helpful for understanding. [1] provides such a derivation for the RCS definition given in (2.10). We begin by assuming an incident power density P_i W/m^2 at the target. The reradiated power is then given by the multiplication of the incident power density and the target's RCS. This gives the reradiated power as σP_i W. From here, it is assumed that the reradiated power is scattered uniformly in all 4π steradians of space, which gives the scattered power density at a distance R from the target as [1]

$$P_s = \frac{\sigma P_i}{4\pi R^2} \tag{2.11}$$

7

(2.11) can then be solved for σ, giving

$$\sigma = 4\pi R^2 \frac{P_s}{P_i} \tag{2.12}$$

By adding the limit as R goes to infinity (point of measurement is in far-field) to (2.12), we obtain the RCS definition given by (2.10).

In general, RCS is dependent on the target's shape, material, and orientation, as well as the transmitted signal's frequency and polarization [1]. RCS is also typically expressed on a logarithmic power scale because of the wide range of values that RCS can take. This unit is denoted as dBsm (decibels per square meter) and is given by [1]

$$\sigma_{dBsm} = 10 \log_{10} \left(\frac{\sigma_{m^2}}{\sigma_{ref}} \right) \tag{2.13}$$

where σ_{m^2} is the RCS expressed in square meters and σ_{ref} is a reference RCS (typically 1 m^2).

2.2.2   Scattering Regimes & Sphere RCS

The details of the interaction between the incident EM wave and target are critical for characterizing RCS. In particular, the electrical size of the target is an important feature that affects RCS. The electrical size of a target is given by the ratio of its physical length to the wavelength of the incident wave. Depending on the value of electrical size, three primary scattering regimes can be observed for the target RCS; the Rayleigh region, resonant region, and optics region. The typical illustration of RCS over these regions is that of a sphere and is shown in Figure 2.1. [9] provides an equation for the

normalized RCS of a perfectly conducting sphere, which is a Mie series given by

$$\frac{\sigma}{\pi a^2} = \frac{j}{ka} \sum_{n=1}^{\infty} (-1)^n (2n+1) b_n \tag{2.14}$$

where

$$b_n = \frac{ka J_{n-1}(ka) - n J_n(ka)}{ka H_{n-1}^{(1)}(ka) - n H_n^{(1)}(ka)} - \frac{J_n(ka)}{H_n^{(1)}(ka)} \tag{2.15}$$

where a is the radius of the sphere, k is the wavenumber ($k = 2\pi/\lambda$), λ is the wavelength, J_n is a n-order spherical Bessel function of the first kind, $H_n^{(1)}$ is a n-order Hankel function given by

$$H_n^{(1)} = J_n(ka) + j Y_n(ka) \tag{2.16}$$

and Y_n is a n-order spherical Bessel function of the second kind [9].
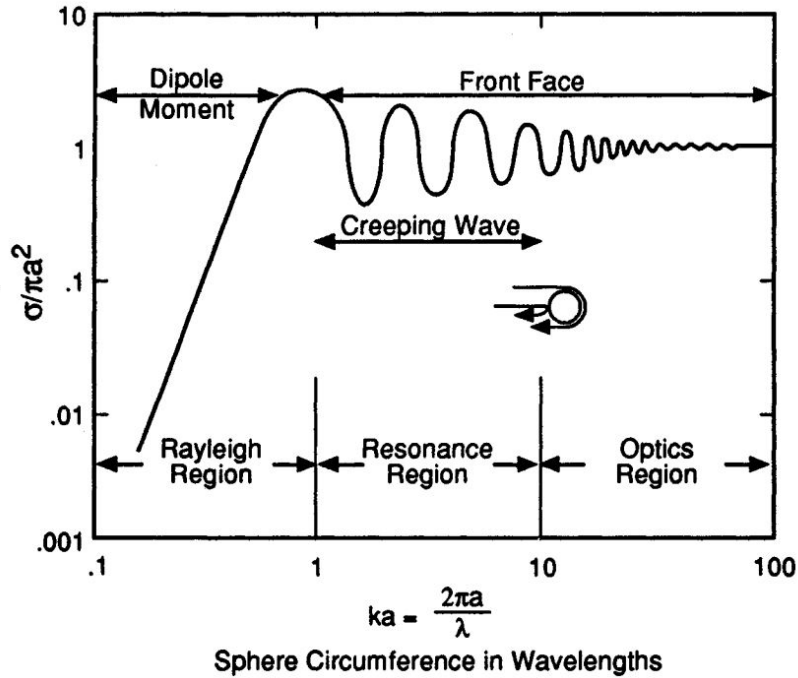
Figure 2.1: Radar cross section of a metallic sphere over the three scattering regimes [1]

9

The first scattering region, known as Rayleigh scattering, occurs when the incident wavelength is much larger than the target size. Because the wavelength is much larger, the incident wave phase is approximately constant across the target body. As a result, each part of the target experiences the same incident field, which means that this situation can be solved as a static field problem (although the incident field still changes with time). Because of the spatially static fields, a dipole moment is induced across the target, which is the primary scattering mechanism of Rayleigh scattering [1]. A dipole moment is given by

$$p = qd \tag{2.17}$$

where q is the separated charge and d is the charge separation. Because the dipole moment increases with increasing charge separation d, an incident wave that is polarized parallel to a larger dimension of the target body will experience greater scattering (i.e., a larger RCS). From Figure 2.1 it can be seen that through the Rayleigh region the RCS increases quite dramatically with increasing frequency. This is also an important characteristic of Rayleigh scattering. From [1], we have that the scattered electric field E^s is proportional to ωJ and that the current density J is given by

$$J = \frac{dq}{dt} = j\omega q \tag{2.18}$$

where ω is the angular frequency of the incident wave. It then follows that $E^s \propto \omega^2 q$, which means that the RCS (proportional to $(E^s)^2$) is proportional to ω^4 [1]:

$$\sigma \propto \omega^4 \tag{2.19}$$

The next scattering regime, known as the resonant region, occurs when the incident wavelength is on the order of the target size; that is, the target is between 1 and 10λ in

10

size [1]. In this region, the phase of the incident field varies greatly over the extent of the target body. Because of this, we see new surface wave effects that play an important role in EM scattering. For the case of a sphere, a wave of EM energy stays attached to the surface and travels around the entire structure; this is known as a creeping wave. Due to interference from this creeping wave, we see an oscillatory behavior in the resonant region of Figure 2.1.

When the incident wavelength becomes much smaller than the target size, we enter the optics region. The optics region has several different scattering mechanisms that can affect the target RCS, including specular scattering, end-region scattering, diffraction, and multiple-bounce [1]. In the case of a sphere, the primary mechanisms are likely to be specular scatting and multiple-bounce because of the smooth geometry. Specular scattering is the typical optics scattering in which the angle of reflection is equal to the angle of incidence. If the wavelength is sufficiently small enough compared to the target size (and the target is smooth), an approximation can be made where the target surface is modeled by a conducting plane tangential to the surface [10]. This can provide a simple expression for the radar cross section; however, multiple-bounce may also be an important factor, depending on the scenario. Multiple-bounce occurs when the scattered field reflects off the primary target and makes additional reflections before arriving back again at the radar receiver.

2.3   Random Variables & Processes

Throughout this work there are times where some background in probability and statistics is helpful for understanding. As such, this section provides a brief overview of the fundamentals of random variables and random processes. Since this topic is large in scope, only the necessities are discussed; more details can be found in [11].

2.3.1 Random Variable Fundamentals

In the most general sense, a random variable is a function that maps a set of possible outcomes to a set of numbers. The set of possible outcomes is viewed through the lens of probability. For example, take the case of rolling a dice. Assuming that the dice is fair, we assign a 1/6 chance that the dice will land on any given face. For a given dice roll, or trial, the face that the dice lands on is recorded and assigned some number. We can do this for each dice face, that is, we have developed a mapping from the dice outcomes to a set of numbers. For this simple example, we have developed a discrete random variable; however, from here on out the discussion will focus on continuous random variables. The principles are the same for both, but it should be noted that for a continuous random variable $\mathbf{x}$, the probability that $\mathbf{x}$ takes on a specific value $P(\mathbf{x} = x)$ is zero.

For a random variable we can define a function $F_x(x) = P(\mathbf{x} < x)$, which is known as the *cumulative distribution function* (CDF). This function describes the probability accumulation of the random variable. For example, $F_x(10) = P(\mathbf{x} < 10)$ yields a number that gives the probability that the random variable $\mathbf{x}$ takes on a value less than 10. It is important to note that $F_x(-\infty) = 0$ and $F_x(\infty) = 1$. Furthermore, the CDF monotonically increases between these points, i.e., its slope is always greater than or equal to 0. The derivative of the CDF gives the *probability density function* (PDF):

$$f_x(x) = \frac{dF_x(x)}{dx} \tag{2.20}$$

it then follows that

$$\int_{-\infty}^{\infty} f_x(x)dx = 1. \tag{2.21}$$

The PDF and CDF can also be used to determine the probability that $\mathbf{x}$ lies between

some values x_1 and x_2

$$P(x_1 < \mathbf{x} < x_2) = F_x(x_2) - F_x(x_1) = \int_{x_1}^{x_2} f_x(x)dx. \tag{2.22}$$

Some common continuous random variables include the Gaussian, exponential, uniform, and Rayleigh random variables; their PDFs are provided below for reference.
Gaussian:

$$f_x(x) = \frac{1}{\sqrt{2\pi\sigma^2}}e^{-(x-\mu)^2/(2\sigma^2)} \tag{2.23}$$

Exponential:

$$f_x(x) = \begin{cases} \lambda e^{-\lambda x} & x \geq 0 \\ 0 & \text{otherwise} \end{cases} \tag{2.24}$$

Uniform:

$$f_x(x) = \begin{cases} \frac{1}{b-a} & a \leq x \leq b \\ 0 & \text{otherwise} \end{cases} \tag{2.25}$$

Rayleigh:

$$f_x(x) = \begin{cases} \frac{x}{\sigma^2}e^{-x^2/(2\sigma^2)} & x \geq 0 \\ 0 & \text{otherwise} \end{cases} \tag{2.26}$$

Two important attributes of random variables are mean and variance. The mean, or *expected value*, of a random variable is defined as

$$\mu_x = E\{\mathbf{x}\} = \int_{-\infty}^{\infty} x f_x(x)dx \tag{2.27}$$

More generally, the mean is the first *moment* of a random variable. The moments for a

13

random variable are defined for $n \geq 1$ as

$$m_n = E\{\mathbf{x}^n\} = \int_{-\infty}^{\infty} x^n f_x(x) dx \tag{2.28}$$

The variance is defined as

$$\sigma_x^2 = \text{Var}\{\mathbf{x}\} = E\left\{(\mathbf{x} - \mu_x)^2\right\} = \int_{-\infty}^{\infty} (x - \mu_x)^2 f_x(x) dx. \tag{2.29}$$

The variance is more generally called the second *central moment*. The central moments for a random variable are defined for $n \geq 1$ as

$$\zeta_n = E\left\{(\mathbf{x} - \mu_x)^n\right\} = \int_{-\infty}^{\infty} (x - \mu_x)^n f_x(x) dx. \tag{2.30}$$

The last important concept for random variables is that you can have joint probability distributions for multiple random variables. If we consider the random variables $\mathbf{x}$ and $\mathbf{y}$, the joint PDF is given by $f_{xy}(x, y)$. We can then define the *correlation* of $\mathbf{x}$ and $\mathbf{y}$ as

$$\text{COR}(\mathbf{x}, \mathbf{y}) = E\{\mathbf{xy}\} = \int_{-\infty}^{\infty} \int_{-\infty}^{\infty} xy f_{xy}(x, y) dx dy. \tag{2.31}$$

We also define the *covariance* as

$$\text{COV}(\mathbf{x}, \mathbf{y}) = E\{(\mathbf{x} - \mu_x)(\mathbf{y} - \mu_y)\} = \int_{-\infty}^{\infty} \int_{-\infty}^{\infty} (x - \mu_x)(y - \mu_y) f_{xy}(x, y) dx dy. \tag{2.32}$$

The covariance and correlation are related by

$$E\{(\mathbf{x} - \mu_x)(\mathbf{y} - \mu_y)\} = E\{\mathbf{xy}\} - E\{\mathbf{x}\}E\{\mathbf{y}\}. \tag{2.33}$$

$\mathbf{x}$ and $\mathbf{y}$ are said to be *uncorrelated* if $E\{\mathbf{xy}\} = E\{\mathbf{x}\}E\{\mathbf{y}\}$, i.e., the covariance is zero.

If the correlation of **x** and **y** is zero ($E\{\mathbf{xy}\} = 0$), then they are said to be *orthogonal*.

2.3.2 Random Processes

Up to this point, we have been concerned with the statistical properties of a single event through the use of random variables. In order to allow for practical application, we must now add an extra dimension to include random measurements that may vary over time and/or space. The mean is now generalized as being time-varying and is given by

$$\mu_x(t) = E\{\mathbf{x}(t)\} = \int_{-\infty}^{\infty} x f(x,t) dx. \tag{2.34}$$

The *autocorrelation* of a random process is defined as

$$R_x(t_1, t_2) \triangleq E\{\mathbf{x}(t_1)\mathbf{x}^*(t_2)\}. \tag{2.35}$$

where * denotes complex conjugation. The *autocovariance* is then given by

$$C_x(t_1, t_2) = R_x(t_1, t_2) - \mu_x(t_1)\mu_x^*(t_2). \tag{2.36}$$

A random process is said to be *wide-sense stationary* (WSS) if the mean is a constant and the autocorrelation function (ACF) depends only on the difference between time indices. Mathematically, $E\{\mathbf{x}(t)\} = \mu_x$ and $E\{\mathbf{x}(t_1)\mathbf{x}^*(t_2)\} = R_x(t_1 - t_2) = R_x(\tau)$. This naturally leads to a restatement of (2.36) for a WSS process

$$C_x(\tau) = R_x(\tau) - |\mu_x|^2. \tag{2.37}$$

Another useful fact for WSS processes is that the Fourier transform of the ACF describes the spectral content of the random process, known as the *power spectral*

density (PSD). The PSD represents the density of average power versus frequency and is formally given by

$$S_x(f) = \int_{-\infty}^{\infty} R_x(\tau)e^{-j2\pi f\tau} d\tau. \tag{2.38}$$

Note that the average power of the process is given by the integral of the PSD:

$$\int_{-\infty}^{\infty} S_x(f)df = R_x(0) = P_{AVE}. \tag{2.39}$$

For a WSS process that is said to be *white*, the PSD is a constant k. Since the PSD is a constant, the ACF is a delta function scaled by this constant, $R(\tau) = k\delta(\tau)$. In other words, a white process is one that is only correlated to itself when compared at the same point in time.

The final property about random processes to be mentioned involves the output of a linear, time-invariant (LTI) system when a WSS random process is the input. For a LTI system with impulse response $h(t)$, if the input random process has an ACF $R_x(\tau)$, then the output ACF $R_y(\tau)$ is given by

$$R_y(\tau) = R_x(\tau) \circledast h^*(-\tau) \circledast h(\tau). \tag{2.40}$$

where $\circledast$ denotes convolution. Taking the Fourier transform of (2.40), we obtain

$$S_y(f) = S_x(f)H^*(f)H(f) = S_x(f)|H(f)|^2. \tag{2.41}$$

2.4 OFDM Signal Model

Orthogonal frequency-division multiplexing (OFDM) is a type of waveform that is a popular choice for broadband wired and wireless communication systems. This is

for a number of reasons, including its resilience to intersymbol interference (caused by multipath propagation) and its excellent scalability with faster data rates [12]. Of course, the primary interest of OFDM in this work is a radar application. However, before moving on to the radar signal processing, an understanding of the OFDM signal must be developed. As such, this section will present an OFDM signal model to set the foundation for the OFDM radar processing.

Let the complex baseband representation for a single-carrier signal be given by

$$x(t) = \sum_{i=0}^{N_{sym}-1} X_i \operatorname{rect}\left(\frac{t - iT_c}{T_c}\right) \tag{2.42}$$

where N_{sym} is the number of symbols, X_i is the modulation of the ith symbol, T_c is the symbol duration, and rect() is the rectangular function. The symbol modulations are typically pulled from phase shift keying (PSK) or quadrature amplitude modulation (QAM) schemes [12] [5]. The resulting signal is a series of N_{sym} rectangular pulses that are modulated according to the chosen modulation scheme. Now, to make the leap from single-carrier to OFDM, let us take a step back for a moment and consider a single, simple pulse. For the simple pulse (a rect function), the Fourier transform results in a sinc function. The sinc function is defined for nonzero values of x as $\operatorname{sinc}(x) = \frac{\sin(\pi x)}{\pi x}$ and is "1" at $x = 0$. The Rayleigh bandwidth, β_r, of this pulse is given by [13]

$$\beta_r = \frac{1}{\tau} \tag{2.43}$$

where τ is the pulse width. Visually, it can be seen that the Rayleigh bandwidth is the peak-to-null bandwidth. Figure 2.2 shows the frequency response for a 1 microsecond pulse. A pulse width of 1 microsecond corresponds to a Rayleigh bandwidth of 1 MHz, which is confirmed by observing that the peak-to-null bandwidth is indeed 1 MHz.
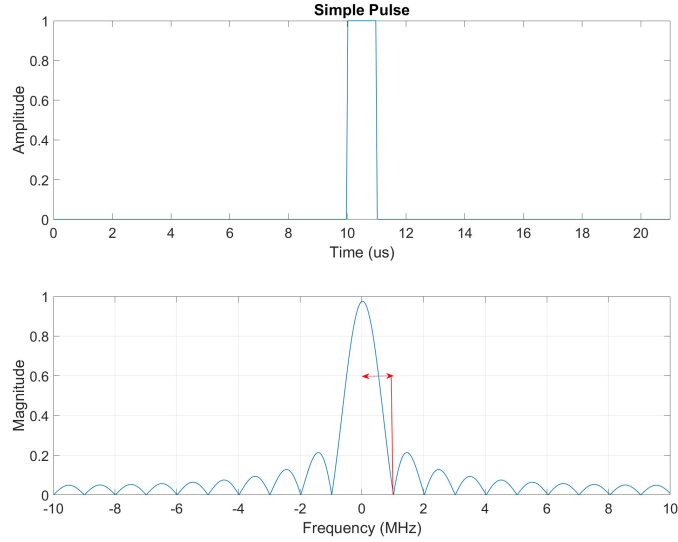
Figure 2.2: Simple pulse Rayleigh bandwidth visualization

As it will be seen, the Rayleigh bandwidth is a key component of constructing the OFDM signal. The single-carrier signal is only able to have one modulation per symbol. With OFDM however, each symbol contains multiple modulations across different *subcarriers*, with all of the information stored in the frequency domain. This is best illustrated with another simple example. Consider a 1 microsecond pulse of a 10 MHz sinusoid, shown in Figure 2.3a. The frequency domain response is a sinc function centered about the sinusoid center frequency, shown in Figure 2.3b. We also see a mirroring of the sinc function due to the fact that the sinusoid is real-valued. Now consider two additional pulses with center frequencies shifted up and down by the Rayleigh bandwidth. The time and frequency domain responses of these pulses are shown in Figure 2.3c and Figure 2.3d, respectively. Looking at the frequency domain content, it is clear that the peak of each sinc function lies at a null of the others. This means that a modulation can be stored at the peak of each sinc function without interference from other modulations. In other words, multiple modulations can be stored in a single time domain pulse.
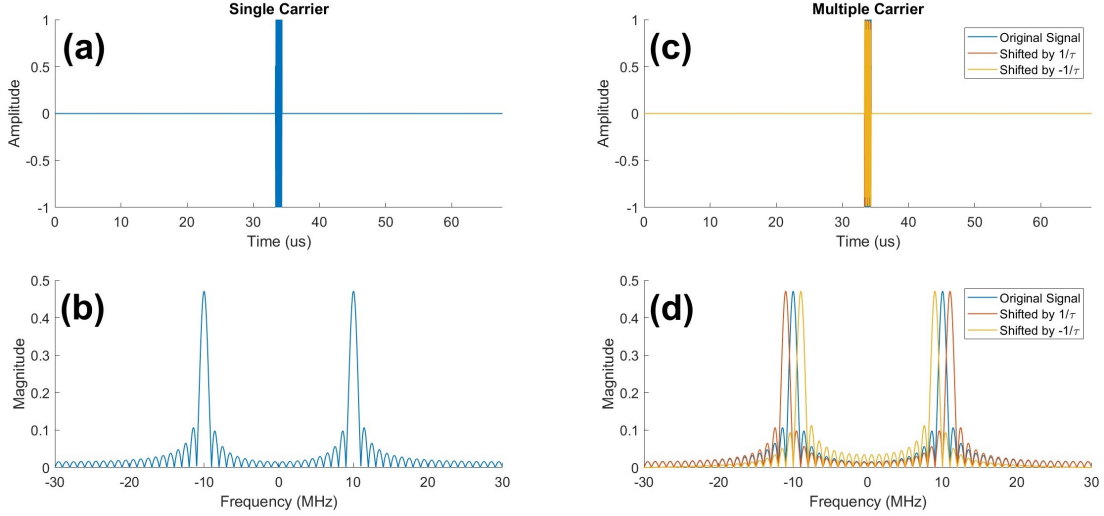
Figure 2.3: Adding subcarriers to single-carrier pulse. (a) Single-carrier time domain (b) Single-carrier frequency domain (c) Multi-carrier time domain (d) Multi-carrier frequency domain

Now that an intuitive understanding of the multi-carrier structure of OFDM has been provided, let's develop a mathematical description of the signal. To start, let the discrete Fourier transform (DFT) be defined by

$$X_k = \frac{1}{\sqrt{N}} \sum_{n=0}^{N-1} x_n \exp\left(\frac{-j2\pi kn}{N}\right), k = 0, \ldots, N-1 \tag{2.44}$$

and the inverse discrete Fourier transform (IDFT) by

$$x_n = \frac{1}{\sqrt{N}} \sum_{k=0}^{N-1} X_k \exp\left(\frac{j2\pi kn}{N}\right), n = 0, \ldots, N-1. \tag{2.45}$$

The benefit of defining the DFT and IDFT in this way is that the signal energy is conserved across both domains [12]. Using (2.45), the continuous time signal of a

single OFDM symbol with N_{sub} subcarriers is given by

$$x(t) = \frac{1}{\sqrt{N_{sub}}} \text{rect}\left(\frac{t}{T_c}\right) \sum_{k=0}^{N_{sub}-1} X_k \exp\left(\frac{j2\pi kt}{T_c}\right) \tag{2.46}$$

where T_c is the symbol duration and X_k is the modulation of the kth subcarrier. For a generalized OFDM signal with N_{sym} symbols, we can expand (2.46) to [5]

$$x(t) = \frac{1}{\sqrt{N_{sub}}} \sum_{i=0}^{N_{sym}-1} \text{rect}\left(\frac{t-iT_c}{T_c}\right) \sum_{k=0}^{N_{sub}-1} X_{i,k} \exp\left(\frac{j2\pi kt}{T_c}\right) \tag{2.47}$$

with $X_{k,i}$ being the modulation for the kth subcarrier of the ith symbol. Notice that each subcarrier is spaced by $\Delta f = \frac{1}{T_c}$ Hz, the Rayleigh bandwidth of the rectangular window.

In addition to the OFDM symbols, a cyclic prefix is typically attached to the beginning of each symbol. This helps prevent intersymbol interference and allows for frequency domain channel estimation and equalization [5]. A cyclic prefix that has N_{CP} samples will be composed of the last N_{CP} samples of the symbol that it is attached to. The total OFDM symbol duration (including the cyclic prefix) is then given by $T_{OFDM} = T_c + T_{CP}$, where T_{CP} is the time duration of the cyclic prefix. The full OFDM signal structure is illustrated in Figure 2.4.
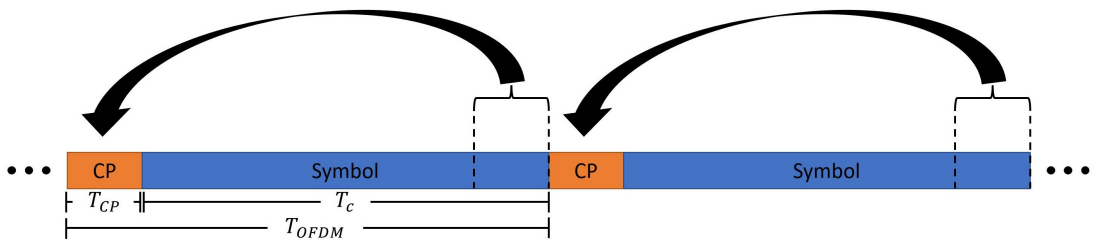
Figure 2.4: OFDM signal structure

Now that the transmitted signal model has been defined, attention will now be given to the received signal. First, assume that the received signal is perfectly synchronized and that it follows the typical stop-and-hop assumption. The stop-and-hop approximation is a common model used in pulsed radar system analysis which states that a target in motion can be modeled as stationary for the pulse transit time, but then "hops" to its next position in space for the next pulse [13]. That is, a target's continuous movement can be discretized across pulses. In the context of OFDM, the stop-and-hop approximation assumes that the target is stationary over the duration of a *symbol's* transit time, but that it moves across multiple symbols. With these assumptions, the continuous time signal received from a target at range R and radial velocity v_r m/s is [5]

$$x(t) = A(t)e^{j2\pi f_D t} \sum_{i=0}^{N_{sym}-1} \text{rect}\left(\frac{t - iT_{OFDM} - \frac{2R}{c}}{T_{OFDM}}\right) \sum_{k=0}^{N_{sub}-1} X_{i,k} e^{j2\pi k \Delta f(t - \frac{2R}{c})}$$

(2.48)

where $A(t)$ is the received signal amplitude, c is the speed of propagation, and $f_D = \frac{2v_r}{\lambda_c}$ is the Doppler frequency shift with λ_c being the transmit wavelength corresponding to the center frequency f_c. The primary differences between (2.48) and (2.47) are the amplitude variable $A(t)$, the Doppler frequency shift f_D across symbols, and the time delay $\frac{2R}{c}$ corresponding to the total signal propagation time to and from the target. These characteristics of the received signal are central to OFDM radar processing, which will now be discussed in detail.

2.5   OFDM Radar Processing

The first step in understanding OFDM radar processing is to view the transmitted and received signal as a matrix. Using the $X_{i,k}$ notation, the transmitted data matrix is

given by [4]

$$\mathbf{D}_{TX} = \begin{bmatrix} X_{0,0} & X_{1,0} & \ldots & X_{N_{sym}-1,0} \\ X_{0,1} & X_{1,1} & \ldots & X_{N_{sym}-1,1} \\ \vdots & \vdots & \ddots & \vdots \\ X_{0,N_{sub}-1} & X_{1,N_{sub}-1} & \ldots & X_{N_{sym}-1,N_{sub}-1} \end{bmatrix}. \quad (2.49)$$

Next, looking back at (2.48) yields insight as to what is happening in the range and Doppler dimensions. Across subcarriers (the range dimension), we see that there is an additional phase shift corresponding to the propagation time to and from the target. Assuming that we have a vector $\mathbf{k}_R \in \mathbb{C}^{N_{sub}}$ to describe the phase shift across subcarriers, the values of this vector are [5] [4]

$$k_R(k) = \exp\left(-j2\pi k\Delta f \frac{2R}{c}\right). \quad (2.50)$$

We can also observe that there is a Doppler shift f_D applied over the entire signal. Using the stop-and-hop assumption that was discussed earlier, this Doppler shift is only applied across symbols. Given a new vector $\mathbf{k}_D \in \mathbb{C}^{N_{sym}}$, the values for the Doppler vector are [5] [4]

$$k_D(i) = \exp\left(j2\pi i T_{OFDM} \frac{2v_r f_c}{c}\right) \quad (2.51)$$

where iT_{OFDM} is the discretized time and $\frac{2v_r f_c}{c} = \frac{2v_r}{\lambda_c} = f_D$ is the Doppler shift. Using (2.49), (2.50), and (2.51), the received data matrix can be represented as

$$\mathbf{D}_{RX} = \mathbf{A} \odot \mathbf{D}_{TX} \odot (\mathbf{k}_R \mathbf{k}_D^T) \quad (2.52)$$

where $\mathbf{A}$ is a matrix of amplitudes and $\odot$ denotes element-wise multiplication. By performing an element-wise division we can remove the transmitted modulations from

the received signal [4]

$$\mathbf{D}_{div} = \mathbf{D}_{RX} \oslash \mathbf{D}_{TX} = \mathbf{A} \odot (\mathbf{k}_R \mathbf{k}_D^T) \tag{2.53}$$

where $\oslash$ represents element-wise division.

Now that we have the data-free received matrix given by (2.53), we can perform an IDFT and DFT to obtain our range and Doppler responses, respectively. Because the IDFT is the matched filter for the range response [4], we start by applying the IDFT defined in (2.45) to (2.50)

$$\begin{aligned} R(n) = \text{IDFT}[k_R(k)] &= \frac{1}{\sqrt{N_{sub}}} \sum_{k=0}^{N_{sub}-1} k_R(k) \exp\left(\frac{j2\pi kn}{N_{sub}}\right) \\ &= \frac{1}{\sqrt{N_{sub}}} \sum_{k=0}^{N_{sub}-1} \exp\left(-j2\pi k\Delta f \frac{2R}{c}\right) \exp\left(\frac{j2\pi kn}{N_{sub}}\right) \\ &\quad n = 0, \ldots, N_{sub} - 1 \end{aligned} \tag{2.54}$$

which yields the range response. By considering the multiplication of two complex exponentials in (2.54) a complex number, it is clear that this equation will be at a max when the complex numbers sum as constructively as possible. This occurs when the exponentials multiply to unity due to their exponents being additive inverses of each other and results when

$$n = \left\lfloor \frac{2R\Delta f N_{sub}}{c} \right\rfloor \tag{2.55}$$

meaning that a peak in the range response will occur at this index value. The Doppler

response is created by applying the DFT defined in (2.44) to (2.51)

$$D(m) = \text{DFT}[k_D(i)] = \frac{1}{\sqrt{N_{sym}}} \sum_{i=0}^{N_{sym}-1} k_D(i) \exp\left(\frac{-j2\pi im}{N_{sym}}\right)$$

$$= \frac{1}{\sqrt{N_{sym}}} \sum_{i=0}^{N_{sym}-1} \exp\left(j2\pi i T_{OFDM}\frac{2v_r f_c}{c}\right) \exp\left(\frac{-j2\pi im}{N_{sym}}\right) \quad (2.56)$$

$$m = 0, \ldots, N_{sym} - 1$$

Once again, considering the case where the complex exponentials multiply to unity, the index of maximum Doppler response is given by

$$m = \left\lfloor \frac{2T_{OFDM}v_r f_c N_{sym}}{c} \right\rfloor. \quad (2.57)$$

The result of the processing described in this section is a sinc-shaped response in both range and Doppler dimensions [4], which will be better illustrated in the next chapter.

24

Chapter 3

Simulation

In this chapter, a MATLAB simulation is presented that models the received OFDM signal for a moving target. The data is processed using the radar processing techniques discussed in Section 2.5. The processed data is then filtered in order to extract the target's radar cross section. In addition to the simulation framework, some helpful expressions are derived, and a signal-to-noise ratio performance evaluation is given. Finally, some practical considerations are discussed, including the influence of Doppler shift and the role of a calibration object in RCS extraction.

3.1   Receive Signal Construction

In order to construct the received signal, the transmit signal for a single symbol must be built first. Let us assume that we have transmitted an OFDM signal where each subcarrier has been modulated with $1 + 0j$. We modulate with "1" because our primary interest is not to transmit data, but instead to measure RCS. Assuming that the spectrum is perfectly Nyquist sampled, the resulting frequency domain shape is a constant. Because the signal is Nyquist sampled, the resulting time domain signal will appear as a delta function as illustrated in Figure 3.1. This is because the underlying sinc function is being sampled at its nulls, that is, the sidelobes aren't going to appear.

Figure 3.2 shows that if the signal is oversampled, then the time domain sidelobes will begin to appear. The rect/sinc Fourier transform relationship and how they are sampled is important when analyzing the shape of the range/Doppler responses, as will be seen soon.
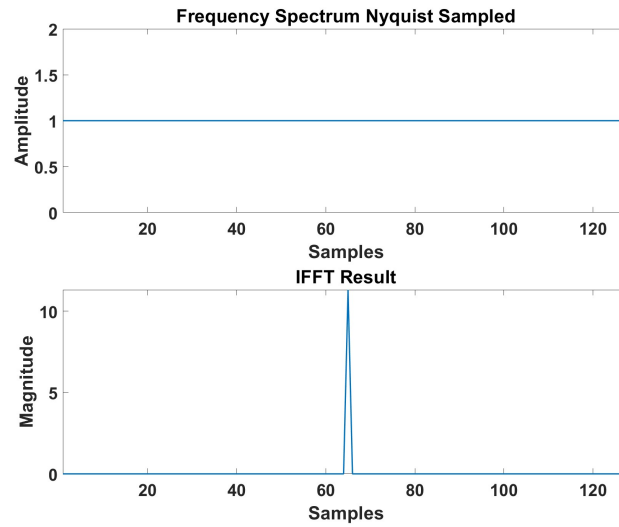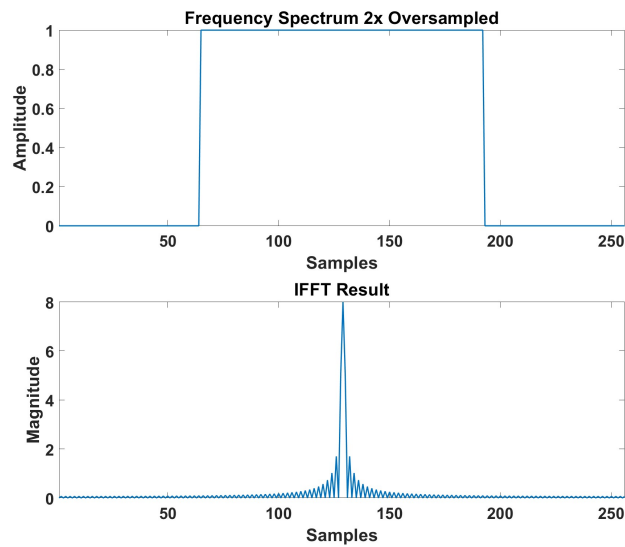

Figure 3.1: Nyquist sampled spectrum

Figure 3.2: Oversampling by a factor of 2

3.1.1 Target Information

Now that the foundation for a single symbol has been built, target information may be added. There are three primary characteristics to the target information; range, Doppler, and received power. The range and Doppler information comes from (2.50) and (2.51), respectively. The received power is derived using the radar range equation from (2.8) and is combined with the range-Doppler data via (2.53). After target information has been added, an inverse fast Fourier transfrom (IFFT) is taken across subcarriers and a fast Fourier transform (FFT) across symbols.

The result of this processing is best illustrated with an example. Table 3.1 gives the radar system and OFDM parameters used for this example scenario. Note that some of the system parameters are highly idealized. This is so that we have a high signal-to-noise ratio for preliminary tests. Later in this work, different signal-to-noise ratios will be explored more thoroughly. The wavelength and RCS are not given because these values change over subcarriers, that is, they are frequency dependent. In reality, the antenna gain is also frequency dependent, but is assumed to be constant for this work. Calculating the wavelength as a function of frequency is simple, but the RCS is much more complex. For this work, a script made by an ARRC PhD student, Rachel Jarvis, was used to calculate the RCS of a 12 inch sphere over the range of subcarrier

Table 3.1: Example Scenario 1 Parameters

System Parameters		OFDM Parameters	
Parameter	Value	Parameter	Value
P_{peak}	10 W	BW	150 MHz
f_c	5 GHz	Δf	200 kHz
G_t	40 dB	T_{cp}	4.5 μs
G_r	40 dB	T_c	$\frac{1}{\Delta f} = 5 \ \mu s$
L_s	6 dB	T_{OFDM}	$T_{cp} + T_c = 9.5 \ \mu s$
f_s	150 MHz	N_{sym}	700

frequencies. This script uses the equations presented in Section 2.2.2 to calculate the RCS. From Table 3.1, it is also important to note that P_{peak} is the *peak* power of the time domain signal, which is the power of the time domain signal when all subcarriers superimpose with the same phase. Lastly, note that because the sampling frequency f_s is equal to the OFDM symbol bandwidth, the signal is Nyquist sampled.
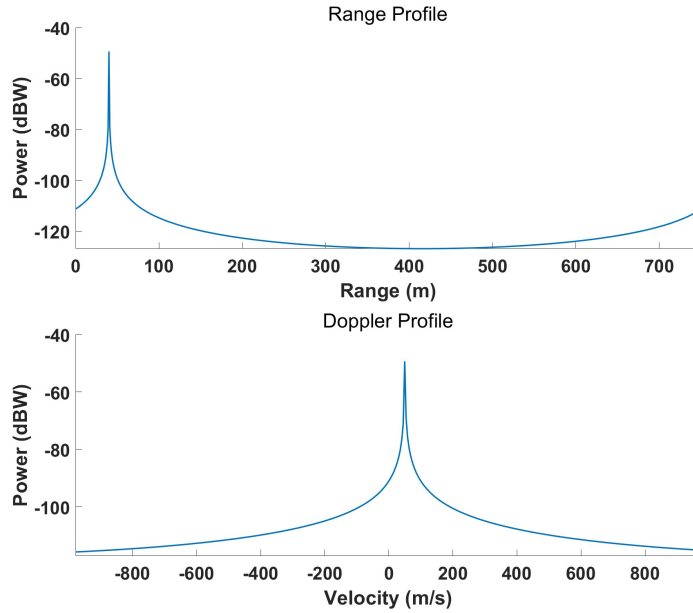
Figure 3.3: Example 1 range and Doppler profiles, $R = 40$ m, $v = 50$ m/s

Figure 3.3 shows the range and Doppler profiles for a target with a range of 40 meters and a radial velocity of 50 m/s. Notice that the sidelobe structure does not appear in either profile, which is a byproduct of being Nyquist sampled in both dimensions. Sidelobes will appear in the range profile if the signal is oversampled, which will be shown shortly. In Doppler, zero padding before the FFT would produce a similar result. Given the system and target parameters of this scenario, the radar range equation yields an average received power of -106.41 dBW. However, due to the IFFT and FFT we obtain a processing gain of $N_{sub}N_{sym}$ [4], which comes out to 57.2 dB for this example. This yields a final target power of about -49.2 dBW.

It can also be seen from Figure 3.3 that the unambiguous velocity is quite high (not all of it is shown), while the maximum unambiguous range is quite low. The maximum unambiguous range is given by

$$R_{ua} = \frac{cT_c}{2} \tag{3.1}$$

which yields $R_{ua} = 750$ m for this scenario. Because the symbol duration T_c is the inverse of the subcarrier spacing, increasing the subcarrier spacing will reduce R_{ua}. In general, for a pulse-Doppler radar the unambiguous velocity is given by

$$v_{ua} = \pm \left(\frac{PRF}{2} \right) \left(\frac{\lambda_c}{2} \right) \tag{3.2}$$

where λ_c is the carrier frequency wavelength and PRF is the pulse repetition frequency. In the context of OFDM, the pulse repetition frequency is $1/T_{OFDM}$, which gives

$$v_{ua} = \pm \frac{\lambda_c}{4T_{OFDM}} \tag{3.3}$$

which yields $v_{ua} = \pm 1578$ m/s for this scenario. Because T_{OFDM} is inversely proportional to the subcarrier spacing, increasing the subcarrier spacing will increase v_{ua}. Furthermore, the total number of symbols directly relates to the Doppler resolution. In this example, the Doppler resolution is $2|v_{ua}|/N_{sym} = 4.51$ m/s.

Before moving on to discussion about the noise and clutter model, Figures 3.4 and 3.5 are provided for additional visualization and insight. Figure 3.4 shows the range-Doppler map (RDM) for the scenario. Range-Doppler maps are a popular way of visualizing radar data and will be seen multiple times throughout this work. Figure 3.5 provides a look at how oversampling causes sidelobes to appear in the range profile. Note that Doppler sidelobes are still not present due to the fact that the data in the Doppler dimension has not been zero padded.
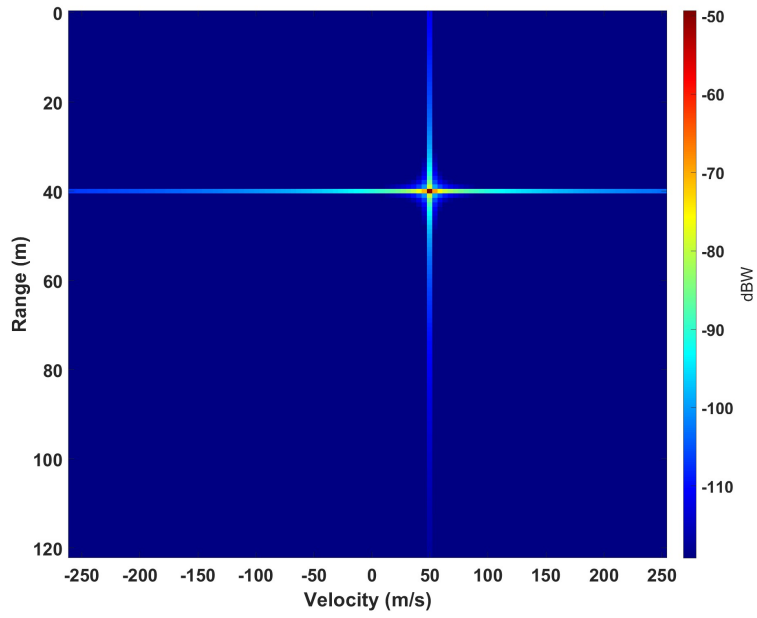
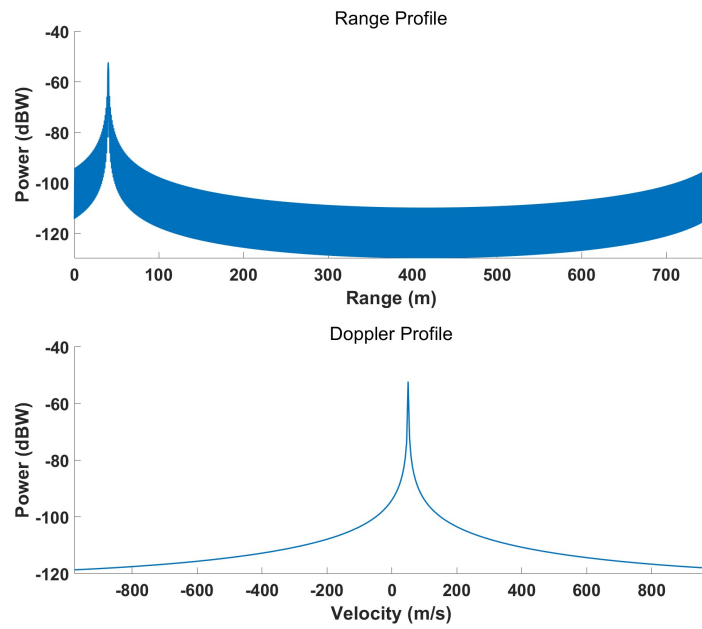Figure 3.4: Example 1 zoomed-in range-Doppler map, $R = 40$ m, $v = 50$ m/s

Figure 3.5: Example 1 range and Doppler profiles with 2x oversampling

3.1.2 Noise & Clutter Model

Thermal noise is an inescapable phenomenon of a radar receiver's hardware components. As such, it must be included in the simulation model. By the central limit theorem, the overall probability distribution of the sum of many independent random events is Gaussian [11]. In the case of thermal noise, these independent random events are the movements of electrons. When sampled in time, a given noise sample is completely uncorrelated to samples at other times. In the context of random processes, this means that the autocorrelation function $R(\tau)$ is zero everywhere except $\tau = 0$. That is, the autocorrelation function is an impulse at $\tau = 0$. Because the power spectral density is given by the Fourier transform of the autocorrelation function [11], the noise power is constant across all frequencies. Noise with this property is known as "white" noise. As such, thermal noise is modeled by additive white Gaussian noise (AWGN). The power of thermal noise is given by [7]

$$P_n = kTFB \tag{3.4}$$

where k is Boltzmann's constant, T is the standard temperature (290 K), F is the receiver noise figure (unitless), and B is the receiver bandwidth in Hz.

With the addition of thermal noise, a new principle may be introduced: signal-to-noise ratio. The signal-to-noise ratio (SNR) is the ratio of the received signal power to thermal noise power. Dividing (2.8) by (3.4), the SNR is given as

$$\text{SNR} = \frac{P_r}{P_n} = \frac{P_t G_t G_r \lambda^2 \sigma}{(4\pi)^3 R^4 L k T F B}. \tag{3.5}$$

SNR is probably the most critical performance metric in the field of radar signal processing. If the SNR is not sufficient, no amount of processing is going to be able to

recover the signal. From (3.5) it is seen that increasing the transmit power will increase SNR; however, another reasonable solution is to integrate pulses together. When integrating pulses, the target signal will sum constructively and the noise will sum destructively, which improves SNR. However, there are types of interference that can sum constructively across pulses, including ground clutter. Thus, pulse integration may help SNR but may not have a considerable effect on improving the signal-to-interference-plus-noise ratio (SINR), which is given by

$$\text{SINR} = \frac{P_r}{P_n + P_i} \tag{3.6}$$

where P_i is the interference power.

With the noise model presented, a brief discussion about the ground clutter model will now be given. Ground clutter is a type of radar interference that occurs when the transmitted signal is reflected off of the ground or objects on the ground such as buildings, trees, etc. A common model for the signal envelope amplitude of ground clutter is the Rayleigh distribution [14]. A random variable R is Rayleigh distributed if $R = \sqrt{X^2 + Y^2}$, where X and Y are independent Gaussian random variables [11]. Due to this fact, the magnitude of a complex Gaussian distributed random variable has a Rayleigh distribution ($|X + jY| = \sqrt{X^2 + Y^2}$). For this reason, the received voltage signal for ground clutter has been modeled by a complex Gaussian random vector. This random vector is duplicated for each symbol, i.e., the ground clutter response does not change over symbols. Because the power is proportional to the magnitude squared, the power distribution is exponential. In other words, the square of a Rayleigh random variable yields an exponential random variable [11].

Figure 3.6 gives the range and Doppler responses for the scenario previously discussed, including noise and clutter. The noise figure F is set to 8 dB, which yields a

noise power of -114.2 dBW using (3.4). The *pre-processing* SINR is set to -20 dB, which gives a clutter power of -86.4 dBW after rearranging (3.6) and solving for P_i. However, the clutter appears at a higher power post-processing because of a processing gain. This comes from the fact that the clutter is unchanging across symbols, therefore a processing gain of N_{sym} is observed. Applying this gain, the post-processing clutter power is -58 dBW, which gives the post-processing SINR as 8.76 dB. Figure 3.7 gives the range-Doppler map of this data, which has once again been zoomed in for clarity. The ground clutter occupies the zero Doppler cut, as expected. Note that although ground clutter is approximately zero velocity, in reality there may be elements of the clutter that have non-zero velocity from wind effects (such as trees moving in the wind). These are considered negligible in this work.
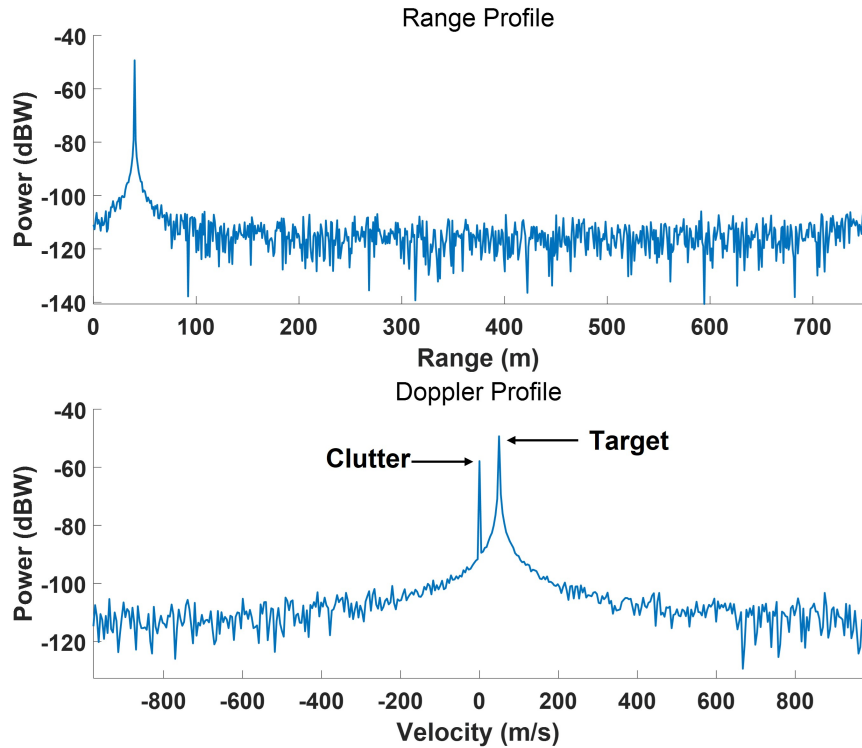

Figure 3.6: Example 1 range and Doppler profile, including noise and clutter
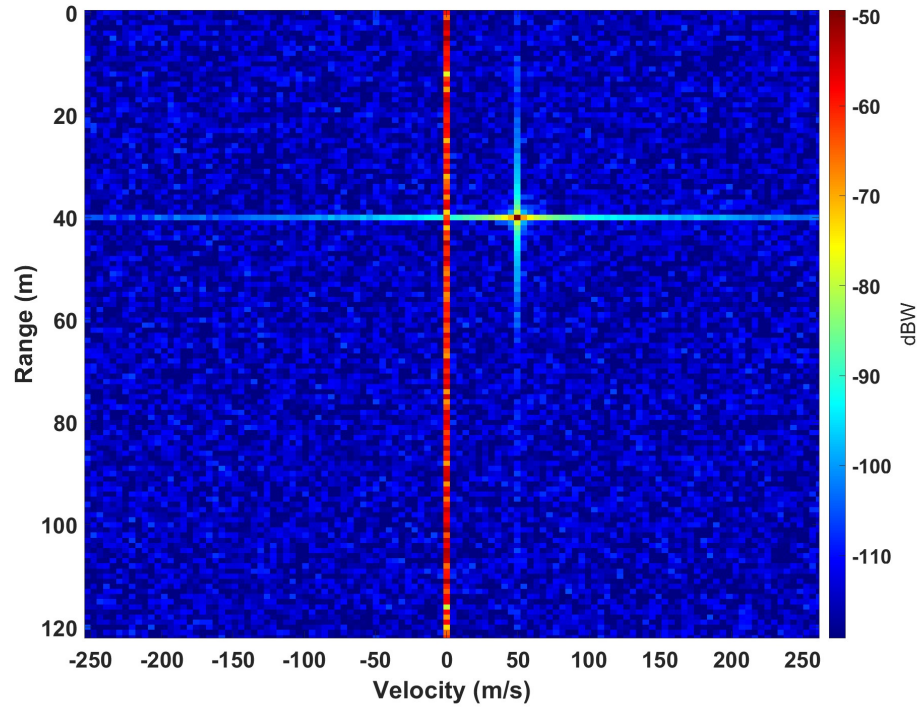
Figure 3.7: Example 1 range-Doppler map, including noise and clutter

3.2 Filtering

In order to accurately extract a target's RCS from radar data, interference must be filtered out. Luckily, a moving target is separated from the stationary ground clutter region after processing, which makes filtering a relatively easy process. For this work, filtering will be applied in both the range and Doppler dimensions. Filtering in range will have little effect on suppressing clutter, but will help reduce noise power. Filtering in Doppler will also help reduce noise power, but has the main purpose of removing clutter. In order to filter, we must first choose a windowing function. Ideally, the chosen window will remove as much clutter as possible, while retaining most of the target information. This section focuses on choosing a windowing function based on a couple of criteria that will be outlined shortly.

34

Before comparing windows, a fact about windowing in general will be explored. In range, windowing is done in the time domain, but for Doppler it is in the frequency domain. What they share in common, however, is that the responses being windowed are both sinc shaped. This means that we aren't interested in which domain the windowing is being applied in; the only interest is the effect of windowing on the *shape* of the opposite domain. So, the domains are simply labeled "A" and "B," rather than picking time or frequency. Figure 3.8 illustrates that a rect function in one domain yields a sinc in the other. By applying a window to the sinc function and convert-
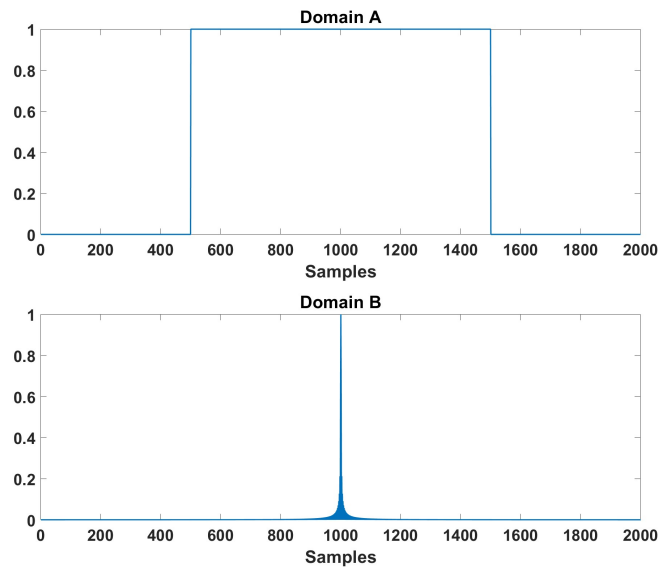
Figure 3.8: Visualization showing that a rect function in one domain yields a sinc function in the other

ing back to the other domain, the effect of the window can be observed. Figure 3.9 shows the domain A response after applying a Gaussian window in domain B. It can be seen that applying a window to the sinc function will result in a tapering of the rect function. This is due to the Fourier transform property that a multiplication in one domain is a convolution in the other. Thus, the rect function is being convolved with the Fourier transform of the windowing function. The "unchanged" trace of Figure

35

Figure 3.9: Windowing the sinc function in domain B tapers the rect function in domain A

3.9 shows the part of the response that has been *minimally* affected by the windowing. That is, this part of the response represen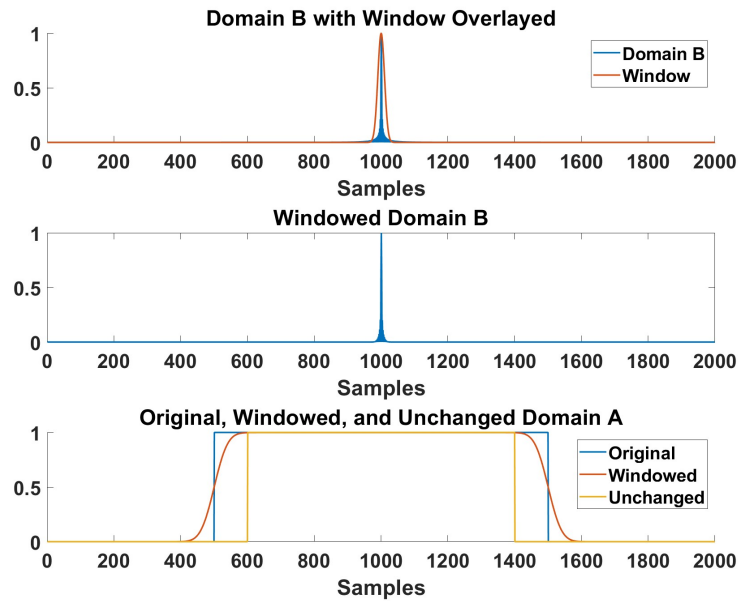ts the region of the convolution where both signals are mostly overlapped (the exact definition of "mostly overlapped" depends on the window). The tapering effect is important because windowing in range will produce a tapering in the subcarriers at the edges of the OFDM bandwidth. This means that by windowing in range, the RCS at the edges of the bandwidth will be incorrect. If one were to forgo windowing in range, then the extracted RCS could either be a little or very noisy, depending on the SNR. Luckily, for a single target, the range window doesn't have to be super tight. Figure 3.10 shows that the tapering is reduced when using a wider window. Of course, the Doppler window may have to be quite narrow, especially for slow-moving targets that lie near the clutter region. Figure 3.11 shows that a heavy taper results from using a narrow window. The effect of tapering on RCS extraction will be seen more in the next section.
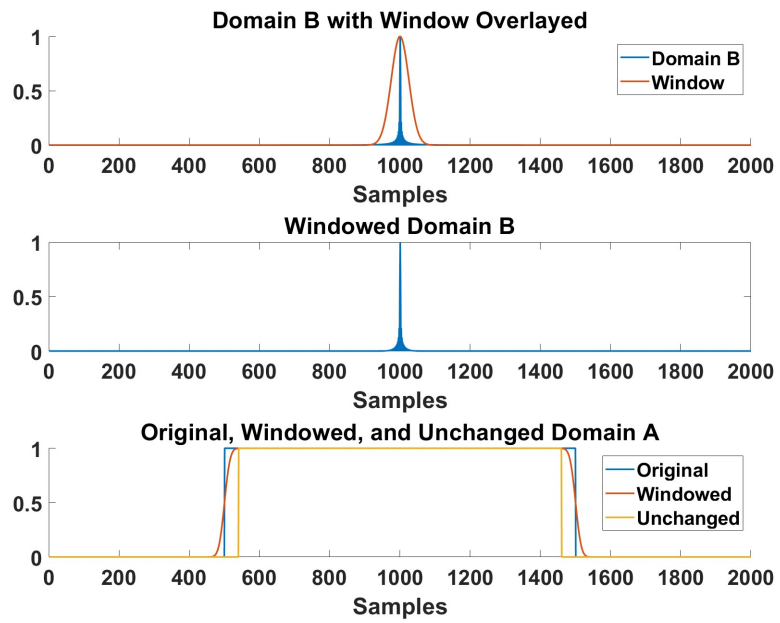
Figure 3.10: Using a wide window tapers domain A less
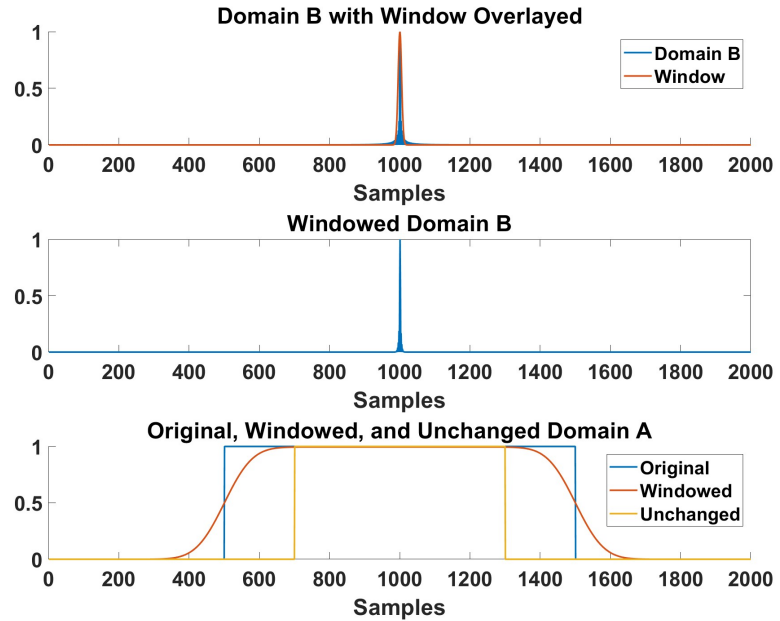
Figure 3.11: Using a narrow window tapers domain A more

Now that the tapering has been discussed, a performance evaluation of some common windows will be made. The primary performance consideration is the minimization of ripple. In order to ensure an accurate RCS measurement, the windowed result must be mostly flat along the top. Some common windows were chosen for the comparison, including the Gaussian, Hanning, Blackman, Hamming, and Tukey windows [15]. Figure 3.12 shows the results of windowing a sinc function with these windows and taking a DFT. Immediately it is clear that some of the windows have noticeable ripple throughout the response. Zooming into one of the corners provides a clearer view of the results, which is shown in Figure 3.13. With a better view, it appears as if a tradeoff exists between the amount of ripple and the width of the taper. The Hanning,
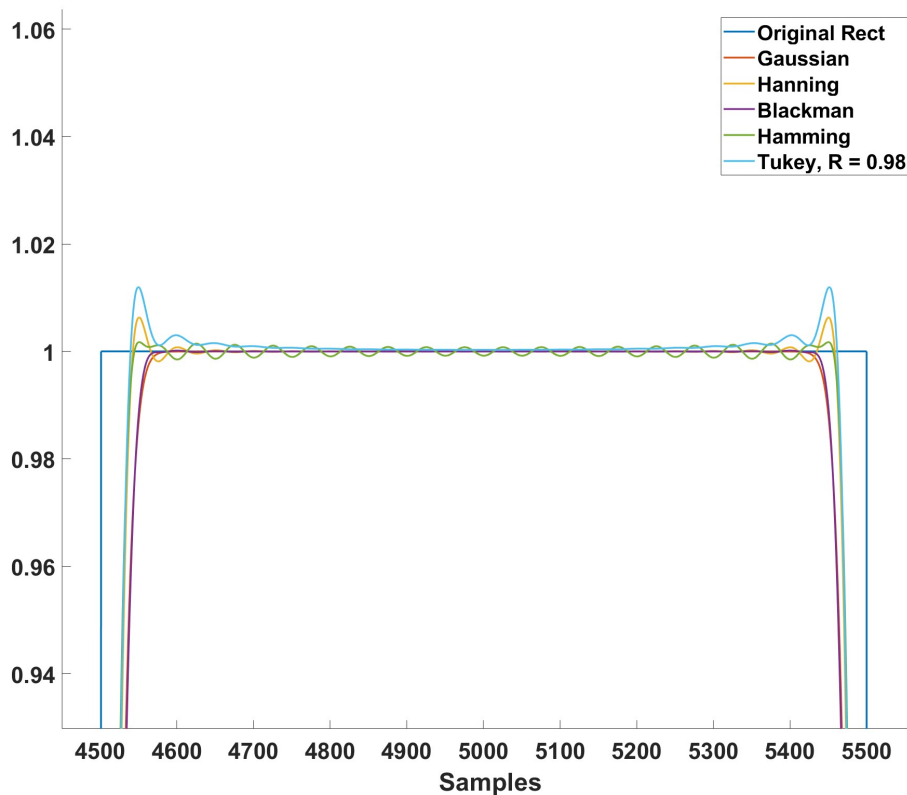
Figure 3.12: Window comparison showing a zoomed-in view of the top

38
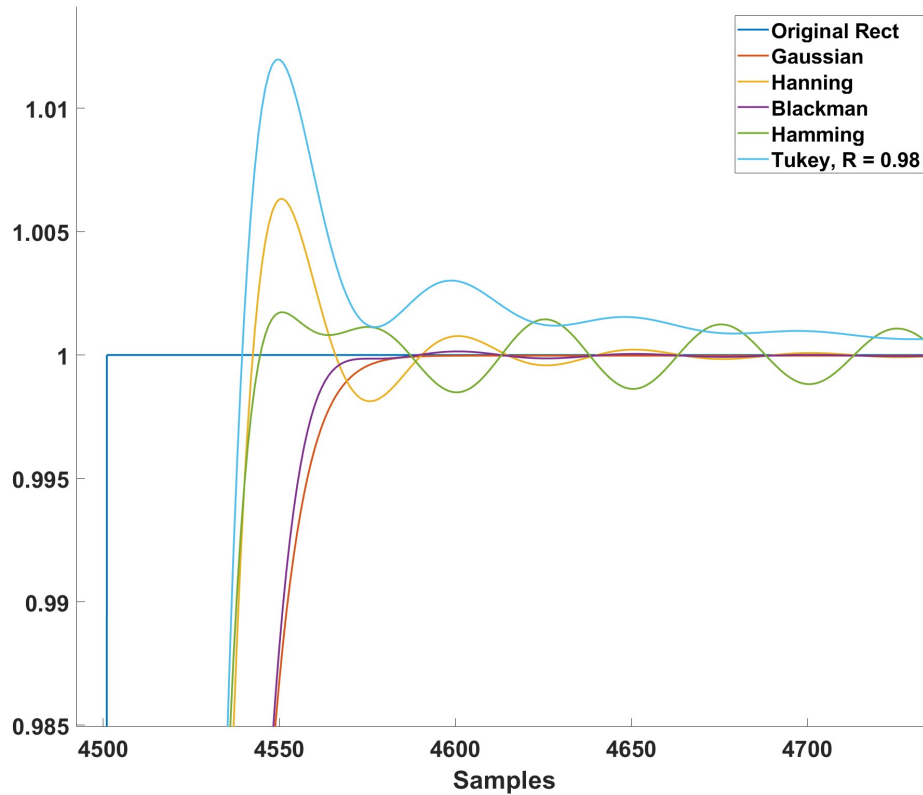
Figure 3.13: Window comparison zoomed-in on one of the corners

Hamming, and Tukey windows have a smaller taper than the other windows, but they suffer from ripple. Conversely, the Blackman and Gaussian windows have a wider taper but less ripple.

The tradeoff between taper and ripple is somewhat expected considering the extreme case of a rectangular window, which yields very little taper but has intense ripple. The result of using a rectangular window is shown in Figure 3.14 for completeness. With these considerations in mind, the window of choice is the Gaussian window. Although the Gaussian has the widest taper, it is still acceptable and satisfies the primary requirement of minimal ripple. In addition to this, the Gaussian function is well-known and should be easy to work with. The MATLAB implementation of the Gaussian win-

dow is given by

$$x(n) = \exp\left(-\frac{1}{2}\left(\alpha \frac{n}{(L-1)/2}\right)^2\right) \qquad (3.7)$$

where L is the window length and α is the "width factor." An alternate form is given as

$$x(n) = \exp\left(-\frac{n^2}{2\sigma^2}\right) \qquad (3.8)$$

where $\sigma = (L-1)/(2\alpha)$ is the standard deviation. Figure 3.15 illustrates how the shape of the window is affected by α, which will be tweaked frequently to obtain optimal RCS extraction.
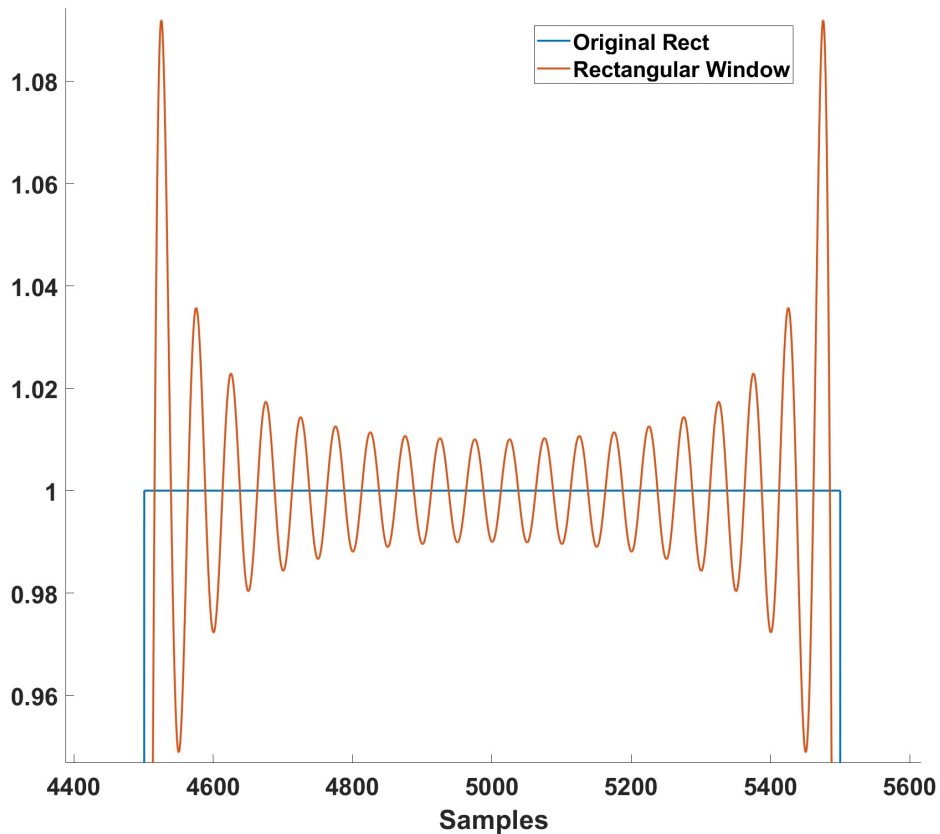
Figure 3.14: Illustration of ripple that results from using a rectangular window
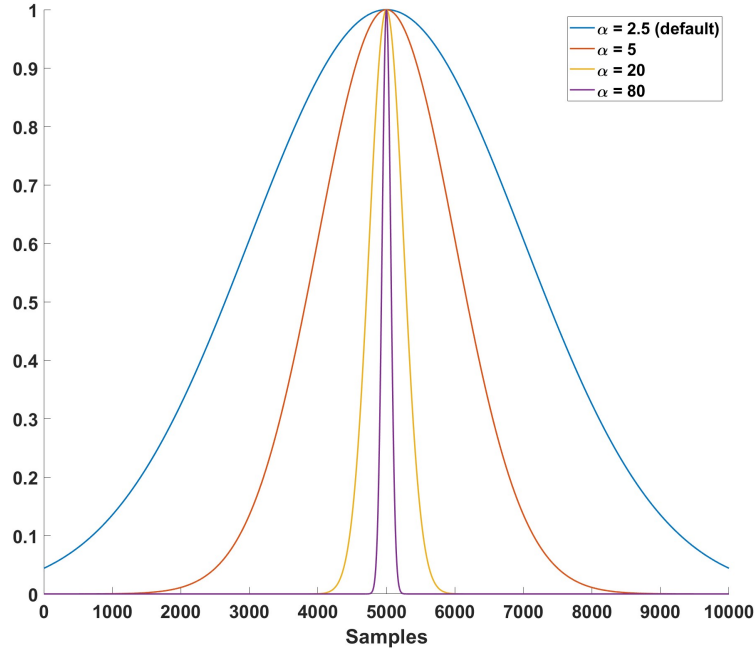
Figure 3.15: Increasing the width factor α makes the Gaussian window narrower

3.3 RCS Extraction

After filtering, the data is transformed back to its original form and (2.9) is used to extract RCS, which is repeated here for convenience.

$$\sigma = \frac{P_r(4\pi)^3 R^4 L}{P_t G_t G_r \lambda^2} \tag{3.9}$$

A big caveat is that in simulation, the variables are explicitly known. In reality, there needs to be some sort of calibration procedure so that parameters such as antenna gain and system losses are accurately represented. Section 3.5 discusses some of these practical considerations in more detail. In this section, we will assume that the system characteristics are well-known and that the radar range equation can be solved directly.

Table 3.2 gives parameters for a new simulation scenario. Note that the SINR listed

41

is the post-processing SINR. After using the processing techniques discussed in Section 2.5, the RDM of Figure 3.16 is obtained. From this point, a Gaussian window is applied in both the range and Doppler dimensions in order to isolate the target's energy. For this filtering, width factors of $\alpha_r = 40$ and $\alpha_d = 250$ were used for the range and Doppler dimensions respectively. Figure 3.17 shows the filtered RDM result after applying the Gaussian windows. From this point the processing is undone, that is, a DFT is taken across the range dimension and an IDFT across Doppler. The result of this backwards processing is shown in Figure 3.18. The effects of the windowing are clear; across both subcarriers and symbols there is a taper at the edges. In addition to the taper, there is also a decrease in power across subcarriers moving from top to bottom. This primarily relates to the RCS of the sphere, since over this bandwidth the RCS is decreasing with increasing frequency. The final step is to take the average complex voltage of each subcarrier (so averaging across the symbol dimension) and convert to power, which is used to solve RCS. Of course, the tapered region is not used when taking the average to ensure accurate results. Before averaging however, the Doppler shift of the target must be undone. To do this, the Doppler shift must be estimated. A good method for estimating the Doppler shift is discussed later in this chapter. The results after using (3.9) to solve for RCS are given in Figure 3.19 in units of dBsm.

Table 3.2: Example Scenario 2 Parameters

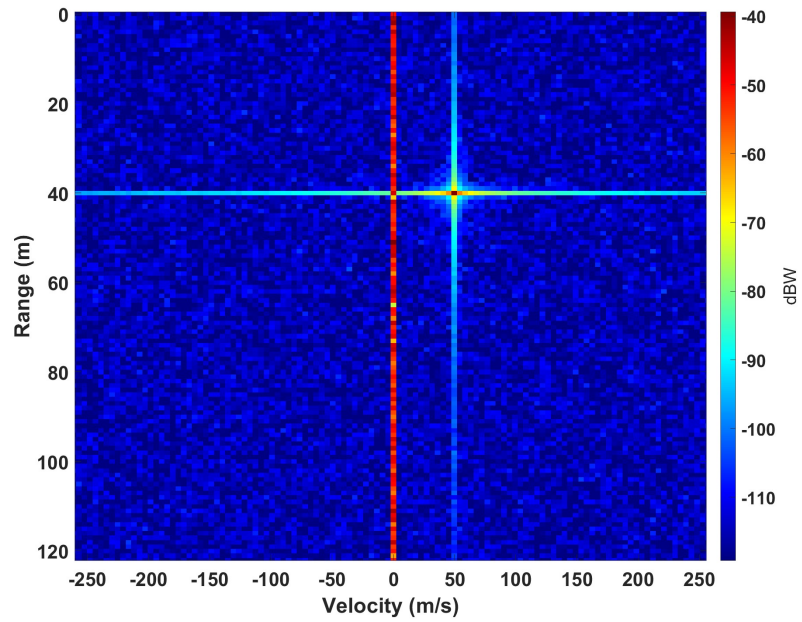| System Parameters		OFDM Parameters	
Parameter	Value	Parameter	Value
P_{peak}	100 W	BW	150 MHz
f_c	5 GHz	Δf	200 kHz
G_t	40 dB	T_{cp}	4.5 μs
G_r	40 dB	T_c	$\frac{1}{\Delta f} = 5\ \mu s$
L_s	6 dB	T_{OFDM}	$T_{cp} + T_c = 9.5\ \mu s$
f_s	150 MHz	N_{sym}	700
$SINR$	10 dB	-	-
F	8 dB	-	-

Figure 3.16: Example 2 zoomed-in range-Doppler map, $R = 40$ m, $v = 50$ m/s

Figure 3.17: Example 2 filtered range-Doppler map, $\alpha_r = 40$, $\alpha_d = 250$

Figure 3.18: Example 2 filtered data with processing undone for $\alpha_d = 250$
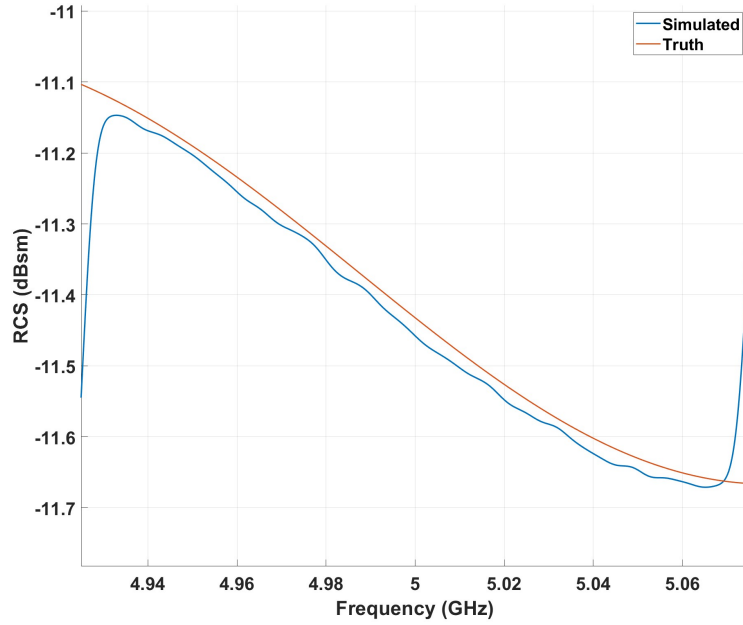
Figure 3.19: Example 2 RCS extraction result for $\alpha_d = 250$, simulated values (blue) and truth values (red)

44

The results show that we have indeed extracted the general shape of the target's RCS, however there is some error (ignoring the edge tapering, which has been established is a result of the windowing) in the form of a bias. This bias is due to Doppler bin straddling. We can try to correct this by going back and adjusting the width factor in the Doppler dimension, which will be changed to $\alpha_d = 80$. Figures 3.20, 3.21, and 3.22 show the filtered RDM, unprocessed RDM, and RCS extraction results for the new width factor, respectively. These results show that the extracted RCS is much closer to the true value on average; however, widening the window has also allowed energy from the clutter region into the signal, which means we may have just compensated with clutter power (which clearly isn't acceptable). A better bin straddling solution may be to simply add 'ones' to the top of the Gaussian window, thus creating a window with a flat top. However, there may not be enough Doppler bins to include the flat top and also attenuate the clutter properly.
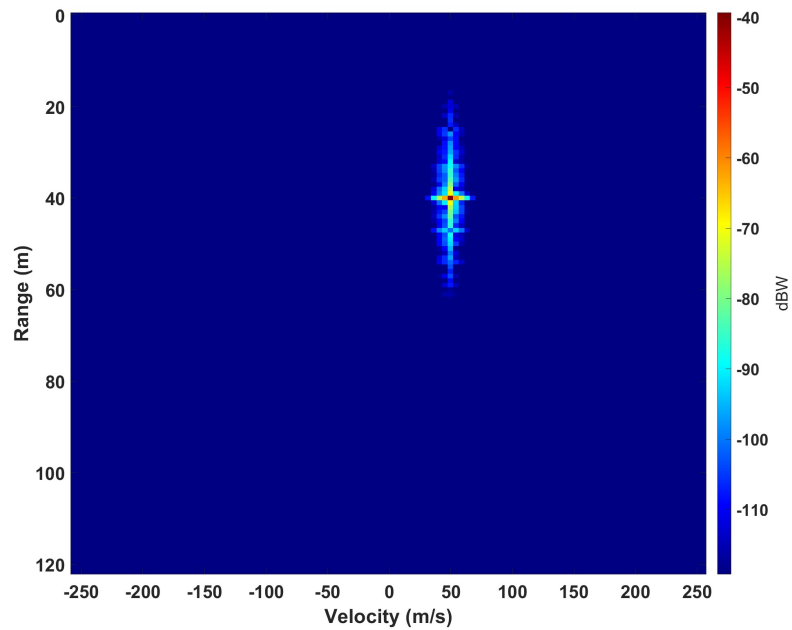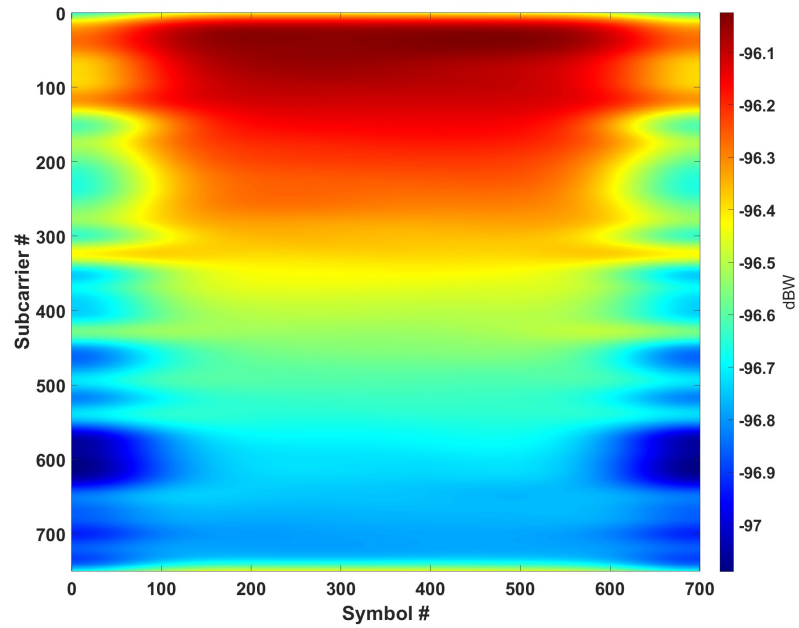

Figure 3.20: Example 2 filtered range-Doppler map, $\alpha_r = 40$, $\alpha_d = 80$

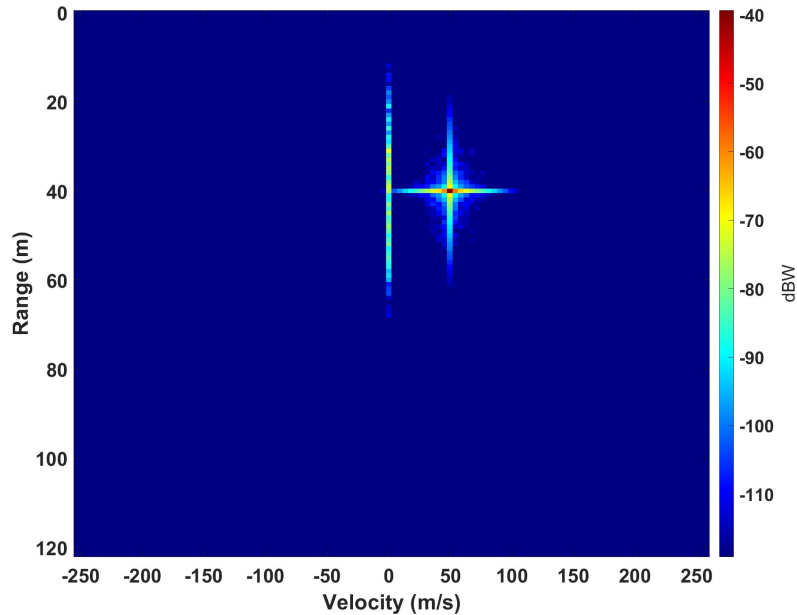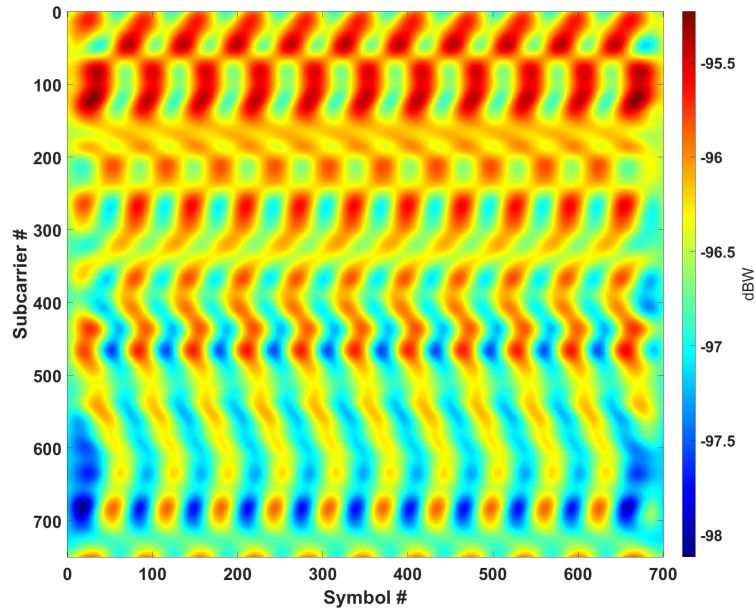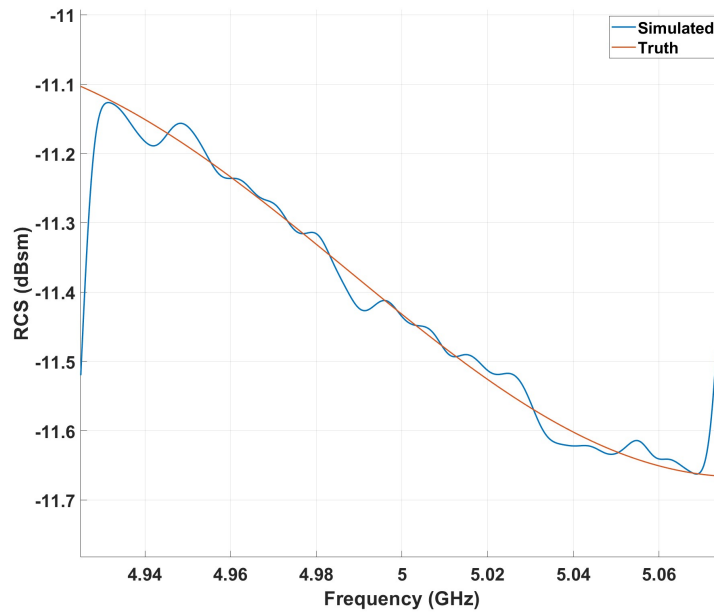Figure 3.21: Example 2 filtered data with processing undone for $\alpha_d = 80$

Figure 3.22: Example 2 RCS extraction result for $\alpha_d = 80$, simulated values (blue) and truth values (red)

Let us now consider a scenario with less ideal parameters. Table 3.3 gives the parameters for this new scenario. The peak power has been dropped from 100 W to 10 W, and the target range has been moved up to 115 m. These two changes have the combined effect of greatly lowering the SNR. In addition, the post-processing SINR has been set to 0 dB, and the Doppler width factor has been set to $\alpha_d = 200$. Figure 3.23 shows that the simulated RCS measurement has been degraded as a result of the decreased SNR and SINR. The best way to combat this is to increase the coherent processing interval (CPI), that is, increase the number of symbols. The CPI, T, is given by $T_{OFDM} N_{sym}$, which in all of the previous examples has been $(9.5\mu s)(700) = 6.65ms$. Increasing the CPI will address both the SNR and SINR issues. The SNR will be improved because increasing the number of symbols raises the target processing gain. In the case of SINR, more symbols provides finer Doppler resolution, thus making it easier to separate the target from clutter. Increased Doppler resolution also decreases windowing error that results from the target straddling Doppler bins. As mentioned earlier, a flat top window may be a solution to bin straddling; however, another technique is presented in the next section to compensate for this effect. Figure 3.24 shows the simulation result of increasing N_{sym} to 14000, which yields a coherent processing interval of $(9.5\mu s)(14000) = 133ms$.

Table 3.3: Example Scenario 3 Parameters

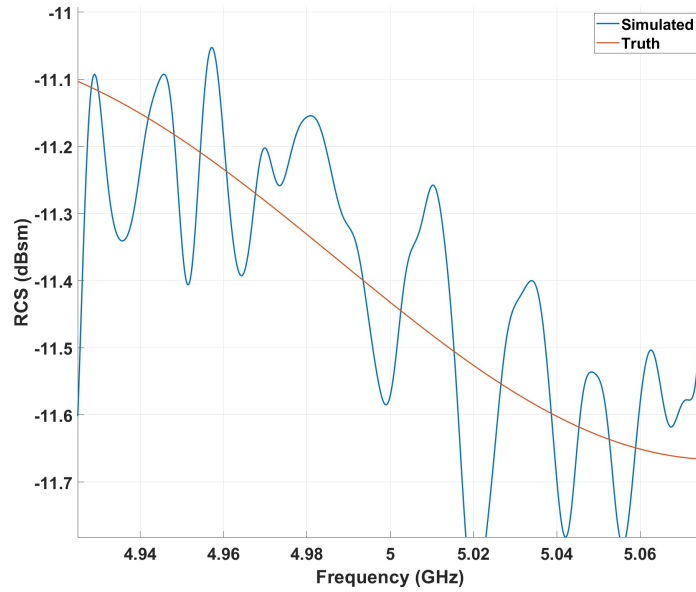| System Parameters		OFDM Parameters	
Parameter	Value	Parameter	Value
P_{peak}	10 W	BW	150 MHz
f_c	5 GHz	Δf	200 kHz
G_t	40 dB	T_{cp}	4.5 μs
G_r	40 dB	T_c	$\frac{1}{\Delta f} = 5 \; \mu s$
L_s	6 dB	T_{OFDM}	$T_{cp} + T_c = 9.5 \; \mu s$
f_s	150 MHz	N_{sym}	700
$SINR$	0 dB	-	-
F	8 dB	-	-

Figure 3.23: Example 3 RCS extraction result for $\alpha_d = 200$, $R = 115$ m, $v = 50$ m/s, simulated values (blue) and truth values (red)
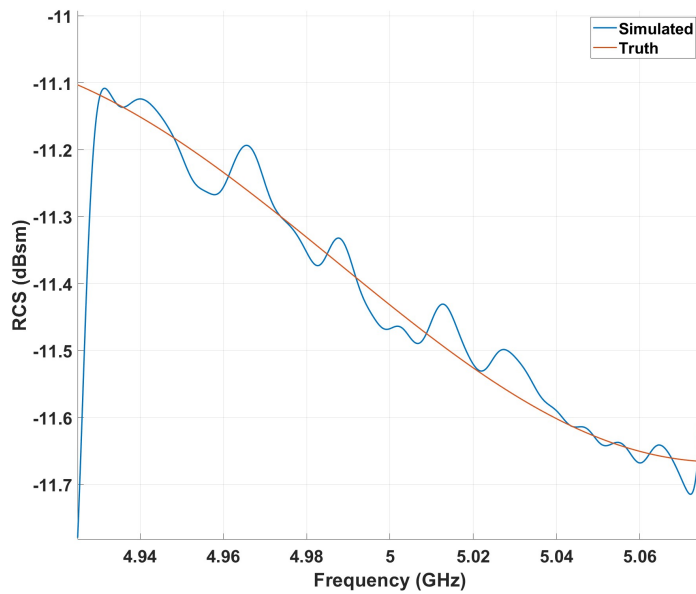

Figure 3.24: Example 3 RCS extraction result after raising CPI, $N_{sym} = 14000$, $\alpha_d = 200$, simulated values (blue) and truth values (red)

3.4 Further Analysis

3.4.1 Helpful Equations

This section is dedicated to deriving equations that aim to assist with RCS extraction performance. Let us first consider that we wish to perform a real-world test of the techniques discussed in this work. In order to do so, a controlled velocity must be established for the target being measured, but how fast should the target be moving? In other words, what is the minimum velocity required to effectively distinguish the target from ground clutter? This is primarily a question about the shape of our window and the available Doppler resolution. Let us begin with (3.7), which is repeated here for convenience

$$x(n) = \exp\left(-\frac{1}{2}\left(\alpha\frac{n}{(L-1)/2}\right)^2\right) = \exp\left(-\frac{n^2}{2\sigma^2}\right). \tag{3.10}$$

The first step is to establish the desired attenuation of the clutter region. Let the clutter attenuation A in dBW be given by

$$A = -20\log_{10}(x(n)) = -20\log_{10}\left(\exp\left(-\frac{n^2}{2\sigma^2}\right)\right). \tag{3.11}$$

Notice that the window is treated as a voltage quantity because windowing is applied to voltages. The goal now is to solve for the value of n that gives the desired attenuation. Dividing A by 20 and undoing the logarithm yields

$$10^{-A/20} = e^{-n^2/(2\sigma^2)}. \tag{3.12}$$

Taking the natural logarithm of both sides, rearranging some terms, and using a log rule

49

yields

$$\frac{2\ln(10)A\sigma^2}{20} = n^2. \tag{3.13}$$

After rearranging and substituting $\sigma = (L-1)/2\alpha$, we obtain

$$n = \frac{L-1}{2\alpha}\sqrt{0.1\ln(10)A} \tag{3.14}$$

which gives the value of n that is required to achieve the desired attenuation A given the width factor α and window size L.

Although (3.14) is already helpful, it is not in a form that means anything physically, that is, we still need to incorporate our system parameters. To do this, n will be converted to v_{min}, the minimum velocity that achieves the desired clutter attenuation. In a previous section it was mentioned that the resolution of the velocity axis is given by $2|v_{ua}|/N_{sym}$, where v_{ua} is the unambiguous velocity defined in (3.3). Given the Doppler resolution, the minimum velocity v_{min} is then given by

$$v_{min} = n\frac{2|v_{ua}|}{N_{sym}} = \frac{n\lambda_c}{2T_{OFDM}N_{sym}}. \tag{3.15}$$

In this form, the value of n is continuous, meaning that the discrete nature of the velocity axis is not represented. To fix this, the value of n should be rounded either up or down. In this case, n will be rounded up so that the desired attenuation is achieved. Because of this, the realized clutter attenuation will be higher than A. As the Doppler resolution increases (N_{sym} increases), the realized attenuation will approach A. Given this change, (3.15) becomes

$$v_{min} = \frac{\lceil n \rceil \lambda_c}{2T_{OFDM}N_{sym}}. \tag{3.16}$$

50

where $\lceil \rceil$ is the ceiling function. Adding this into (3.14) and substituting N_{sym} for L results in

$$v_{min} = \frac{\lambda_c}{2T_{OFDM}N_{sym}} \left\lceil \frac{N_{sym} - 1}{2\alpha} \sqrt{0.1\ln(10)A} \right\rceil \qquad (3.17)$$

It may also be helpful to solve for other variables, which is easily accomplished by rearranging (3.17). The window width factor is then given as

$$\alpha = \frac{N_{sym} - 1}{2 \left\lfloor \frac{2vT_{OFDM}N_{sym}}{\lambda_c} \right\rceil} \sqrt{0.1\ln(10)A} \qquad (3.18)$$

and the clutter attenuation by

$$A = \frac{10}{\ln(10)} \left(\frac{2\alpha \left\lfloor \frac{2vT_{OFDM}N_{sym}}{\lambda_c} \right\rceil}{N_{sym} - 1} \right)^2 \qquad (3.19)$$

where $\lfloor \rceil$ denotes rounding.

Another highly beneficial derivation to perform is the closed-form expression for the windowed Doppler response. This will be used to compensate for the Doppler bin straddling loss that was seen in a previous section. The first step in the derivation is to find the unwindowed Doppler response. Recall from (2.29) that the values for the Doppler vector are given by

$$k_D(n) = \exp\left(j2\pi n T_{OFDM} f_D\right). \qquad (3.20)$$

Note that we are assuming the true Doppler shift, f_D, is known. We will later discuss a method of estimating the true Doppler shift (this method is used in all of the simulation

results). The unwindowed Doppler response is then given by the DFT of (3.20)

$$
\begin{aligned}
K_D(m) &= \frac{1}{\sqrt{N_{sym}}} \sum_{n=0}^{N_{sym}-1} k_D(n) e^{\frac{-j2\pi mn}{N_{sym}}} \\
&= \frac{1}{\sqrt{N_{sym}}} \sum_{n=0}^{N_{sym}-1} e^{j2\pi n T_{OFDM} f_D} e^{\frac{-j2\pi mn}{N_{sym}}} \\
&= \frac{1}{\sqrt{N_{sym}}} \sum_{n=0}^{N_{sym}-1} e^{j2\pi n (T_{OFDM} f_D - m/N_{sym})} \\
&= \frac{1}{\sqrt{N_{sym}}} \sum_{n=0}^{N_{sym}-1} \left[e^{j2\pi (T_{OFDM} f_D - m/N_{sym})} \right]^n
\end{aligned}
\tag{3.21}
$$

Now consider the following summation formula

$$
\sum_{k=0}^{n} a^k = \frac{1 - a^{n+1}}{1 - a}, \; a \neq 1
\tag{3.22}
$$

which when applied to (3.21) yields

$$
K_D(m) = \frac{1}{\sqrt{N_{sym}}} \frac{1 - e^{j2\pi (T_{OFDM} f_D - m/N_{sym}) N_{sym}}}{1 - e^{j2\pi (T_{OFDM} f_D - m/N_{sym})}}.
\tag{3.23}
$$

Letting $\beta = T_{OFDM} f_D - m/N_{sym}$ and performing some manipulations gives

$$
\begin{aligned}
K_D(m) &= \frac{1}{\sqrt{N_{sym}}} \frac{1 - e^{j2\pi\beta N_{sym}}}{1 - e^{j2\pi\beta}} = \frac{1}{\sqrt{N_{sym}}} \frac{e^{j\pi\beta N_{sym}} \left(e^{-j\pi\beta N_{sym}} - e^{j\pi\beta N_{sym}} \right)}{e^{j\pi\beta} \left(e^{-j\pi\beta} - e^{j\pi\beta} \right)} \\
&= \frac{1}{\sqrt{N_{sym}}} \frac{-2j \sin(\pi\beta N_{sym}) e^{j\pi\beta N_{sym}}}{-2j \sin(\pi\beta) e^{j\pi\beta}} \\
&= \frac{1}{\sqrt{N_{sym}}} \frac{\sin(\pi\beta N_{sym})}{\sin(\pi\beta)} e^{j\pi\beta (N_{sym}-1)}
\end{aligned}
\tag{3.24}
$$

Finally, substituting the value for β back into (3.24) gives the equation for the unwin-

dowed Doppler response

$$K_D(m) = \frac{1}{\sqrt{N_{sym}}} \frac{\sin(\pi T_{OFDM} f_D N_{sym} - \pi m)}{\sin(\pi T_{OFDM} f_D - \pi m/N_{sym})} e^{j\pi(T_{OFDM} f_D - m/N_{sym})(N_{sym}-1)}$$

(3.25)

The windowing function (3.10) will now be applied to (3.25), but first a couple tweaks need to be made to the windowing function. First, n should be shifted by $-\lceil(N_{sym} - 1)/2\rceil$ to ensure a symmetric response. The ceiling function ensures that the peak of the window is always being sampled, otherwise there would be a large loss of energy. In addition to the shift applied to n, the full window vector is circularly shifted by C cells to the peak of the Doppler response, with C given by m in (2.35). The values of the windowing function are then given by

$$x(n) = e^{-0.5\left(\alpha\left(\frac{n - \lceil \frac{N_{sym}-1}{2}\rceil}{(N_{sym}-1)/2}\right)\right)^2}$$

(3.26)

At last, the windowed Doppler response is given as a vector by

$$\mathbf{W_D} = \mathbf{K_D} \odot (\mathbf{x})_C$$

(3.27)

where $\mathbf{K_D}$ is the vector formed by values of $K_D(m)$ from $m = 0$ to $N_{sym} - 1$, $\mathbf{x}$ is the vector formed by values of $x(n)$ from $n = 0$ to $N_{sym} - 1$, $()_C$ denotes circular shifting, and $\odot$ denotes element-wise multiplication.

The windowed Doppler response given by (3.27) is helpful for determining the energy lost from the windowing process. Let the energy of a signal $x[n]$ be given by

$$E_x = \sum_{n=-\infty}^{\infty} |x[n]|^2.$$

(3.28)

The energy of $\mathbf{W_D}$ is thus given by

$$E_W = \sum_{i=0}^{N_{sym}-1} |W_{D_i}|^2.$$ (3.29)

where W_{D_i} is the ith element of $\mathbf{W_D}$. The *percent energy lost* by windowing is then one minus the ratio of the energy in the windowed response to the original response

$$E_{lost} = \left[1 - \frac{\sum_{i=0}^{N_{sym}-1} |W_{D_i}|^2}{\sum_{i=0}^{N_{sym}-1} |K_{D_i}|^2} \right] \times 100.$$ (3.30)

Although (3.30) gives an idea of how much energy of the response is being windowed out, it doesn't say anything about where this is occurring in the opposite domain. That is, in the opposite domain the lost energy mostly comes from the tapered edges (as it was seen in Section 3.2). We mostly care about the energy lost *between* the edges, so to find the answer to this an IDFT of (3.27) needs to be taken. After that, the magnitude of the central part of the response is used to correct windowing errors that result from bin straddling. An example of this is provided in Figure 3.25, which shows the magnitude of the IDFT of (3.27). Notice that the peak of the central part of the response is well below one, which indicates bin straddling. In a case where there is no bin straddling, the peak would be very close to one. With this information, we can simply adjust the RCS measurement using the different between one and the peak of the response.

Throughout the previous derivation, we have assumed that we know the true Doppler shift of the target. Of course, we don't know the true value in reality; we only know an estimation based on our discrete Doppler samples. A good Doppler estimate will not only ensure that our bin straddling compensation technique is usable, but also that we can undo the target Doppler shift for the averaging operation across symbols (which is a part of the RCS extraction process discussed in a previous section). Luckily, [7] pro-
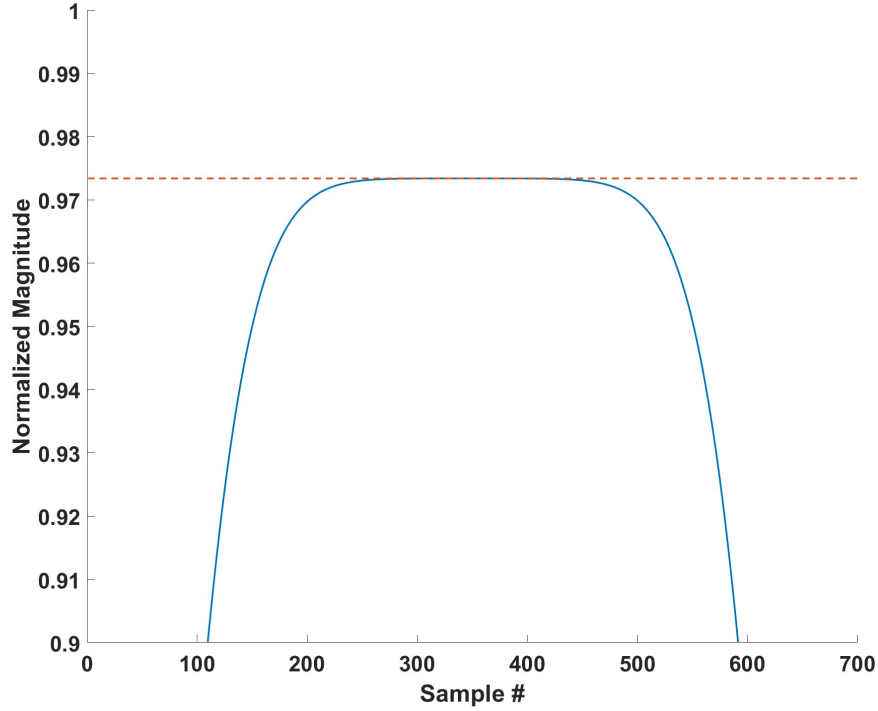
Figure 3.25: Peak magnitude (dotted line) of the IDFT of (3.27) is below one for bin straddled target

vides an excellent Doppler shift estimation technique for a critically sampled Doppler response. Given the bin location of the peak of the Doppler response, the true Doppler shift can be estimated using a quadratic interpolation. We start by estimating the (likely non-integer) bin corresponding to the peak of the interpolated response:

$$b' = b_0 + \Delta b = b_0 + Re\left\{\frac{R[b_0+1] - R[b_0-1]}{R[b_0-1] - 2R[b_0] + R[b_0+1]}\right\} \qquad (3.31)$$

where b_0 is the bin corresponding to the peak of the complex voltage response R, and b' is the bin corresponding to the peak of the interpolated response. We can then convert b' from a bin number to frequency, which yields the estimated Doppler shift.

To quickly demonstrate the usefulness of the derived equations, let us consider a

new scenario with parameters given by Table 3.4. Consider that on receive, a target at approximately 40 m in range moving at 24 m/s has been located. In addition, assume that we wish to use a Doppler window with $\alpha_d = 300$. Using (3.19), the approximate attenuation of the clutter region is given as 96.7 dBW. This clutter attenuation should be more than enough, given that our post-processing SINR is 0 dB. Figures 3.26, 3.27, 3.28, and 3.29 give the RDM, range/Doppler profiles, filtered RDM, and RCS extraction results respectively. Notice that in Figure 3.29, the simulated RCS values are slightly off as a result of the narrow window. From our previous analysis however, we are able to compensate for the lost energy in the middle part of the response, which gives a result that is centered better around the true values. A big caveat, however, is that as the window becomes narrower this adjustment will grow to be inaccurate. So, in order to ensure that the adjustment is better than the measured result, the Doppler window must not be too narrow. As a general rule of thumb, the Doppler window width factor should be kept below 1000.

Despite mathematical compensation being a successful strategy for alleviating straddle loss, it may not be the best strategy computationally. Instead, it was alluded to previously that a better approach might be to create a hybrid window that has a flat top and Gaussian tapered edges. The flat top ensures that there is no straddle loss without having to jump through mathematical hoops. It is also important to consider that bin straddling can occur in the range dimension as well. If the target spans multiple range bins over the duration of the CPI, then a flat top will be necessary to retain all of the target information. However, in the case of Doppler filtering, there may not be enough resolution between the target and clutter to use a flat top window. These decisions are ultimately specific to the application and scenario.

Table 3.4: Example Scenario 4 Parameters

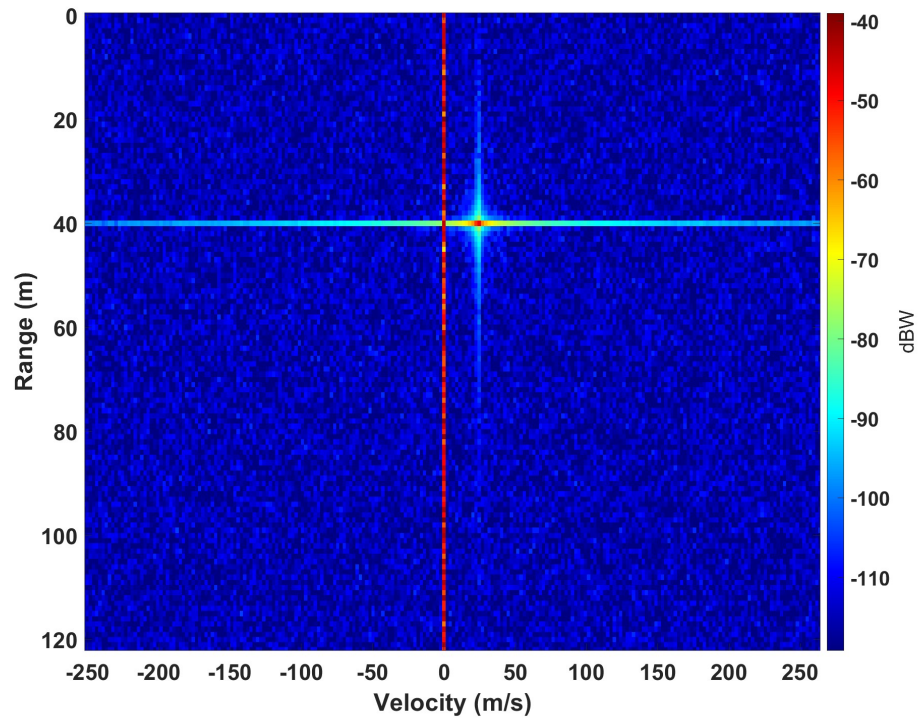| System Parameters		OFDM Parameters	
Parameter	Value	Parameter	Value
P_{peak}	10 W	BW	150 MHz
f_c	5 GHz	Δf	200 kHz
G_t	40 dB	T_{cp}	4.5 μs
G_r	40 dB	T_c	$\frac{1}{\Delta f} = 5\ \mu s$
L_s	6 dB	T_{OFDM}	$T_{cp} + T_c = 9.5\ \mu s$
f_s	150 MHz	N_{sym}	1400
$SINR$	0 dB	-	-
F	8 dB	-	-

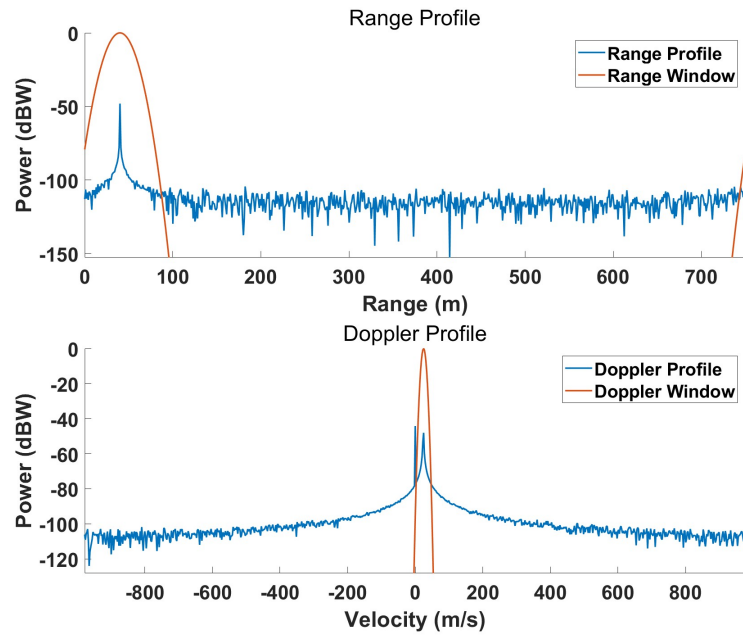Figure 3.26: Example 4 range-Doppler map, $R = 40$ m, $v = 24$ m/s

Figure 3.27: Example 4 range and Doppler profiles (blue) with windows overlaid (red), $\alpha_r = 40$, $\alpha_d = 300$
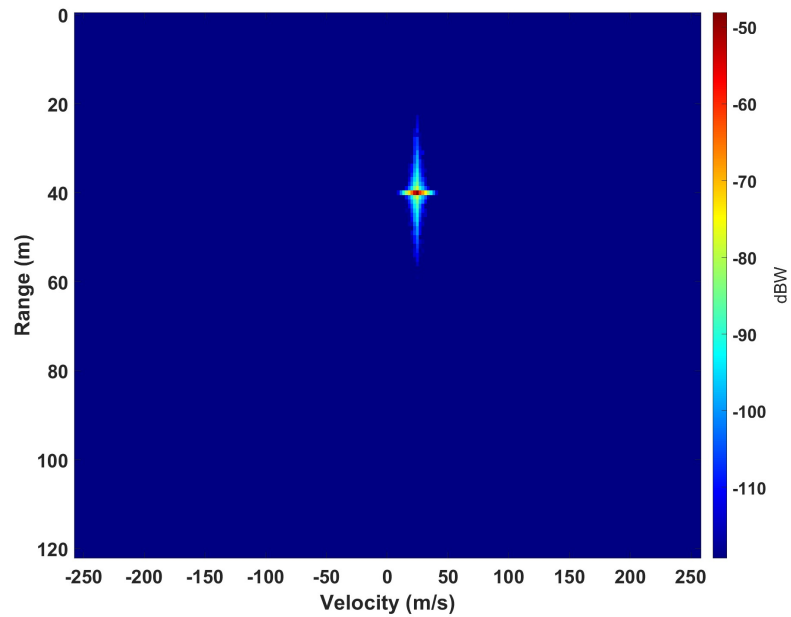

Figure 3.28: Example 4 filtered range-Doppler map, $\alpha_r = 40$, $\alpha_d = 300$
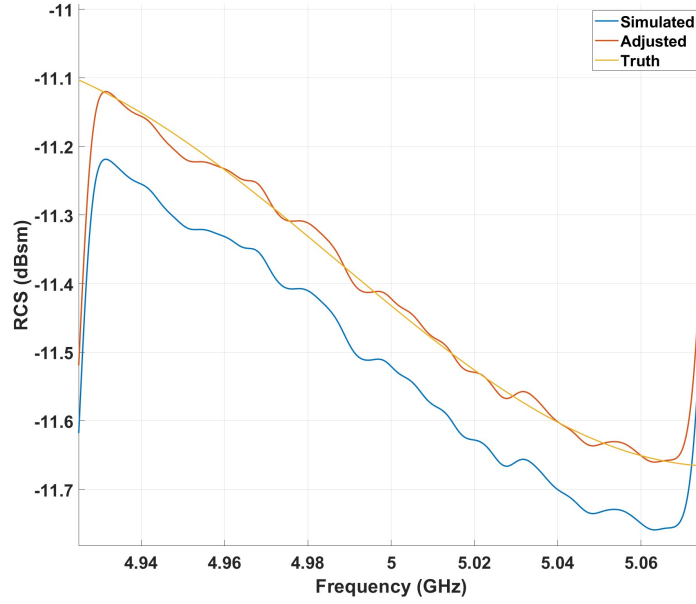
Figure 3.29: Example 4 RCS extraction result, simulated values (blue), adjusted values (red), true values (yellow)

3.4.2 SNR Performance Evaluation

An additional test was run to determine the performance for a given SNR. For the test, ground clutter has been removed and the targets are stationary ($v = 0$ m/s). The percent error in the simulated RCS measurement is plotted against the window width factor, α, which is swept for both the range and Doppler dimensions simultaneously. The percent error is given as

$$\%Error = \frac{|\sigma_{truth} - \sigma_{sim}|}{\sigma_{truth}} \times 100 \qquad (3.32)$$

where σ_{truth} and σ_{sim} are the true and simulated RCS values in m^2, respectively. Note that (3.32) gives the percent error for a single frequency bin, but since the percent error can fluctuate across bins, the *average* percent error is used. Figure 3.30 gives

the average percent error versus α for different post-processing SNRs. For the test, the number of symbols is equal to the number of subcarriers, and the window width factors for range and Doppler dimensions are also kept equal to each other. It can be seen that for high/medium SNRs, slight windowing is helpful, although at a certain point windowing has a negative impact. This is expected since the SNR is already quite good, so windowing is mainly going to discard target information. For lower SNRs, it can be seen that windowing becomes much more important, although there are diminishing returns as the windows become increasingly narrow.
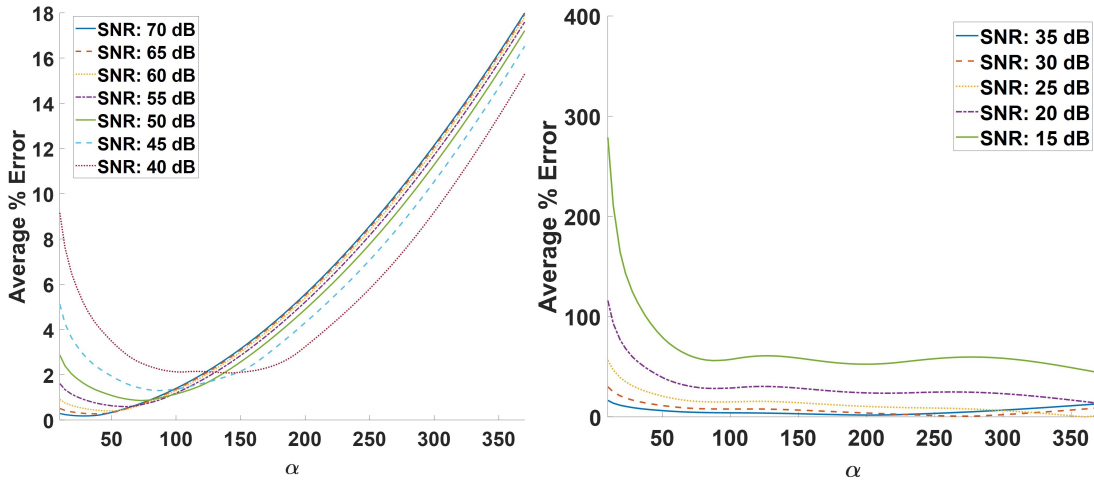

Figure 3.30: RCS percent error versus window width factor α for medium/high SNRs (left) and low SNRs (right), $N_{sub} = N_{sym} = 750$

These results provide some general insight, but it is more beneficial to look at SNR as a function of specifically range or Doppler window width. That is, we will perform the same test two more times but hold one of the windowing dimensions constant. Figure 3.31 shows the results from holding the Doppler window constant and sweeping the range window width. Figure 3.32 shows similar results, but for holding the range window constant and sweeping the Doppler window width. From these results, we can see that the Doppler window width has little impact on the average percent error. This
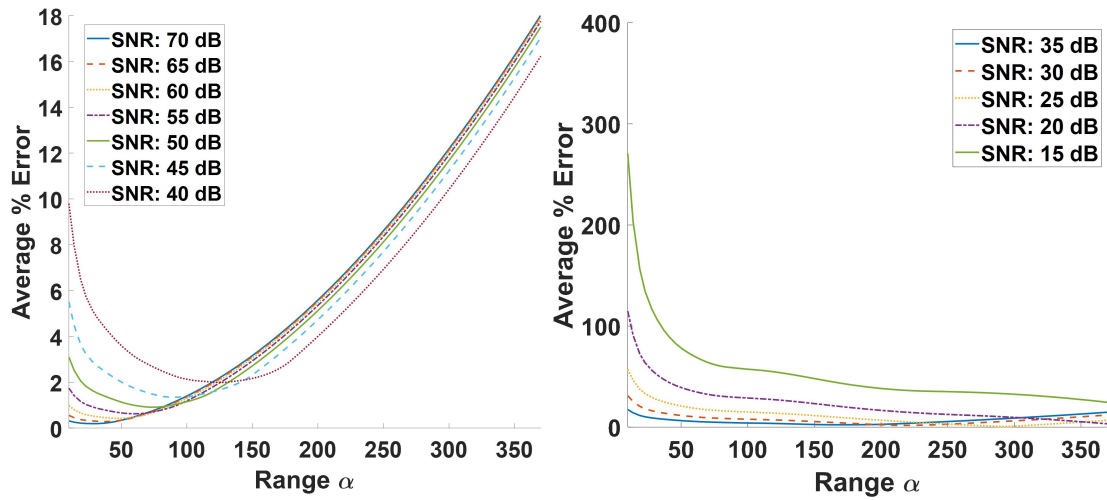
Figure 3.31: RCS percent error versus range window width factor α for medium/high SNRs (left) and low SNRs (right), $N_{sub} = N_{sym} = 750$, Doppler alpha set to 100
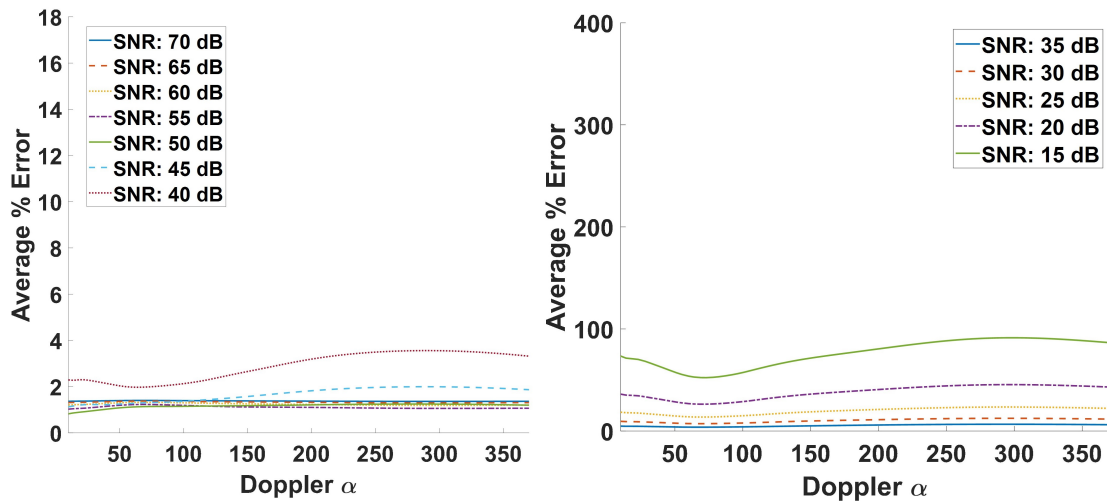

Figure 3.32: RCS percent error versus Doppler window width factor α for medium/high SNRs (left) and low SNRs (right), $N_{sub} = N_{sym} = 750$, range alpha set to 100

is a sensible result, considering that we are taking an average across the symbols as part of the RCS extraction process, which averages out noise in the Doppler dimension. The range window is thus the primary tool for influencing the RCS extraction result in the face of poor SNR.

Some additional insight about what the range window is doing can be gained from

61

looking at a specific scenario and modifying the range window width while holding the Doppler width constant. Figure 3.33 illustrates a specific scenario with a post-processing SNR of 33 dB. Each plot shows the result for a different range window width, with the width decreasing from left to right. As the window becomes narrower, we can see a smoothing behavior. This can be explained by considering that as the window becomes narrower, we are convolving in the other domain with a wider Gaussian. As a result, we are essentially applying a Gaussian smoothing filter to the result. This is helpful for reducing our measurement variance and eliminating noise; however, it should also be noted that the edge subcarrier taper increases as well. As a result, it is important to try to apply range filtering in moderation.
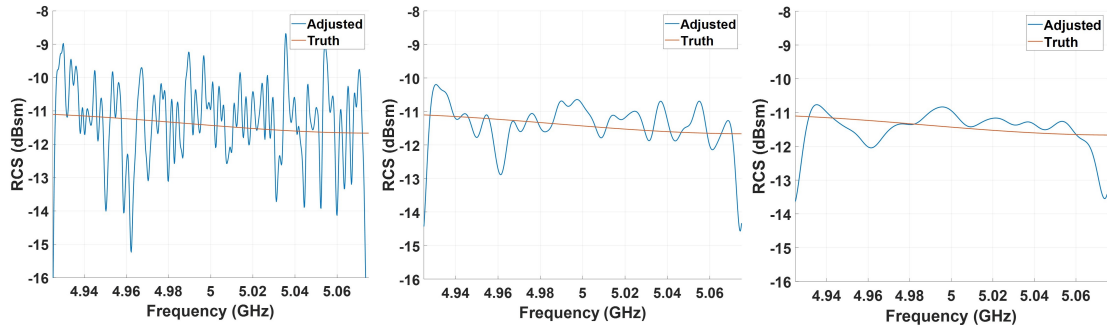

Figure 3.33: RCS extraction result for SNR of 33 dB, Doppler window held constant ($\alpha_d = 100$), range window $\alpha_r = 10$ (left), $\alpha_r = 40$ (middle), $\alpha_r = 80$ (right)

3.5 Practical Considerations

Before concluding this chapter, some comments will be given about practical considerations outside of the simulation environment. Although there are *many* considerations when it comes to a real-world test of the ideas presented in this work, the two that are most relevant have been chosen.

3.5.1 Calibration Object

The topic of a calibration object arises from the discussion of RCS extraction in Section 3.3. In simulation, the radar range equation can be used to solve for RCS explicitly because all of the variable are exactly known. Of course, in reality it is much more difficult to accurately know these variables. To work around this problem, an object with a *known* RCS is used for calibration. Using an object with a known RCS allows for the other variables to be solved for together as a single constant [2] [3]. To better illustrate this idea, consider the form of the radar range equation given in (2.8), which is repeated here for convenience.

$$P_r = \frac{P_t G_t G_r \lambda^2 \sigma}{(4\pi)^3 R^4 L} \tag{3.33}$$

Considering that the ratio of P_r to P_t is known from a vector network analyzer (VNA) measurement, (3.33) can be written as

$$\frac{P_r}{P_t} = \frac{G_t G_r \lambda^2 \sigma}{(4\pi)^3 R^4 L}. \tag{3.34}$$

The unknown variables can then be lumped into a single constant k, which is solved for using the calibration object

$$\frac{P_r}{P_t} = k\sigma. \tag{3.35}$$

The calculation of this constant is the first step to making accurate RCS measurements; however, the fact that the target for this work is moving means that there are challenges to overcome for the calibration process. As an example of one such challenge, assume that a radar system needs to be calibrated in an outdoor environment for tests. Further assume that we wish to give the calibration object some velocity to

63

separate it from the clutter zone. In order to move the calibration target in a controlled manner, it must be mounted to some type of vehicle that can hold a steady velocity. Additionally, the mounting structure and vehicle should be constructed in a way such that they do not interfere with the calibration measurement; this will require some considerable thought.

It is also important to remember that the calibration set will change as a function of range. This introduces a unique challenge, since the target will be at slightly different ranges across the duration of the CPI. If the calibration object is measured while moving, then it will be important that the calibration object ranges coincide with the target under test. Clearly, there are many considerations to the calibration procedure that will have to be analyzed prior to performing a real-world test.

3.5.2 Doppler Shift & Orthogonality

As it has been well established, a key component of the OFDM signal is the orthogonality of its subcarriers. Unfortunately, the Doppler shift imparted upon each subcarrier by target motion impacts this orthogonality by shifting each subcarrier. As such, it is important to consider the maximum allowable Doppler shift for a given subcarrier spacing. As a general rule of thumb to ensure orthogonality, the subcarrier spacing should be chosen such that $\Delta f > 10 f_{D,max}$, where $f_{D,max}$ is the maximum expected Doppler shift [4] [16]. As a quick example, recall that all of the previous scenarios presented in this work had a subcarrier spacing $\Delta f = 200$ kHz. This sets the maximum Doppler shift to 20 kHz, which corresponds to a maximum velocity $v_{max} = \frac{f_{D,max}\lambda_c}{2} = 600$ m/s for a radar with a center frequency of 5 GHz.

Chapter 4

Interference

Up to this point, it has been assumed that the spectrum is clear of competing signals. That is, there is no interference from other nearby transmitters. In reality, there may be parts of the spectrum that are corrupted by unwanted RF signals, most likely communications signals. This is especially true if operating near popular frequency bands for wireless broadband cellular networks such as 4G LTE and 5G. This chapter discusses a possible solution to this type of interference, how the solution affects the matched filter response, and how it impacts the RCS extraction result. Lastly, a possible technique for spectral reconstruction is presented.

4.1   Problem Statement

All of the previous examples in Chapter 3 have used a center frequency of 5 GHz and a bandwidth of 150 MHz, which we will maintain here. Assume that an outdoor test is being performed; during the test, the receiver intercepts some unknown communications transmission. Further assume that the interfering signal is much stronger than the reflected signal from the target under test (a reasonable assumption, especially if the interference is from a source in direct line of sight). For illustration purposes, let the interfering signal have a center frequency of 5.01 GHz with a bandwidth of 20

MHz. The amplitude of the interference is set to be 500 times stronger than the reflected signal from the target, which is a $20 \log_{10}(500) = 54$ dBW increase. Finally, the interfering signal is given random amplitude/phase modulations according to a 16-QAM modulation scheme. Of course, the data from the interfering signal need not be random (and mostly likely wouldn't be); however, the data modulations would likely *appear* "random" since the interfering transmitter is operating under a different set of system parameters. In other words, the receiver is not "lined up" with the interfering signal. Figure 4.1 provides a look at the raw data matrix (i.e., before radar processing) for this scenario, and Figure 4.2 gives the same data in a 3-dimensional view.

When taking a look at the data in this form, the interfering signal is clearly distinguishable from the rest of the data. However, it is important to remember that this data also contains the ground clutter information. That is, we still need to perform radar processing on the data, window out the clutter, and then return to this domain for RCS extraction. After radar processing the raw data matrix, we obtain the range-Doppler map shown in Figure 4.3. This is where the problem becomes apparent; there is no way to find the target because the interference is completely masking the important details. Of course, the ideal solution to this problem would be to take new measurements when the interference is not present. However, in situations where new measurements cannot be obtained, the data we have needs to be salvaged.

The proposed solution is quite intuitive, which is to simply null out the interference in the raw data matrix. What is meant by this is to observe the received data and set the data to zero at subcarriers where interference is believed to exist. Emphasis should be given to the fact that nulls are added to the received data *after* observation, i.e., we assume here that nothing is known about the interference before transmission. Although this strategy can be quickly applied to the simulation model, first a general analysis of how nulls affect the matched filter response will be given.
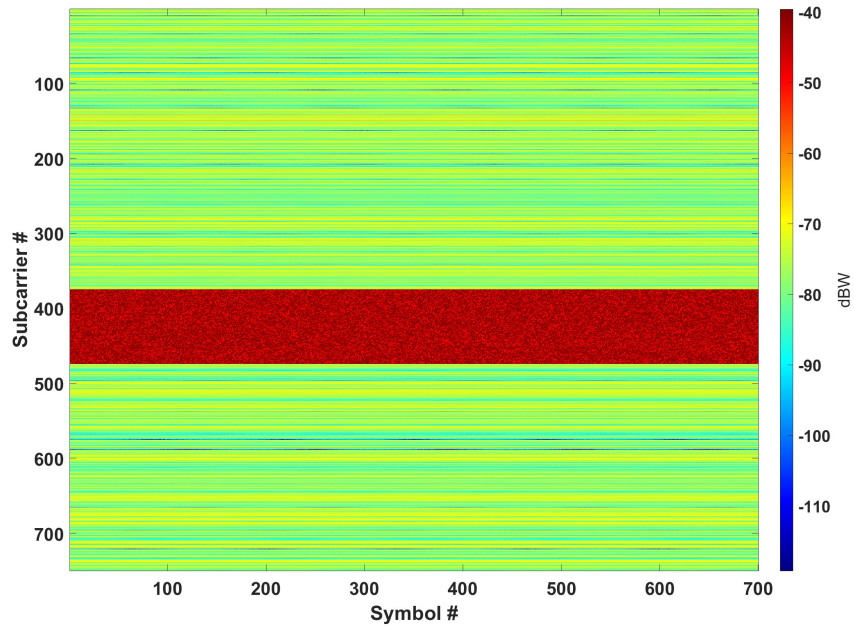
66

Figure 4.1: View of the raw data matrix with an interfering signal, 2-dimensional
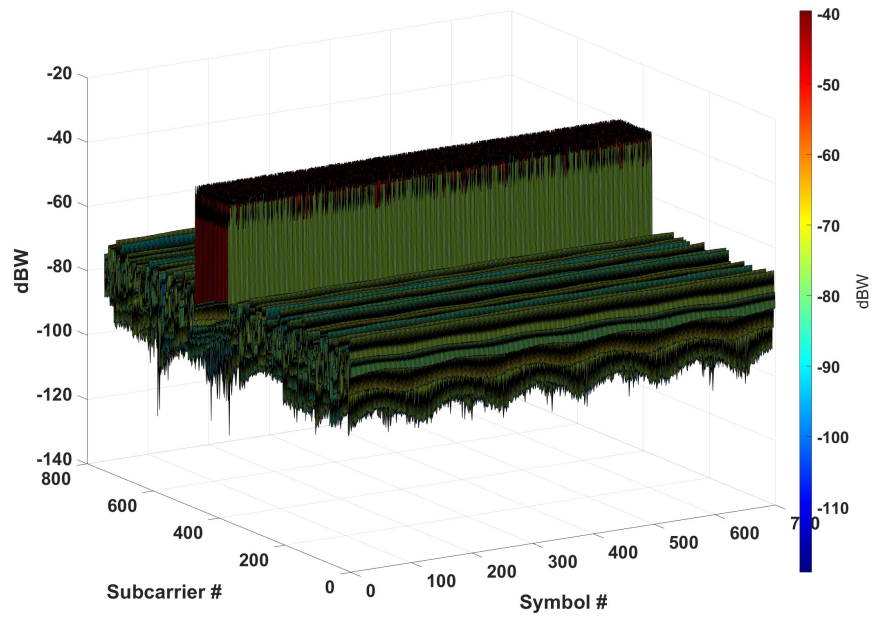

Figure 4.2: View of the raw data matrix with an interfering signal, 3-dimensional
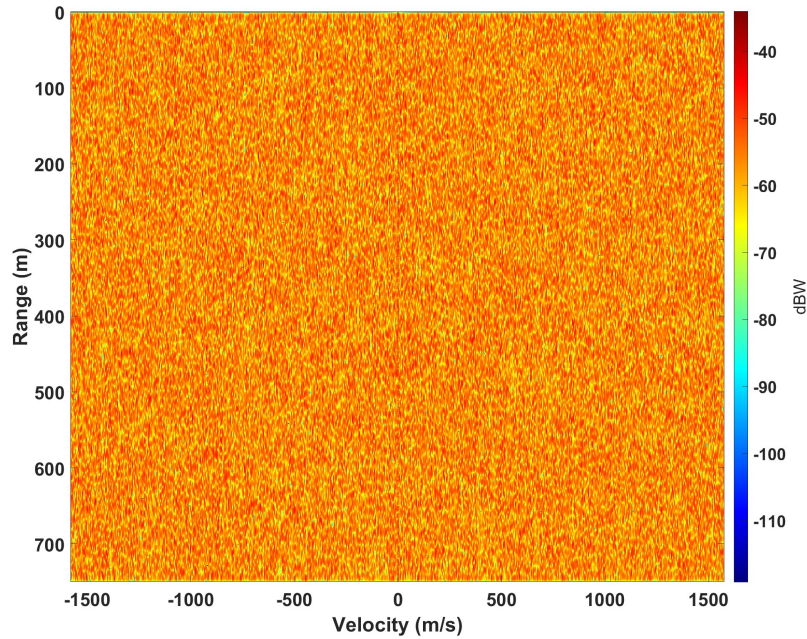
67

Figure 4.3: Range-Doppler map after radar processing the raw data with the interfering signal

4.2 Analyzing the Effect of Nulls

The effect of nulls on the matched filter response will now be analyzed. First, the metrics used for analysis are presented, followed by the sets of null locations. Finally, the results are presented and then discussed.

4.2.1 Metrics

There are three metrics used for the following analysis, the peak sidelobe level (PSL), integrated sidelobe level (ISL), and the mainlobe width ratio. The PSL and ISL are typical metrics used for waveform sidelobe analysis, while the mainlobe width ratio is intended to, of course, provide information about the mainlobe of the response. It has been shown throughout this work that the matched filter response for the OFDM

signal has a sinc shape. As such, consider a sinc-shaped response $r(n)$ that corresponds to a highly oversampled range response. Figure 4.4 gives the plot of $r(n)$ on a decibel scale. The mainlobe (green) is the central part of the response, and the sidelobes (blue) are the parts of the response outside of the mainlobe. From these two regions there are two obvious maxima: the peak of the entire response and the peak sidelobe. The PSL is given as the ratio of these maxima. To develop a more concrete mathematical description of the PSL, let us assume that our response has $N = 2048$ samples and that the first nulls to the left and right of the mainlobe occur at indices n_- and n_+ respectively. Utilizing the fact that the response is symmetrical, the PSL is given by

$$PSL = \max \left\{ \frac{|r(n)|^2}{|r(0)|^2} \right\}, n \in [n_+, 1024].$$
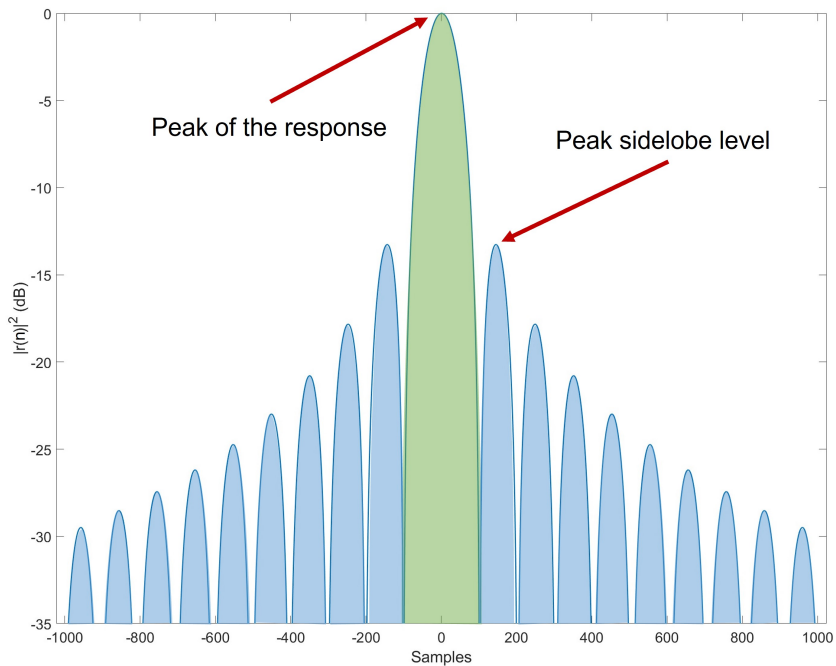(4.1)

Figure 4.4: Sinc-shaped range response, mainlobe (green), sidelobes (blue)

The ISL also compares the sidelobes with the mainlobe; however, instead of being a ratio of the peaks, it is a ratio of the total energy in each region. For the 2048 sample signal used previously, the ISL is given by

$$ISL = \frac{\sum_{n=-1023}^{n_-} |r(n)|^2 + \sum_{n=n_+}^{1024} |r(n)|^2}{\sum_{n_-+1}^{n_+-1} |r(n)|^2} \qquad (4.2)$$

where the numerator is the energy contained in the sidelobes, and the denominator is the energy contained in the mainlobe. The PSL and ISL together give some idea as to how energy is distributed throughout the response. If energy is distributed more evenly across the response (as opposed to being concentrated in the mainlobe), then windowing the response could throw away more energy than is acceptable.

The last metric is the mainlobe width ratio, which is defined for this work as the ratio of the mainlobe width of the nulled signal to the mainlobe width of the null-free signal. This metric is intended to tell if the addition of nulls has made the mainlobe wider or narrower when compared to the null-free case. This also gives some insight into how windowing may affect the final result. For example, if the mainlobe width is significantly wider with nulls, a wider window may need to be used in order to retain energy.

4.2.2   Null Locations

Before displaying test results, the null locations need to be defined. There are four primary tests, each with a different way of placing nulls in the signal. The first test places all of the nulls together in a single group and sweeps them left to right along the signal. This test is described as "grouped" nulls and is shown in Figure 4.5. The second test is similar to the grouped nulls; however, the nulls are split evenly into two groups and are swept symmetrically to the center of the signal as shown in Figure 4.6. The

final two tests involve a random placement of the nulls. One method places *each* null randomly, while the other places groups of 10 randomly. The null and group positions are obtained by generating a random uniform permutation of the possible locations, which is accomplished using *randperm()* in MATLAB. Four different trials for each random placement technique are shown in Figures 4.7 and 4.8. Lastly, it is important to note that for each test the percentage of the signal to be nulled is specified. In each of these examples, 10% of the signal has been nulled (the signal has 1000 samples, so there are 100 nulls). Of course, there are many combinations of null locations that can be explored, but the hope is that these general cases will provide enough insight.
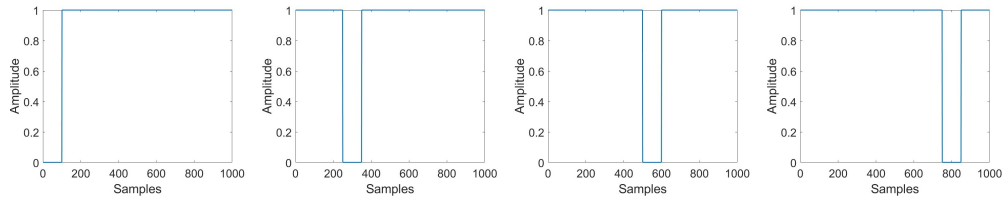

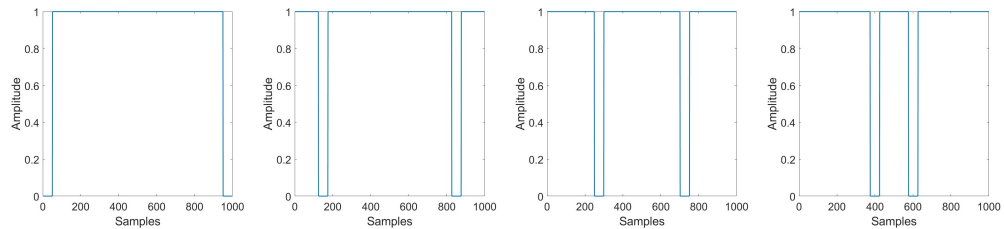Figure 4.5: Grouped nulls for 4 different sweep locations

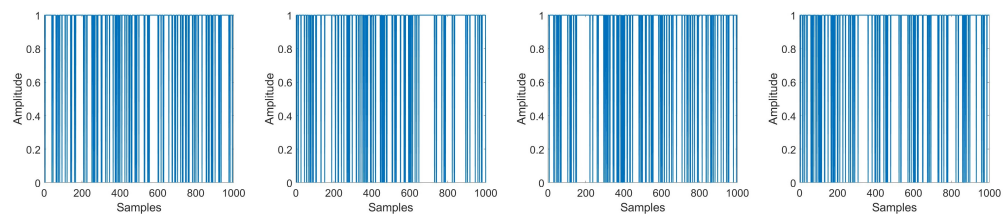Figure 4.6: Symmetric nulls for 4 different sweep locations

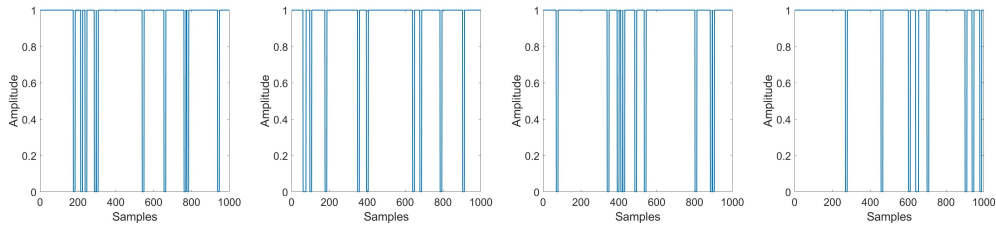Figure 4.7: Four different trials for the random placement of each null

71

Figure 4.8: Four different trials for the random placement of 10 null groups

4.2.3 Results

Figures 4.9, 4.10, 4.11, 4.12, 4.13, and 4.14 provide results for a rectangular function that has been nulled 1%, 2%, 5%, 10%, 20%, and 50% of its total length respectively. The figures provide the results of each of the three metrics for each of the four nulling techniques. Clearly there are many plots. As a result, instead of discussing each one individually, general trends and interesting features will be the main focus.

The most obvious trend is that as the number of nulls increases, the signal increasingly deviates from its original state (which is the null-free case). In other words, all of the metrics experience a wider range of values that they can take. The PSL and ISL primarily trend upwards as the nulls increase, while the mainlobe width ratio generally increases in both directions (above and below 1). A more interesting result is that the symmetric nulls resemble the left half of the grouped nulls result for lower null percentages. As the null percentage increases however, this resemblance begins to fade. When looking at the two random cases, it is clear that the trials using groups of 10 nulls experience a wider variance. That is, when the nulls are in groups they appear to tend towards degrading the response worse than ungrouped nulls.

At higher nulling percentages, there is strange behavior that deserves to be mentioned in some of the results. The behavior is best seen by looking at the grouped mainlobe width ratio results of Figures 4.13 and 4.14. In these plots we see some large

72

discontinuities, so what is causing this? These discontinuities have to do with how the mainlobe is being defined. For all of the plots shown, the mainlobe is defined as the region that is contained by the first minima found by starting in the center and moving in either direction. As the response is distorted, these minima can shift and even disappear entirely, while new ones can be created in unexpected places. The reason that the mainlobe width ratios suddenly drop in these plots is that two new minima have appeared inside of the previous mainlobe. This also explains why the PSL and ISL also jump upwards with a similar discontinuity.

So why not just redefine what qualifies as a zero? That is, we could set an additional criterion for the mainlobe; there could be a minima requirement, as well as a threshold requirement (minima must be below threshold to qualify as "zero"). The problem with this approach is that if you specify a threshold for what zero is, then you will get different results for different thresholds. This naturally leads to the question as to which result is correct; what would "correct" even mean? Because of this issue, it is best to just keep the minima requirement as the sole requirement. Ultimately, it comes down to the fact that if you throw away a significant amount of your signal, the resulting response could be severely distorted and it may be hard to make any sense of it.

To recap, we have found that there is indeed a correlation between the amount of nulls and signal distortion. It appears that the symmetrically placed nulls have similar behavior to the grouped nulls for low nulling percentages. From the random trials, it appears as if nulls that are found in groups have a higher change of degrading the response worse than individually placed nulls. It was also found that if about 20% or more of the response has been nulled, the signal can experience sharp and unexpected distortions in the mainlobe region. For smaller percentages however, the degradation is not super significant. To get a better idea how it these results may affect RCS extraction, we will now perform nulling tests with the main simulation.
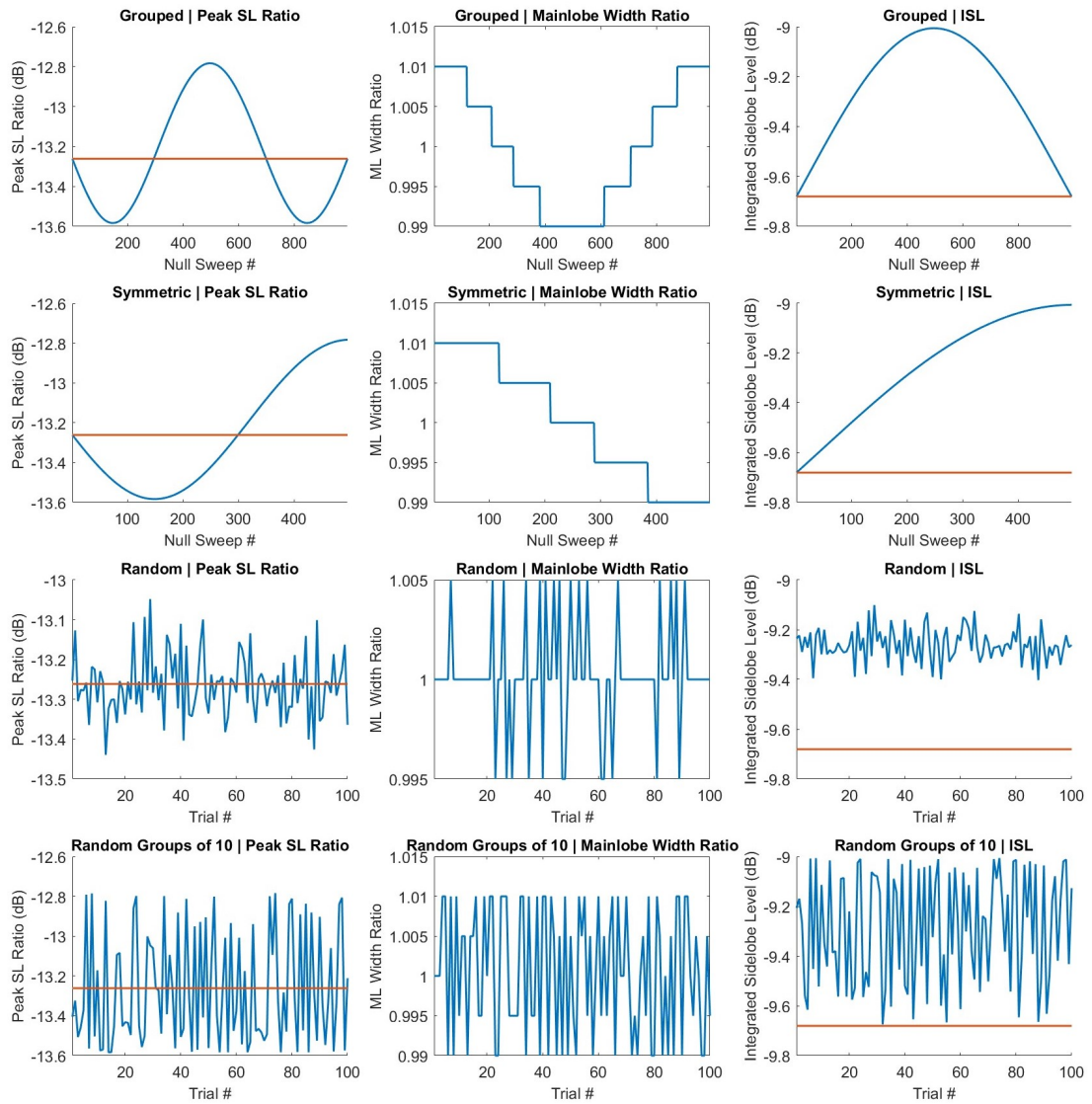
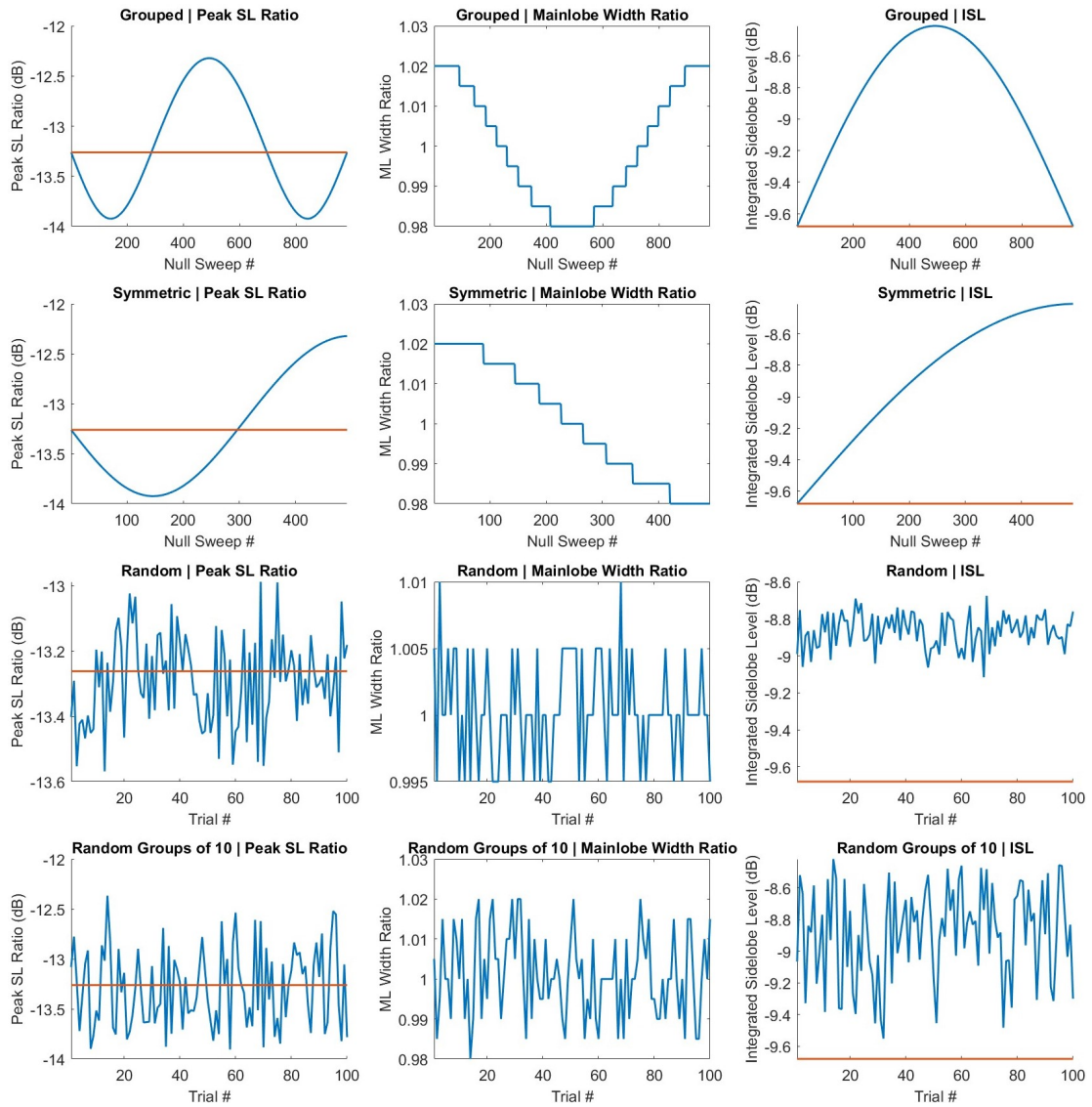Figure 4.9: Results for 1% nulled signal, nulled signal (blue) and null-free signal (red)

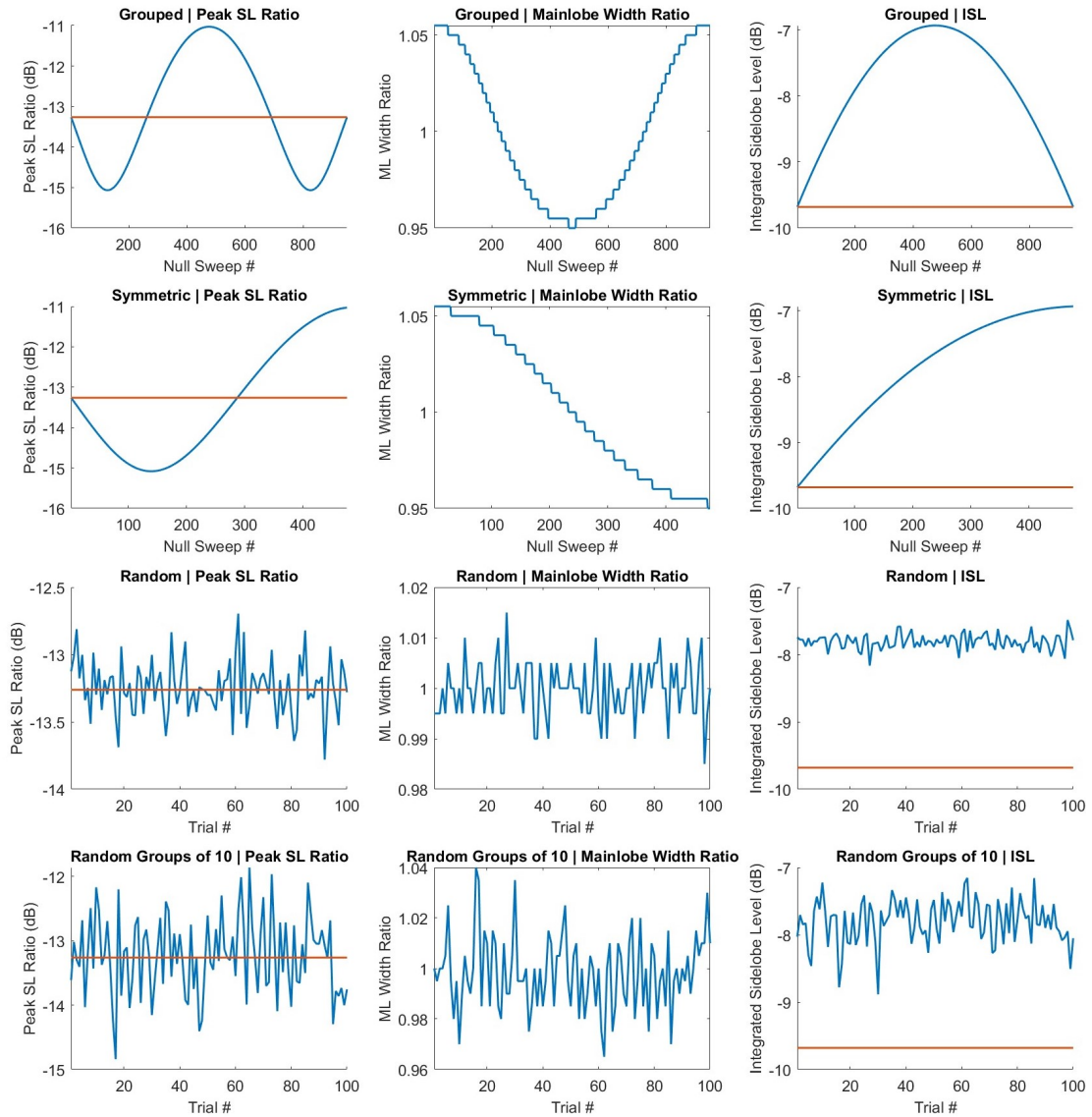Figure 4.10: Results for 2% nulled signal, nulled signal (blue) and null-free signal (red)

Figure 4.11: Results for 5% nulled signal, nulled signal (blue) and null-free signal (red)
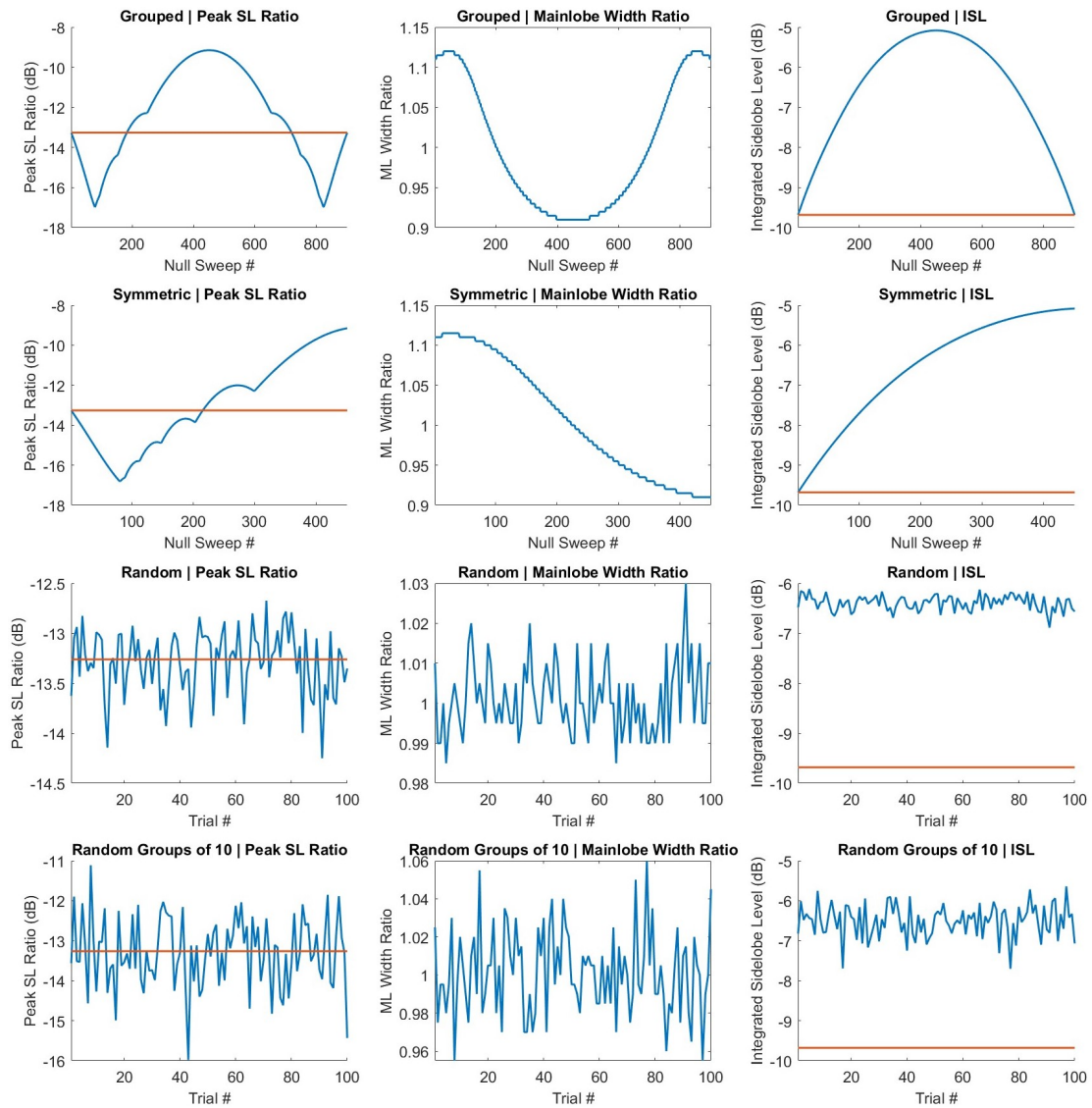
Figure 4.12: Results for 10% nulled signal, nulled signal (blue) and null-free signal (red)
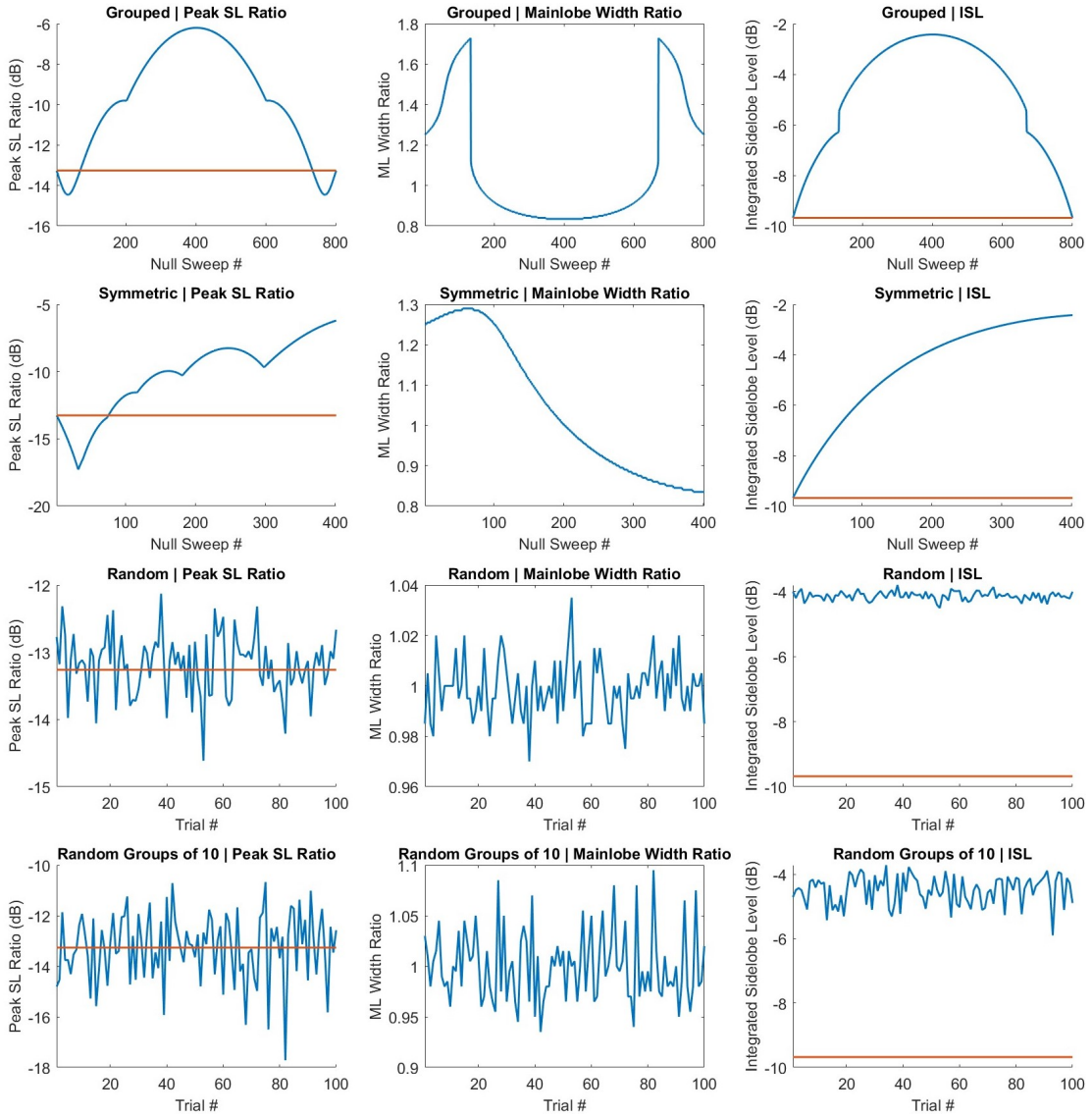
Figure 4.13: Results for 20% nulled signal, nulled signal (blue) and null-free signal (red)
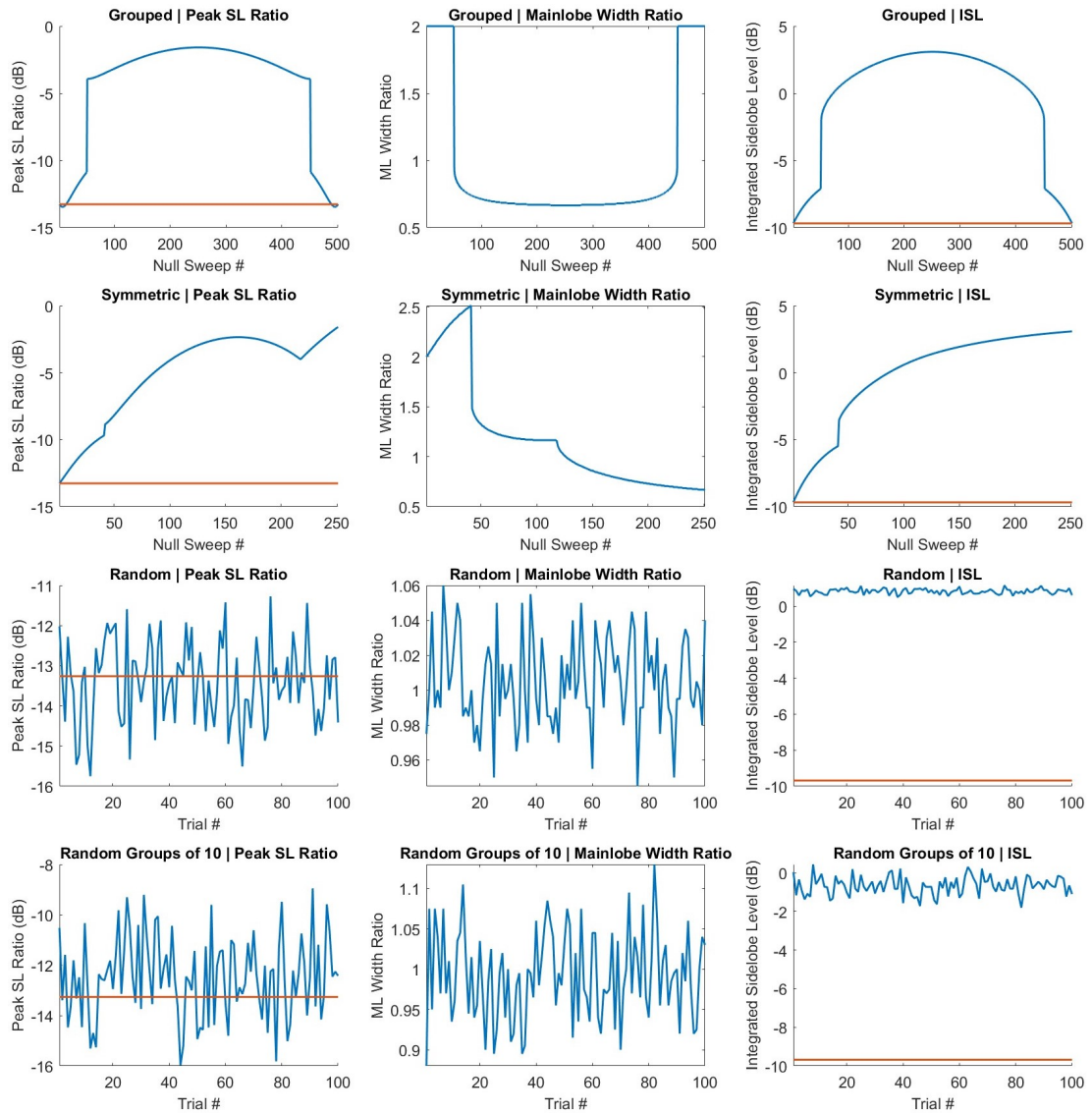
Figure 4.14: Results for 50% nulled signal, nulled signal (blue) and null-free signal (red)

4.3 Simulation Tests

This section will now present the simulation results with the inclusion of nulls. Note that scenario 4 parameters will be used for each simulation. The first example revisits the interference scenario presented in Section 4.1, i.e., the frequencies between 5 and 5.02 GHz have been corrupted. Figure 4.15 shows that the subcarriers occupying these frequencies have been nulled out. OFDM radar processing is then performed on the data as usual, with an IFFT taken across subcarriers and a DFT across symbols. The resulting range-Doppler map and range/Doppler profiles are provided in Figures 4.16 and 4.17 respectively. From both figures it is clear that the range profile is messier than usual as a result of the nulled subcarriers. By contrast, the Doppler profile has remained intact, which is not particularly surprising considering that the null locations are the same across symbols. Despite the nulls, the target is still clearly distinguishable from the clutter region.
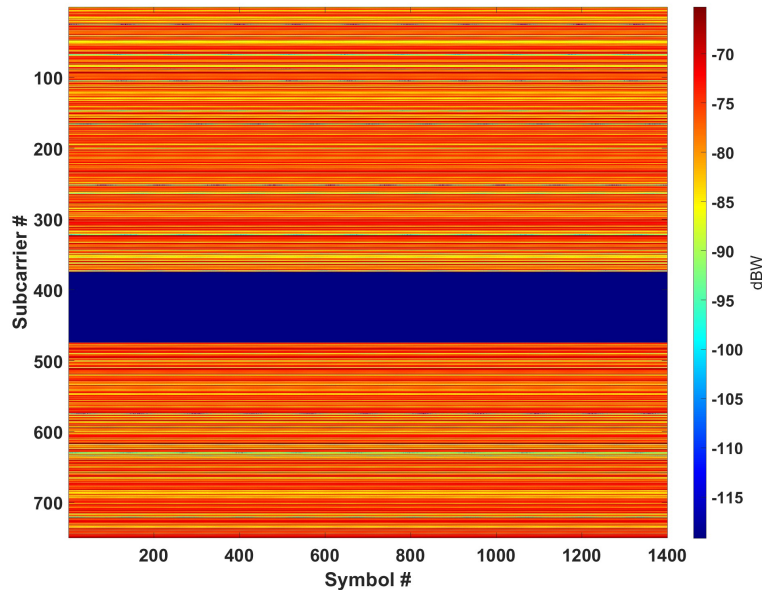

Figure 4.15: Subcarriers occupying frequencies between 5 and 5.02 GHz are nulled out
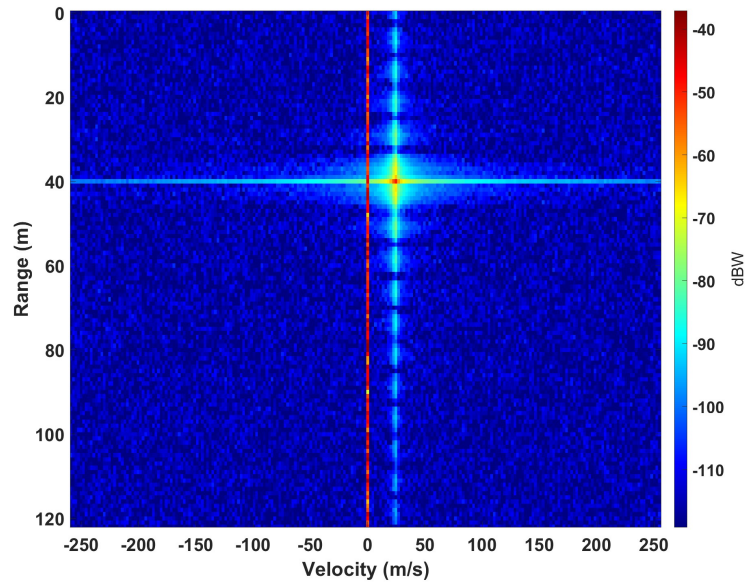
Figure 4.16: Range-Doppler map result with subcarriers between 5 and 5.02 GHz nulled out
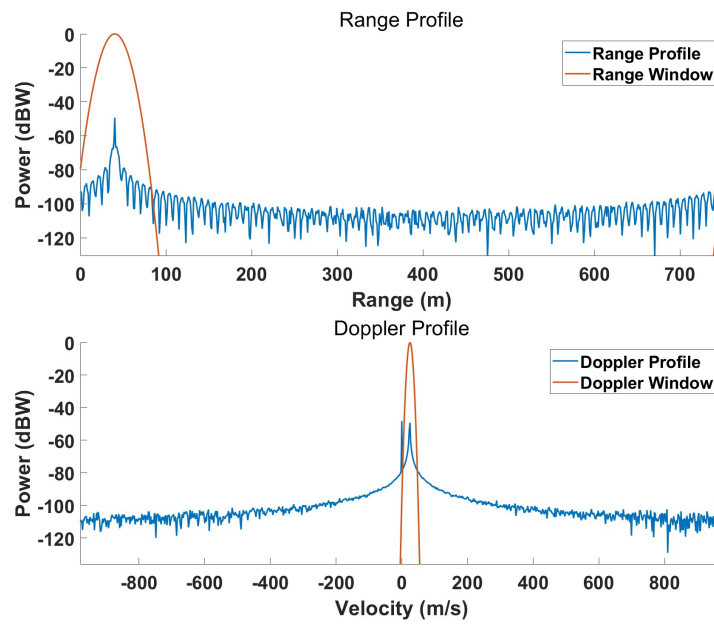

Figure 4.17: Range/Doppler profiles with subcarriers between 5 and 5.02 GHz nulled out

The question then becomes how the RCS extraction has been affected by nulling out subcarriers. The RCS extraction result is shown in Figure 4.18. As expected, we have completely lost the information in the region that has been nulled. Notice that we have also lost information to the left and right of the nulled region, which is a result of the tapering effect from windowing. Luckily, nulling the signal uniformly across symbols only affects the range/subcarrier dimension. Since our window in this dimension is quite wide, the tapering is not too significant. We can reduce this taper by widening the range window, as will be shown shortly.
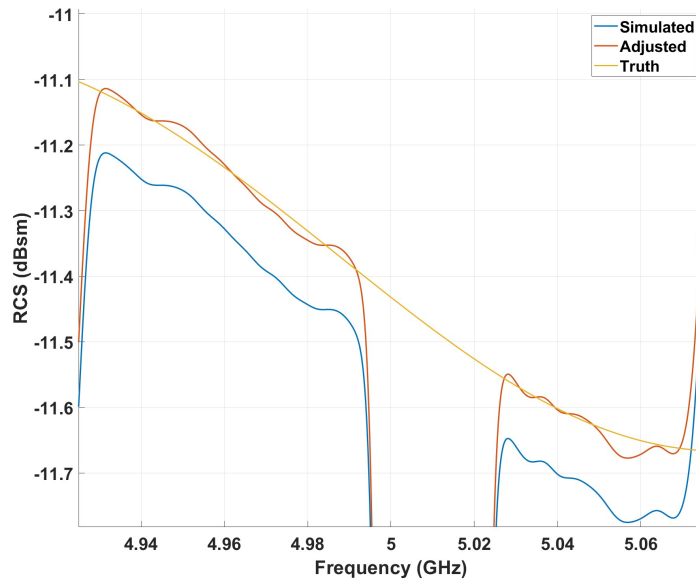

Figure 4.18: RCS extraction result with subcarriers between 5 and 5.02 GHz nulled out

We will now consider a new case where there is additional narrowband interference below 5 GHz. This interference has a bandwidth of 10 MHz and is centered about 4.985 GHz. In other words, the interference occupies frequencies between 4.98 and 4.99 GHz. Figure 4.19 shows the subcarriers that have been nulled out as a result of the additional interference. From our previous analysis in Section 4.2, we know that the response becomes increasingly distorted with more nulls. The RDM and range/Doppler profiles

shown in Figures 4.20 and 4.21 confirm that the range response looks slightly degraded with the additional nulls. Despite the degraded range response, the target is still clearly identified in the RDM, so windowing and RCS extraction are easily performed.

Figure 4.22 shows the RCS extraction result. From this it is clear that we have lost the entire region between 4.98 and 5.02 GHz, despite having subcarrier information between 4.99 and 5 GHz. This is a result of the range windowing, which has tapered away the small region between interference zones. To remedy this, we can widen the range window; however, this results in a higher measurement variance. Figures 4.23 and 4.24 show that for a widened range window, the previously lost region can be recovered at the cost of a noiser measurement. To recap, the addition of nulls degrades the range response, but does not affect the Doppler response. Also, the degradation should not affect RCS extraction apart from losing the nulled regions, assuming that the target can be identified in the RDM. However, range window width may need to be a consideration for closely-spaced null regions.
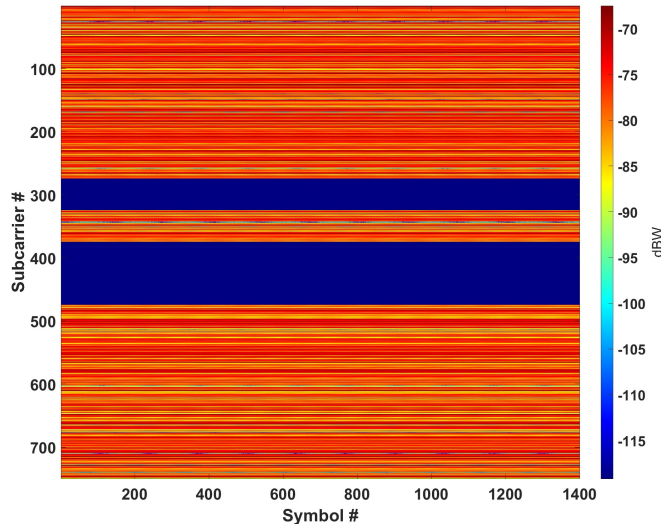

Figure 4.19: Subcarriers occupying frequencies 4.98 to 4.99 GHz and 5 to 5.02 GHz are nulled out

Figure 4.20: Range-Doppler map result with subcarriers inside 4.98 to 4.99 GHz and 5 to 5.02 GHz nulled out

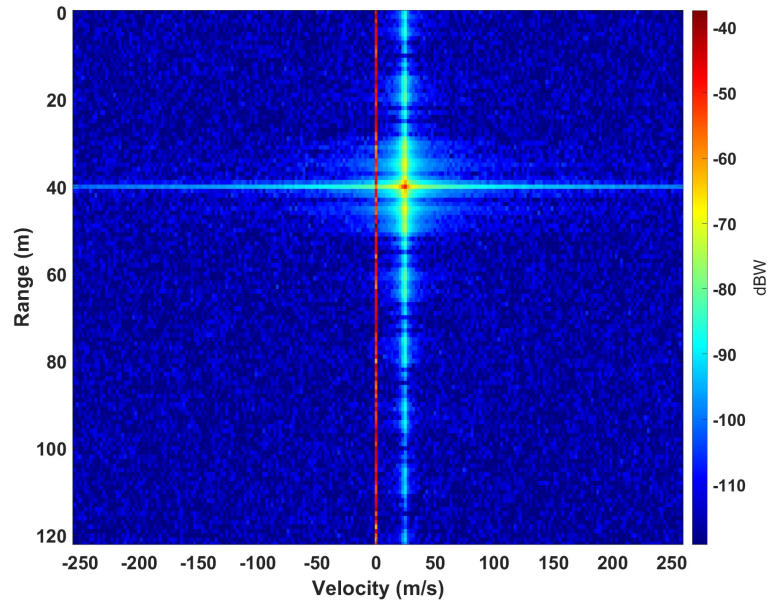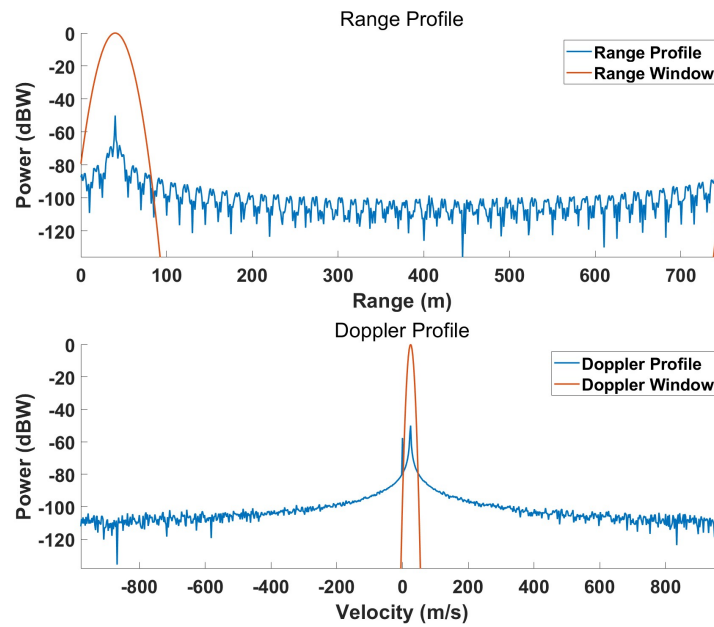Figure 4.21: Range/Doppler profiles with subcarriers inside 4.98 to 4.99 GHz and 5 to 5.02 GHz nulled out
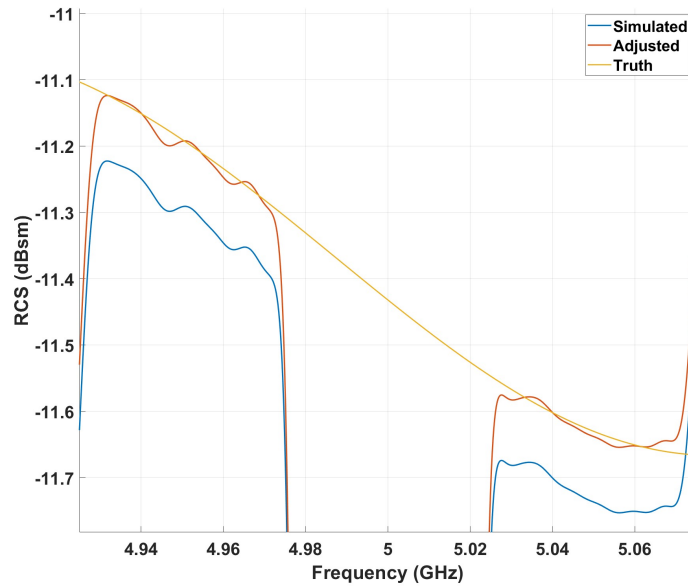
Figure 4.22: RCS extraction result with subcarriers inside 4.98 to 4.99 GHz and 5 to 5.02 GHz nulled out
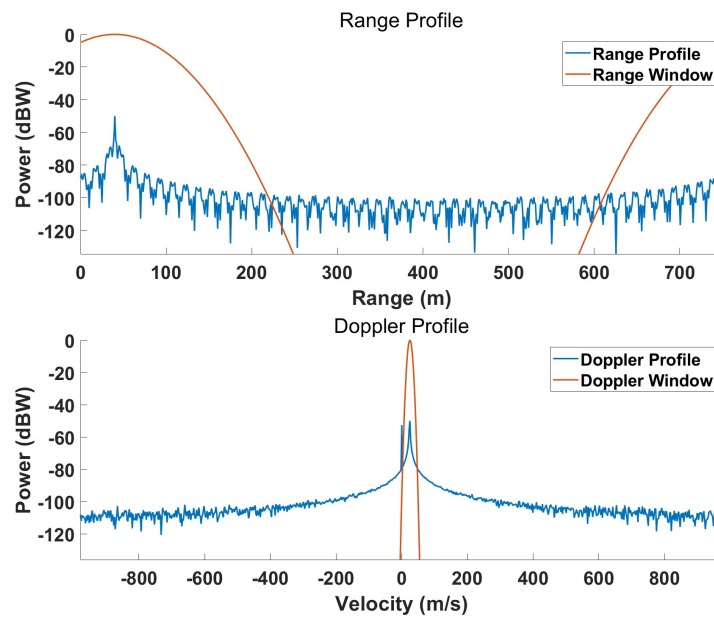

Figure 4.23: Range/Doppler profiles with subcarriers inside 4.98 to 4.99 GHz and 5 to 5.02 GHz nulled out, increased range window width
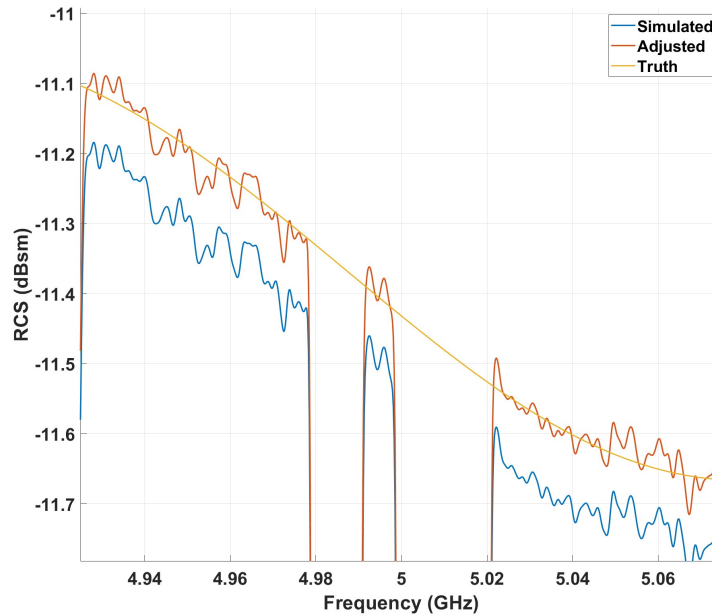
Figure 4.24: RCS extraction result with subcarriers inside 4.98 to 4.99 GHz and 5 to 5.02 GHz nulled out, increased range window width

If the range window must be widened to reduce taper, considerable noise may appear in the final measurement, depending on the SNR. An unweighted moving average (MA) filter (see next section for general MA filter discussion) may help reduce measurement variance as a result of inadequate windowing, poor SNR, or a combination of the two. To illustrate this, we will alter the target range of the scenario that has been presented in this section. The target range is changed from 40 m to 250 m, which results in a reduced SNR. From the range-Doppler map shown in Figure 4.25, it can be seen that the target response is mostly embedded in the noise floor except for the central peak. Figure 4.26 shows the RCS extraction result and the result after applying a 30-point MA filter. The MA filter helps smooth out the RCS result; however, we see that we have introduced significant tapering once again. As the MA filter length is increased, the smoothing gets better, but the tapers get worse. This is a similar tradeoff to what we observed with the range window width.
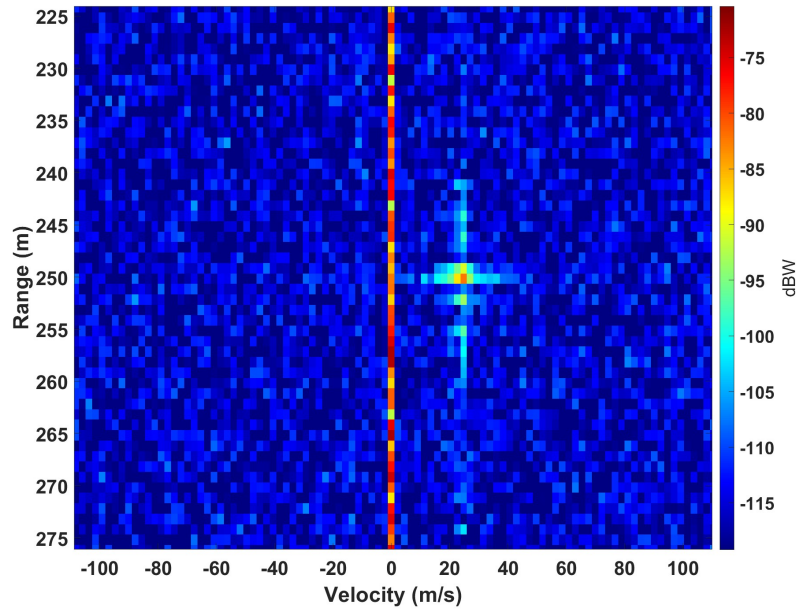
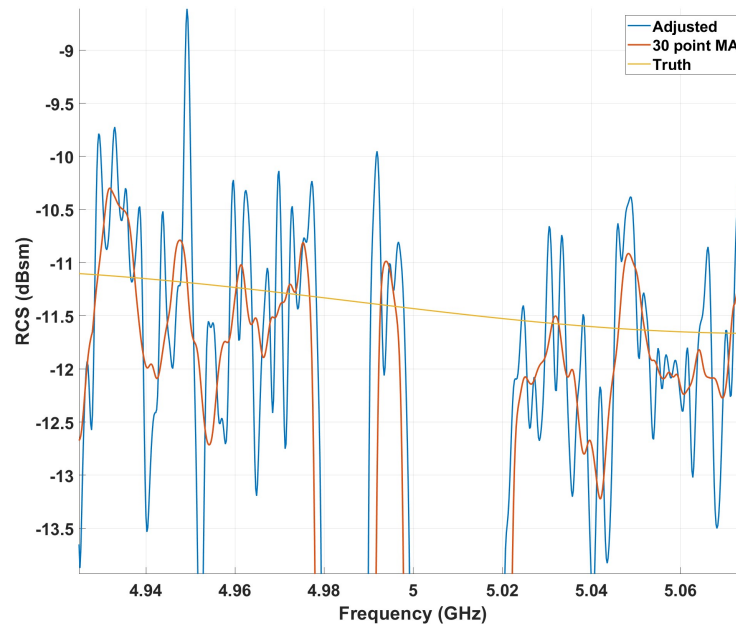Figure 4.25: Range-Doppler map after moving the target to 250 m

Figure 4.26: RCS extraction result with and without a 30-point moving average filter

4.4 Spectral Estimation & Reconstruction

Up to this point, we have seen how nulling subcarriers throws away RCS data at those frequency points. However, with spectral estimation techniques it may be possible to reconstruct the power spectrum and obtain RCS measurements across the full symbol bandwidth. Since there is a great deal of literature on spectral estimation, only basic principles will be presented in this section. For more details, see [17].

4.4.1 Fundamental Theory

The goal of spectral estimation is ultimately to determine the spectral content of a random process from a finite number of samples of that process. Formally, the spectral content of a random process is called the power spectral density (PSD), and it describes the distribution of power across different frequencies. For a wide sense stationary (WSS) random process, the PSD and autocorrelation function (ACF) $R(\tau)$ form a Fourier transform pair. This implies that a complete PSD requires an infinite number of points in the ACF, which is clearly impractical since we can only obtain a finite number of time domain samples. Since determining the exact PSD is an impossible task, the best we can do is estimate it.

An example of a common spectral estimator is the periodogram. Given a finitely sampled signal $x[n]$ with Fourier transform $X(f)$, the periodogram is given by $|X(f)|^2$ and is usually normalized by the signal length N. Spectral estimators such as the periodogram operate under the assumption that data outside of the observation window is zero; however, this is typically not a realistic assumption. Rather than assume that the data is zero outside of the observation window, we may make some assumptions about the random process or make use of a priori information. In other words, we can develop a model that tries to approximate the random process, and the model parameters can

be derived from the observation data. If the model is accurately chosen, this modeling approach can usually obtain a better result.

The models of interest fall under a class known as rational transfer function models. They are the autoregressive (AR) model, moving average (MA) model, and the autoregressive-moving average (ARMA) model. Consider a WSS random process $x[n]$ that is the output of a BIBO stable LTI system with input $w[n]$, where $w[n]$ is a white process following a Gaussian distribution with zero mean and variance σ^2. Suppose that the present input can be written as a linear combination of the present output and past outputs as

$$w[n] = x[n] + a_1 x[n-1] + a_2 x[n-2] + \cdots + a_p x[n-p] \tag{4.3}$$

or equivalently,

$$x[n] = -\sum_{k=1}^{p} a_k x[n-k] + w[n] \tag{4.4}$$

This form represents an AR model of order p and is sometimes referred to as an *all-pole* model. This is because the transfer function contains only poles. The transfer function is given by

$$\frac{X(z)}{W(z)} = \frac{1}{A(z)} = \frac{1}{\sum_{k=0}^{p} a_k z^{-k}}, a_0 = 1 \tag{4.5}$$

where $X(z)$ and $W(z)$ are the z-transforms of the output and input respectively.

Now consider that the present output is modeled as linear combinations of the current and past inputs as

$$x[n] = b_0 w[n] + b_1 w[n-1] + b_2 w[n-2] + \cdots + b_q w[n-q] \tag{4.6}$$

or equivalently,

$$x[n] = \sum_{k=0}^{q} b_k w[n-k] \tag{4.7}$$

This form is a MA model of order q and is sometimes referred to as an *all-zero* model, since the transfer function contains only zeros. The transfer function is given by

$$\frac{X(z)}{W(z)} = B(z) = \sum_{k=0}^{q} b_k z^{-k} \tag{4.8}$$

Finally, (4.4) and (4.7) may be combined to form the ARMA model, which has a linear difference equation of the form

$$x[n] = -\sum_{k=1}^{p} a_k x[n-k] + \sum_{k=0}^{q} b_k w[n-k] \tag{4.9}$$

The transfer function then follows easily

$$H(z) = \frac{B(z)}{A(z)} = \frac{\sum_{k=0}^{q} b_k z^{-k}}{\sum_{k=0}^{p} a_k z^{-k}} \tag{4.10}$$

With the transfer functions of (4.5), (4.8), and (4.10) in mind, recall that the ACF and PSD are a Fourier transform pair for a WSS process. Also recall that for a WSS process, the output ACF is related to the input ACF by the system transfer function as

$$R_{yy}(\tau) = R_{xx}(\tau) * h^*(-\tau) * h(\tau) \tag{4.11}$$

So, the z-transform of the output ACF is given for the ARMA model as

$$P_{xx}(z) = H(z)H^*(1/z^*)P_{ww}(z) = \frac{B(z)B^*(1/z^*)}{A(z)A^*(1/z^*)}P_{ww}(z) \tag{4.12}$$

which when evaluated along the unit circle ($z = \exp(j2\pi f)$) yields the output PSD

$P_{xx}(f)$ for the ARMA model [17]

$$P_{\text{ARMA}}(f) = P_{xx}(f) = \sigma^2 \left| \frac{B(f)}{A(f)} \right|^2 \tag{4.13}$$

Through the same technique we can obtain the PSD for the AR and MA models [17]

$$P_{\text{AR}}(f) = \frac{\sigma^2}{|A(f)|^2} \tag{4.14}$$

$$P_{\text{MA}}(f) = \sigma^2 |B(f)|^2 \tag{4.15}$$

So, how does spectral estimation theory apply to our problem? Spectral estimation tries to determine the PSD for a finitely sampled random process. In our case, this isn't exactly what we want; we want to *reconstruct* missing pieces of our spectrum. If we were to estimate the spectrum from the time domain data, then we would be creating a model that still contains gaps in the spectrum. Because of this, we will not be solving a spectral estimation problem, but instead will use principles to reconstruct our RCS. In particular, we will use a rational transfer function model to try to model the spectrum itself. With this model, we can predict values for gaps in the spectrum.

4.4.2 AR Model Tests

Now that the general form of each model has been presented, some tests will be presented that try to fill the gaps in our RCS using an AR model. The AR model is chosen for testing because it is generally easier to solve for the model parameters. This is because given the ACF it is possible to determine the AR parameters by solving a set of linear equations; however, for MA and ARMA models this relationship is nonlinear [17]. Luckily for this scenario, a MATLAB function already exists that achieves what we are trying to do. The MATLAB function *fillgaps()* fills signal gaps based on an AR

model. This function chooses the AR model order p such that the Akaike information criterion (AIC) [18] is minimized. The AIC seeks to address the trade-off space that exists when trying to determine the model order. That is, the AIC tries to weight the risk of underfitting (model order is too low) and overfitting (model order is too high) . After determining the model order, the Burg method is used to estimate the AR parameters; more information about the Burg method can be found in [17].

Figure 4.27 shows the result after using an AR model to estimate the RCS from the nulled spectrum RCS result of Figure 4.24. The AR model is used to fill in the gaps, and then the result is smoothed. Clearly, the model has produced an accurate estimation of the missing RCS measurements. Let us consider another scenario where the bandwidth has been greatly increased to 1 GHz in order to observe a wider variation in RCS. Additionally, the target range has been set to 10 m in order to retain a high SNR. Subcarriers from 4.9 to 5.1 GHz have been nulled out, and the results after applying the AR model and smoothing are shown in Figure 4.28. In this scenario, it is clear that the model order was not chosen properly by *fillgaps()*. This was not evident from the previous test shown in Figure 4.27 because the RCS across the nulled regions was approximately linear. In general, since our data is noisy, we require a high model order to appropriately model the data. A manual increase of the model order results in a much better result and is shown in Figure 4.29. Note that the model order p was chosen somewhat arbitrarily as the number of RCS samples divided by two ($p = 2500$ in this case).

It is important to remember that these tests have been run with high SNRs (around 70 dB). For low SNRs, it is expected that some level of range windowing is required to avoid being noise-limited (meaning that the noise is too strong to make an accurate RCS measurement). In order to analyze how range windowing affects the AR modeling approach, let us consider many different simulation runs.
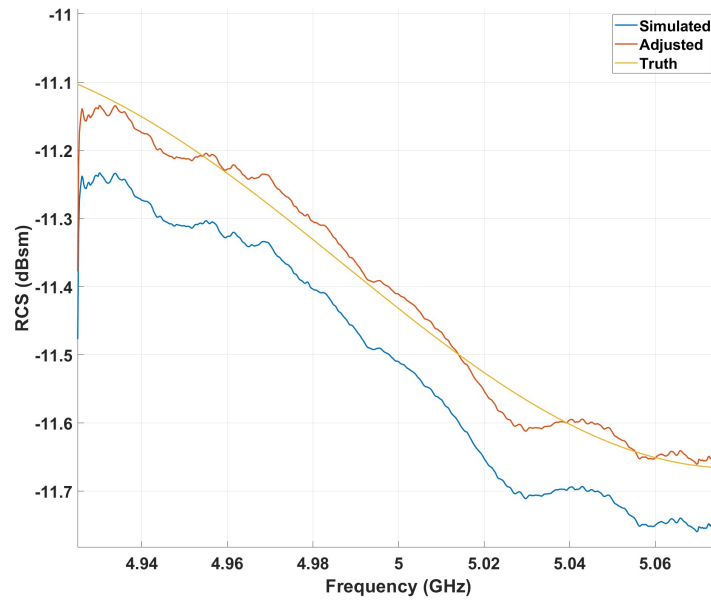
Figure 4.27: RCS extraction result from Figure 4.24 after applying AR model and smoothing
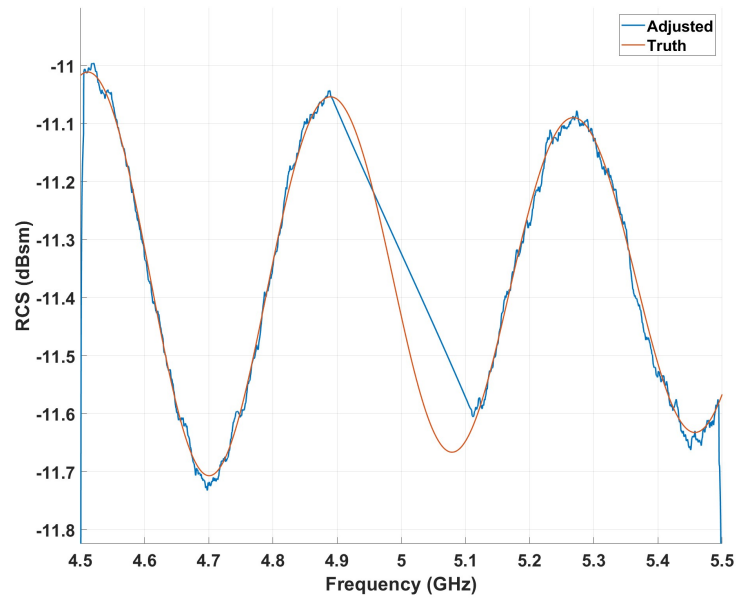

Figure 4.28: RCS extraction result with AR model after increasing bandwidth to 1 GHz and nulling out 4.9 to 5.1 GHz
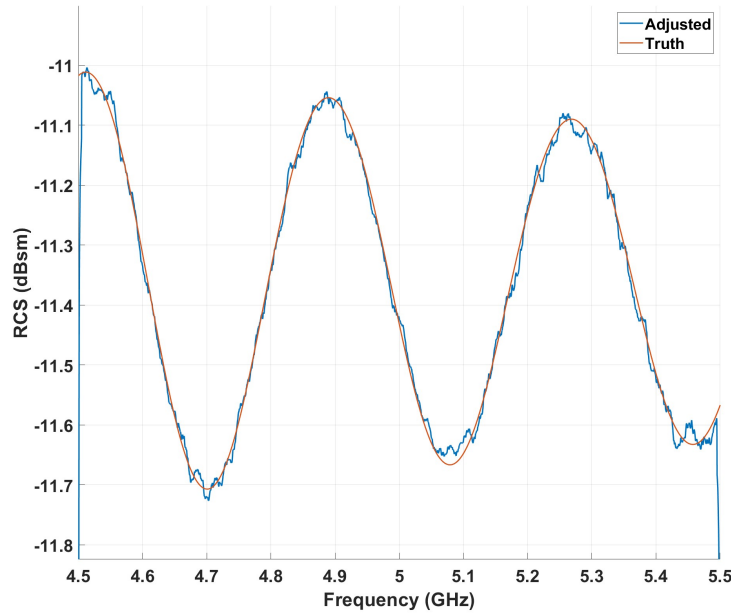
Figure 4.29: RCS extraction result with AR model from Figure 4.28 with increased model order

Figures 4.30, 4.31, and 4.32 each contain results from 110 simulation runs. Each cell represents the percent error of the AR model reconstruction compared with the true RCS. For each simulation, the post-processing SNR and "percent nulled" is specified. The percent nulled determines what percentage of the signal to null, with the nulls consisting of a single group centered at the waveform center frequency. Each simulation run has 1.5 GHz of bandwidth, which allows for several of the RCS oscillations to be captured. Additionally, after the AR models have been applied, an unweighted moving average filter is used to smooth the result. To keep the results consistent, the model order is the number of RCS samples divided by two, which is $p = 3750$ for all results shown.

Figure 4.30 shows results that do not utilize a range window. We can see that for high SNRs, there is excellent reconstruction performance overall. However, at low SNRs our overall performance quickly becomes noise limited, which can be seen by

the sharp increase in the percent error. To remedy this noise limitation, we will apply a range window with width factor $\alpha_r = 10$. The results, which are given in Figure 4.31, show that with range windowing we are able to improve our performance at lower SNRs while retaining a low percent error for high SNRs. However, some of the simulation runs still report a somewhat high percent error, so we will make our window slightly narrower by raising α_r to 15. The results for $\alpha_r = 15$, which are shown in Figure 4.32, show that we have slightly improved our low SNR results; however, we can also see that we have degraded our high SNR performance. This is because as the range window is made narrower, our RCS result is increasingly smoothed. For smooth signals, the sensitivity to overfitting increases, which is why some trials in Figure 4.32 have a high percent error. In other words, if we apply a range window such that our RCS result is smoothed, then we have to lower the model order compared to the case in which we do not range window. The question of how to determine the proper model order from the data is something that still needs to be explored in future work.
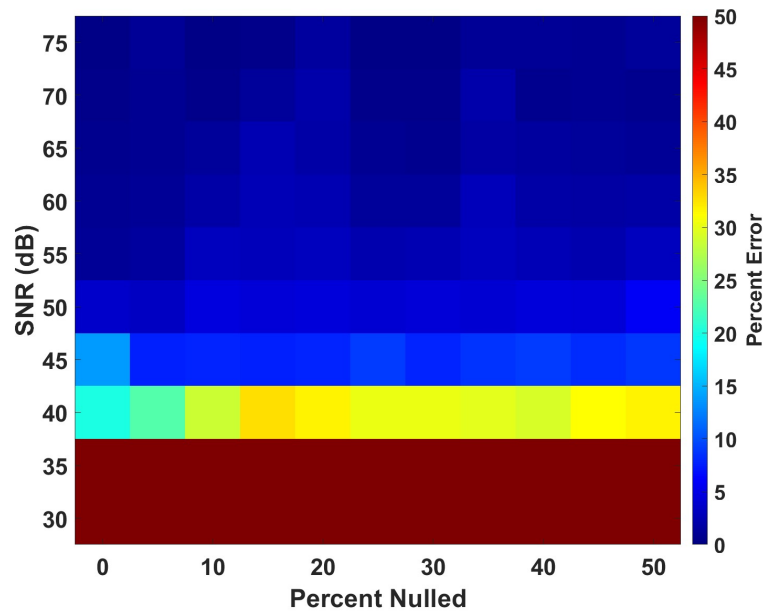

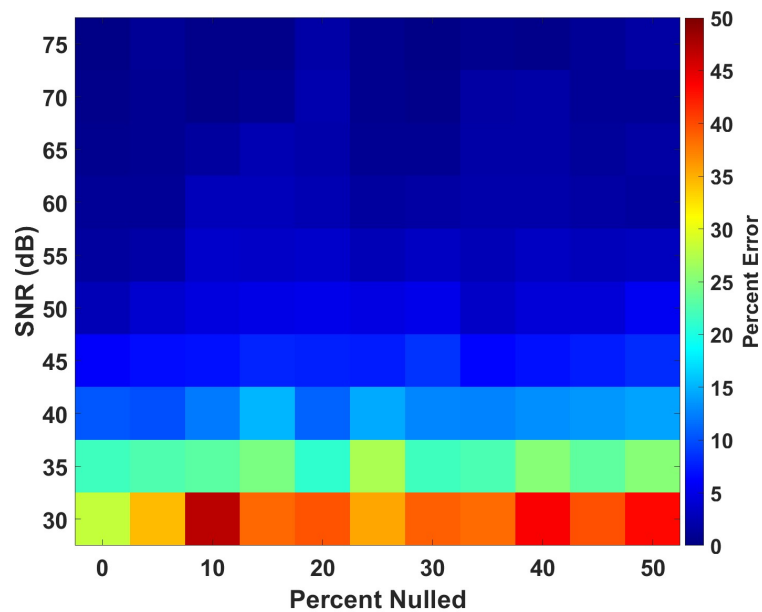Figure 4.30: AR modeling simulation results with no range windowing

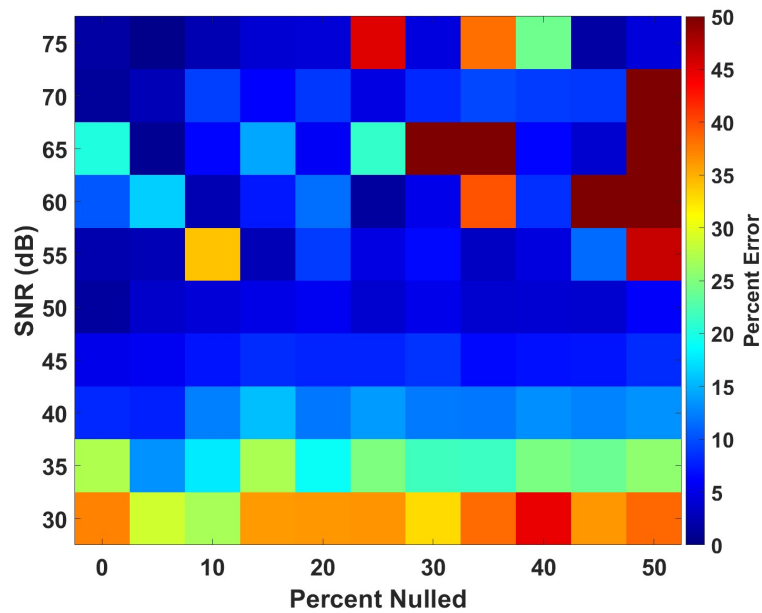Figure 4.31: AR modeling simulation results with $\alpha_r = 10$

Figure 4.32: AR modeling simulation results with $\alpha_r = 15$

Chapter 5

Conclusions & Future Work

5.1 Conclusions

This thesis has shown that from a simulation standpoint, it is indeed possible to extract RCS from a moving target using OFDM. In order to be successful, ground clutter occupying the zero Doppler portion of the range-Doppler map must be filtered out. It has been seen that in order to filter effectively, there must be adequate Doppler spacing between the target and clutter region, as well as fine enough Doppler resolution. For targets that straddle Doppler bins, there may be some reduction in power due to windowing with the Gaussian window; however, it was shown that this effect can be compensated for. The RCS extraction performance was also seen to be a strong function of SNR. To increase the SNR, it proved helpful to increase the number of transmitted symbols. This raised the Doppler processing gain for the target, thus helping SNR; however, it was also seen that the same processing gain was applied to the ground clutter. As a result, increasing the number of symbols helps with SNR, but has little effect on improving SINR. It was also shown that range windowing plays an important part in fighting low SNR, since windowing in range helps filter noise and acts like a smoothing filter.

It was also shown that for an interfering signal from another transmitter, nulling out

the corrupted spectrum proved crucial for identifying the target in the range-Doppler space. Although spectral nulls distort the ideal sinc-shaped time domain response, they have little effect on the RCS extraction process, other than zeroing out RCS values in the final result. Finally, it was observed that parametric modeling techniques may prove helpful for reconstructing parts of the spectrum that were nulled out; however, it is clear that attention should be given to model order selection to ensure accurate results.

5.2 Future Work

With this thesis completing the simulation analysis, the natural next step is to begin real-world tests. In order to perform such tests, there are practical issues that must be researched. One of the more glaring issues concerns how to mount a calibration target on a moving vehicle to separate it from the clutter zone. Assuming that these obstacles are overcome and the tests are successful, there are still more scenarios to be considered. For instance, throughout this work we have restricted our discussion to that of a single target, but there may be multiple targets present at one time. This greatly changes how the filtering problem should be formulated, since now there are competing target returns in both the range and Doppler dimensions. There may even be additional filtering considerations depending on the degrees of freedom that you wish to allow for. For example, if the radar itself is moving, then the clutter zone could be shifted and possibly distorted. Types of clutter other than ground clutter may pose additional challenges.

Additional work can also be done in analyzing spectral reconstruction models. In this thesis, only the AR model was considered; however, a different model may provide better results. Before analyzing different models however, additional work on model order selection should probably be conducted. In addition, other reconstruction

approaches such as interpolation-based methods may prove beneficial for narrowband reconstruction. Interpolation-based methods are likely more efficient computationally, but may also be more accurate than a parametric model in cases where the training data is not representative of the missing data.

References

[1] E. F. Knott, J. F. Shaeffer, and M. T. Tuley, *Radar Cross Section, 2nd ed.* SciTech, 2004.

[2] R. E. Jarvis, J. G. Metcalf, J. E. Ruyle, and J. W. McDaniel, "Measurement and Signal Processing Techniques for Extracting Highly Accurate and Wideband RCS," *IEEE International Instrumentation and Measurement Technology Conference (I2MTC)*, Glasgow, United Kingdom, 2021, pp. 1-6.

[3] ——, "Wideband Measurement Techniques for Extracting Accurate RCS of Single and Distributed Targets," *IEEE International Instrumentation and Measurement*, vol. 71, pp. 1-12, 2022, Art no. 6001512.

[4] C. Sturm and W. Wiesbeck, "Waveform Design and Signal Processing Aspects for Fusion of Wireless Communications and Radar Sensing," *Proceedings of the IEEE*, vol. 99, no. 7, pp. 1236-1259, July 2011.

[5] C. Munnell, R. Mattingly, S. Flandermeyer, and J. G. Metcalf, "On the Practical Use and Experimentation of LTE Signals for Radar-Communications," *2022 IEEE Radar Conference (RadarConf22)*, New York City, NY, USA, 2022, pp. 1-6, 2022.

[6] C. A. Balanis, *Antenna Theory: Analysis and Design.* John Wiley & Sons, 2005.

[7] M. A. Richards, J. A. Scheer, and W. A. Holm, *Principles of Modern Radar Vol. 1: Basic Principles.* SciTech, 2010.

[8] "The Authoritative Dictionary of IEEE Standards Terms, Seventh Edition," *IEEE Std 100-2000*, vol., no., pp.1-1362, Dec. 2000.

[9] B. R. Mahafza, *Radar Systems Analysis and Design Using MATLAB, 1st ed.* Chapman & Hall/CRC, 2000.

[10] A. Ishimaru, *Electromagnetic Wave Propagation, Radiation, and Scattering: From Fundamentals to Applications, 2nd ed.* John Wiley & Sons, 2017.

[11] A. Papoulis and S. U. Pillai, *Probability, Random Variables, and Stochastic Processes.* McGraw-Hill Education, 2002.

[12] J. Armstrong, "OFDM for Optical Communications," *Journal of Lightwave Technology*, vol. 27, no. 3, pp. 189-204, Feb. 1, 2009.

[13] M. A. Richards, *Fundamentals of Radar Signal Processing*. McGraw-Hill Education, 2014.

[14] M. Skolnik, *Radar Handbook, 3rd ed.* Chapter 16, "Ground Echo," McGraw-Hill Publishing Company, 2008.

[15] A. Oppenheim, R. Schafer, and J. Buck, *Discrete-Time Signal Processing*. Prentice Hall, 1999.

[16] M. Engels, *Wireless OFDM Systems: How to Make them Work?* Boston, MA: Kluwer Academic, 2002.

[17] S. M. Kay, *Modern Spectral Estimation: Theory & Application*. Prentice Hall, 1988.

[18] H. Akaike, "Fitting Autoregressive Models for Prediction," *Annals of the Institute of Statistical Mathematics*, vol. 21, 1969, pp. 243-247.